Study of light nuclei and strange baryon production in proton-proton and Pb-Pb collisions with ALICE

Politecnico di Torino

ScuDo
Scuola di Dottorato ~ Doctoral School
WHAT YOU ARE, TAKES YOU FAR

Doctoral Dissertation
Doctoral Program in Physics (35th cycle)

Study of light nuclei and strange baryon production in proton–proton and Pb–Pb collisions with ALICE

Alessandro Balbino

******

Supervisors:
Prof.ssa Stefania Bufalino, Supervisor
Dr. Livio Bianchi, Co-Supervisor

Doctoral Examination Committee:
Prof.ssa Sara Palmerini, Referee, Università degli Studi di Perugia
Dr. Lizardo Valencia Palomo, Referee, Universidad de Sonora

Politecnico di Torino
Tuesday 9th May, 2023

I hereby declare that, the contents and organization of this dissertation constitute my own original work and does not compromise in any way the rights of third parties, including those relating to the security of personal data.

Alessandro Balbino
Tuesday 9th May, 2023

Abstract

A comprehensive description of the mechanisms underlying particle production in the cool-down of physics systems characterized by extreme energy density and temperature is still an open point. An outstanding example of such a highly energetic process is supplied by the high energy hadronic collisions provided by the Large Hadron Collider (LHC) at CERN. An abundant production of light flavor particles, made up of u, d and s quarks, is observed in the proton-proton (pp), proton-lead (p–Pb), xenon-xenon (Xe–Xe) and lead-lead (Pb–Pb) collisions delivered by the LHC in the years between 2015 and 2018 (known as Run2 phase). The center of mass energies of such collisions ranges between 900 GeV and 13 TeV. ALICE (A Large Ion Collider Experiment) was specifically designed to study ultra-relativistic heavy-ion collisions provided by the LHC. In these collisions, thanks to the unprecedented conditions of high energy density and temperature reached, a thermodynamic transition from standard hadronic matter to a deconfined phase is foreseen. Such an exotic state of hadronic matter is called Quark-Gluon Plasma (QGP) as partons, i.e. quarks and gluons, are not confined into hadrons. The conditions created with heavy-ion collisions at the LHC characterized the early Universe in its first microseconds and it is believed to be currently present in massive and dense objects as neutron stars. Due to the recent experimental observation of unexpected behaviors in the kinematics and dynamics of particle production in small collision systems (pp and p–Pb collisions), which resemble those expected when a deconfined phase is reached, new interest was prompted in the study of small colliding system features. Among all the light flavor particle species, light nuclei and strange particles are two outstanding examples of the large variety of measurements which can be performed to characterize the processes underlying high energy hadronic collisions, ranging from small to large collision systems.

The first part of this thesis work is devoted to the measurement of the production of light nuclei and antinuclei, whose formation in the early universe happened on time scales between 10 and 180 seconds, well before fusion in stars started to build-up heavier nuclei states. The measurement of the production spectra of protons, deuterons, helions and their antimatter counterparts is presented for pp collisions at $\sqrt{s} = 5.02$ TeV. Relying on this measurement,

the coalescence parameter B_{A}, which is related to the probability to form a nucleus via a coalescence process starting from nucleons, and the ratio between the integrated production yields of nuclei and protons are evaluated.
The second part consists of the measurement of multi-strange particles, the Ξ and Ω baryons, in Pb–Pb collisions at $\sqrt{s_{\mathrm{NN}}} = 5.02$ TeV. The presence of strange and multi-strange objects into the core of neutron stars is currently debated and could give an explanation for the existence of neutron stars with masses larger than twice the solar mass, which have been observed but are at present not accounted for by the most up-to-date equation of states. The production spectra of multi-strange baryons are presented and the ratio between their integrated yields and the production yields of pions are evaluated.
Both the results from light nuclei and multi-strange particles are reported as a function of the average charged particle multiplicity of the collision, and are compared to previous measurements performed by the ALICE experiment across different collision systems and to the up-to-date theoretical predictions. This comparison proves to be a useful tool to shed light on the dependence of the light flavor particle production mechanisms on the size of the hadronizing system only, without any dependence on the type of collision system or center of mass energy.
The results from the nuclei analysis have been approved by the ALICE collaboration and have been published [1], while those from multi-strange particles will be submitted for publication soon.

Contents

Chapter 1

High energy nuclear physics

The strong interaction between quarks and gluons, the elementary constituents of the hadronic matter, is described by a specific quantum field theory called Quantum Chromodynamics (QCD) [2]. The QCD theory predicts a phase transition from the ordinary hadronic matter to a color-deconfined state under conditions of extreme energy density. Such a deconfined state of matter, called Quark-Gluon Plasma (QGP), can be studied in the laboratory via heavy ion collisions at ultra-relativistic energies. In this Chapter, the key concepts of high-energy nuclear physics are introduced, together with a summary of the main experimental observables exploited in this fields.

1.1 Quantum chromodynamics

QCD describes the strong interaction between the particles of the Standard Model framework in terms of the elementary interactions between quarks and gluons, the fundamental constituents of matter. QCD is a non-Abelian quantum gauge field theory based on the invariance under local SU(3) group transformations. The existence of a new quantum number called color is stated and the $SU(3)_c$ is chosen as symmetry group of the theory [3]. As a convention, the color quantum number can come into three different states: red, green and blue. The symmetry group $SU(3)_c$ predicts the existence of eight massless vector bosons called gluons, which can carry a color and an anticolor charges. Gluons, whose existence is due to the symmetry group chosen for the theory, mediate the interaction between the fundamental fermionic fields of the theory, which are called quarks.

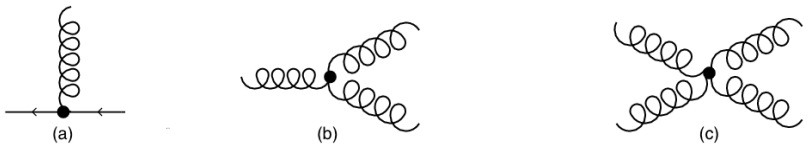

Fig. 1.1 QCD vertices with gluons: quark-quark-gluon (a), three gluons (b), four gluons (c).

The density of the Lagrangian of this theory is defined as

$$\mathscr{L}_{\mathrm{QCD}} = -\frac{1}{4} G^{\mathrm{a}}_{\mu\nu} G^{\mu\nu}_{\mathrm{a}} + i \sum_{\mathrm{f}} \bar{\psi}_{\mathrm{f}} (\not{\partial} - i g_{\mathrm{s}} \frac{\lambda^{\mathrm{a}}}{2} \not{A}_{\mathrm{a}} - m) \psi_{\mathrm{f}} \tag{1.1}$$

where $G^{\mu\nu}_{\mathrm{a}}$ represents the gauge invariant gluon field strength tensor

$$G^{\mathrm{a}}_{\mu\nu} = \partial_\mu A^{\mathrm{a}}_\nu - \partial_\nu A^{\mathrm{a}}_\mu + g_{\mathrm{s}} f^{\mathrm{abc}} A^{\mathrm{b}}_\mu A^{\mathrm{c}}_\nu \ . \tag{1.2}$$

The terms $\psi(x)$, g_{s}, λ^{a}, $A^{\mathrm{a}}(x)$ and f^{abc}, correspond to the quark fields expressed in the fundamental representation of $\mathrm{SU(3)_c}$, the coupling constant for the strong interaction, the Gell-Mann matrices, the gluon fields and the group structure constants, respectively. The main difference with respect to the well known theory of Quantum Eletrodynamics (QED) [4], which describes the electromagnetic interaction, lays in the non abelian nature of this group: since group structure constants are not null, additional vertices with gluon-only interactions are expected in addition to the "QED-like" vertex between two quarks and a gluon. A summary of the possible QCD vertices is reported in Fig. 1.1. The presence of self-interactions among gluons also reflects on the effective range of the strong interaction, which is dominant at a short distance scale, while vanishes over long ranges with respect to the electromagnetic force.

1.2 Confinement and asymptotic freedom

Peculiar features of the QCD can be derived by studying the strong coupling constant α_{s}. The value of α_{s} is driven by the interaction vertices that are allowed by the theory. When all the possible tree level interactions reported in Fig. 1.1 are considered, the strong coupling constant has the constant value $\alpha_{\mathrm{s}} = \frac{g_{\mathrm{s}}^2}{4\pi}$. Additional terms for higher order interactions, such as vertex corrections, self-energy and vacuum polarization, should anyway be considered to describe properly the theory. When accounting for both the tree-level and higher order interactions, the theory is no more convergent. In order to maintain its convergence, the theory needs to undergo a renormalization process and the α_{s} constant gains thus a dependence on

the squared transferred momentum Q^2 [5]. Such an evolution with Q^2 can be described as

$$\alpha_s(Q^2) = \frac{\alpha_s(\mu^2)}{1 + \frac{\alpha_s(\mu^2)}{12\pi}(33 - 2n_f)\ln\frac{Q^2}{\mu^2}} \tag{1.3}$$

where μ is the mass scale of the renormalization and n_f is the number of quark families, which is supposed to be three. This behavior is called running of the coupling constant and it is also observed for QED. The main difference between QED and QCD is due to the opposite sign of the first order correction, which is driven by the aforementioned interactions between gluons that are not permitted for photons in QED. The expected dependence of α_s on the transferred momentum has been confirmed by many experimental results and it is reported in Fig. 1.2. Depending on the value of Q^2 it is possible to distinguish between two extreme regimes of the QCD:

- Confinement
  For decreasing values of the transferred momentum, an exponential increase of the coupling constants is predicted and observed. In particular for a process with $Q <$ 1 GeV/c, α_s grows larger than unity, leading to a force strong enough to create hadrons without any possibility to observe free quarks or gluons. Another relevant feature of the QCD theory is that if the distance between the hadron constituents is increased, the separation energy raises linearly leading to a confinement of quarks and gluons. The usual perturbative approach is not suitable to describe confinement from the theoretical point of view, since α_s is large. For this reason an alternative approach has been developed in order to cope with this limitation and relies on the discretization of the four dimensional space-time. This method, called Lattice QCD (LQCD) [6], allows for the calculation of the Green's functions of the QCD Lagrangian on a discrete lattice and its performance depends on the computing resources available, thus on the granularity of the lattice. In the continuum limit, meaning for an infinite number of lattice points, it is possible to compare the experimental results with the calculations. LQCD was successfully exploited to determine the proton mass, with a precision of 2% [7].

- Asymptotic freedom
  In the large Q region the coupling constant decreases sizeably, becoming null for large enough transferred momentum. For this reason the usual perturbative approach to quantum field theories can be applied to study QCD. From the physical point of view this region is characterized by a vanishing interaction between quarks and gluons at very high energies, and this implies the possibility to observe them as free particles.

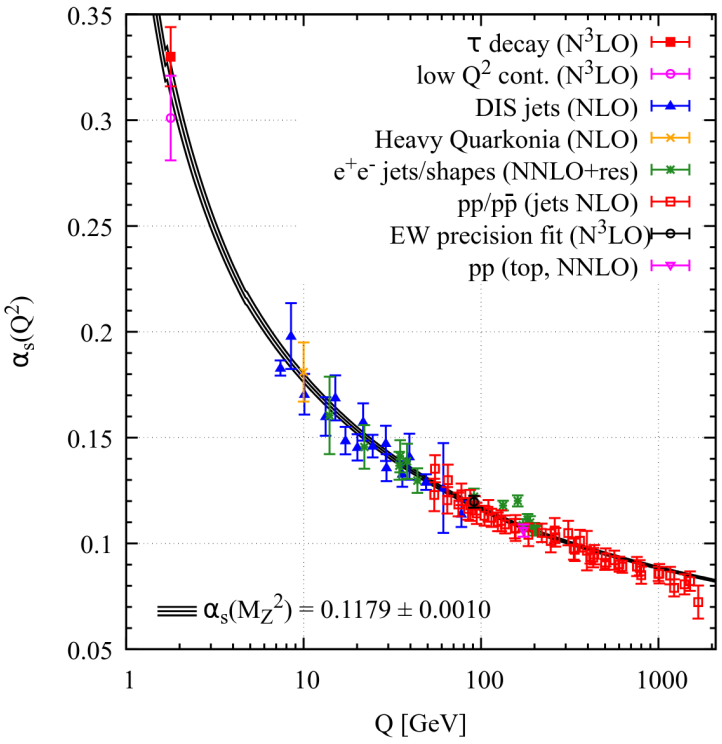

Fig. 1.2 Summary of the experimental values of α_s as a function of the transferred momentum Q. The black lines represents the theoretical expectations for α_s and its uncertainties. The figure is taken from [8]

This behavior is called asymptotic freedom and is a peculiar feature of non-abelian theories.

1.3 Quark-gluon plasma

As was described in the previous Section, the running of the strong coupling constant implies the existence of two extreme regimes for the hadronic matter. From the experimental point of view, different phases of the hadronic matter can be reproduced in the laboratory, depending on the energy scale of the hadron system. The study of these phases and of the transition between them is one of the key research interests in the field of high-energy physics. In order to perform such detailed study, a thermodynamical approach can be developed: considering a hadronic system with a finite number of degrees of freedom, its temperature T and chemical potential μ are taken into account. Since this potential is intended as the energy required to create a baryonic state it is called baryo-chemical potential μ_B. As was mentioned before,

the region of interest of the phase transition is not perturbative, thus the usage of LQCD or effective models is required. In the following, the predictions obtained via the MIT Bag Model [9] will be described.

1.3.1 MIT bag model

The MIT Bag Model is an effective model which relies on two very simple assumptions. First of all, quarks are considered as massless particles, so in principle they can move freely in space, but the spacial region they could access is limited and takes the name of bag. The second one states that the bag acts on quarks with an external pressure B to balance the kinetic energy coming from quark motion. This model can easily be linked to confinement and asymptotic freedom: confinement is obtained if the external bag pressure is large enough to bound quarks into hadron, whereas asymptotic freedom is reached if the internal pressure overcomes B, thus quarks are able to exit the bag. The external bag pressure can be evaluated from these assumptions as

$$B^{\frac{1}{4}} = \frac{\hbar c}{R}\left(\frac{2.04N}{4\pi}\right)^{\frac{1}{4}} \tag{1.4}$$

where R is the radius of the bag and N is the number of valence quarks. If their values are set to the experimental ones $R \approx 0.8$ fm and $N = 3$ for a hadron, the previous equation can be written as

$$B^{\frac{1}{4}} \simeq \frac{206\,\text{MeV}}{(\hbar c)^{\frac{3}{4}}}\,. \tag{1.5}$$

Thermodynamics shows that the internal energy of the system can be varied either increasing the system temperature T or enhancing the baryo-chemical potential μ_B.
Predictions on the critical values needed for T and μ_B to reach deconfinement can be obtained through the MIT Bag Model. If any of the aforementioned conditions is met, the color degrees of freedom are no more confined into hadrons, which are color singlets, thus quarks and gluons can move out of the bag. Such a peculiar state of matter is called Quark-Gluon Plasma (QGP) as an analogy to the classical idea of electron plasma. A so called cold QGP is formed when the net baryon density exceeds about five times the ordinary one, as happens in the core of massive neutron stars. In ultra-relativistic heavy ion collisions, where the net baryon density vanishes, a hot QGP is expected to be produced if a sufficiently large energy density ε is reached. For the hot QGP the MIT Bag Model predicts a critical temperature $T_\text{c} \simeq 145$ MeV and a critical energy density $\varepsilon \simeq 1$ GeV/fm^3. Similar results can be obtained via a LQCD approach, which leads to an expected value of $\varepsilon \simeq 0.5$ GeV/fm^3 at the same critical temperature.

1.3.2 QCD phase diagram

As mentioned before, effective models can give reliable predictions for QGP formation under a certain set of constraints. In order to avoid this limitation, it is necessary to use the non perturbative approach of LQCD, whose accurate predictions can also inspect intermediate T_c and μ_B values. Thanks to a precise scan in the space of T and μ_B, LQCD allows for the definition of a phase diagram of hadronic matter and for the calculation of the conditions needed for a phase transition to take place. A summary of the QCD phase diagram is reported in Fig. 1.3. The ordinary confined hadronic matter can be observed at temperatures of tens of MeV and a baryo-chemical potential $\mu_B \approx 1$ GeV. A QPG state can be exploited by enlarging sufficiently the energy density of the system, increasing either T or μ_B. For very low μ_B, LQCD calculations predict a smooth transition between the two phases of matter at a critical temperature $T_c \approx 165$ MeV. For larger temperature values, the momentum exchange between quarks and gluons is large, thus the strong coupling constant decreases and partons are no longer confined in color singlets. Such system conditions resemble the primordial universe ones. Moving to the extremely high baryon density and low temperature region, a color superconducting phase is expected [10]. This peculiar behavior is foreseen by some cosmological models [11] for the core of particular neutron stars. The order of a phase transition describes how the system's free energy varies when the transition temperature is reached. In particular, if the derivative of the system free energy is not continuous, a first order transition takes place. Otherwise, a second order transition occurs when the first time derivative is continuous but the higher order ones are not. Finally, a transition called crossover takes place if both the free energy and its derivatives are continuous. This particular kind of phase transition is predicted by LQCD calculations in the phase diagram region at low μ_B and high T and it is reported in Fig. 1.3 with a dashed blue line. A continuous blue line shows the first order transition which is expected for higher values of the baryo-chemical potential. A precise determination of the point which separates the two different phase transitions, called critical point, has not been performed yet and it is currently an open point in the field.

1.3.3 Heavy ion collisions

The theoretical effort discussed in the previous sections was aimed to describe as precisely as possible the different features of hadronic matter under extreme conditions. Anyway such predictions need to be tested from the experimental point of view. Indirect measurements of the hot and dense QCD matter at high temperatures and baryon densities come from

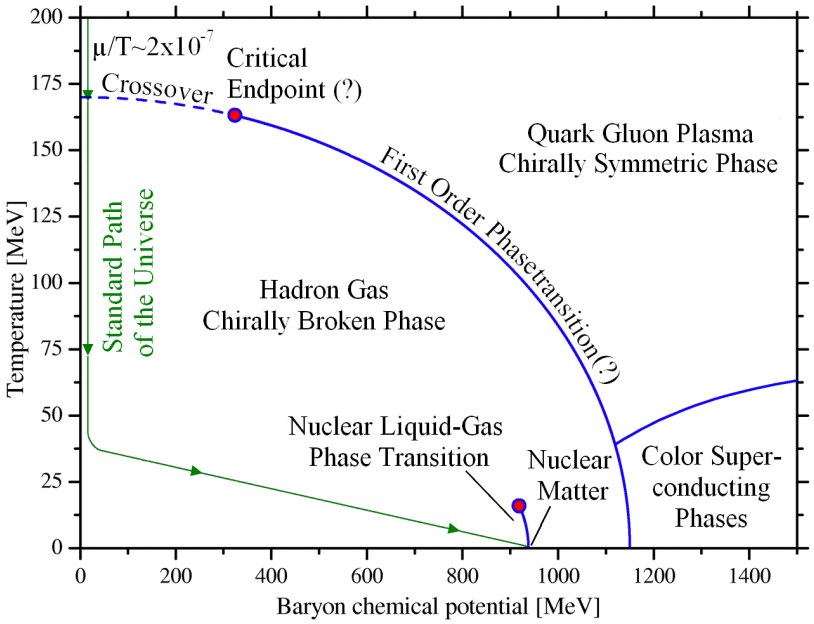

Fig. 1.3 QCD phase diagram in the temperature T and baryo-chemical potential μ_B space. For different combination of T and μ_B the corresponding phases of QCD matter are reported and are separated by blue lines. The green line shows the evolution of the matter produced in the Universe formation and expansion. Figure taken from [12]

cosmology [13, 14]: as was mentioned before, the core of massive neutron stars resemble the high μ_B and $T \approx 0$ GeV region, while the first instants of the Universe life were characterized by a deconfined phase at very high temperature and a subsequent phase transition to form hadrons.

A really unique tool to recreate the extreme conditions of high temperature in a laboratory is provided by heavy ion collisions at ultra-relativistic energies. Due to the large number of interactions which occur in the complex system formed by the collision, called fireball, the only way to give a proper description of the system is by using thermodynamics and statistical mechanics. Under the assumption of a long lived system, widely extended in space, thermal equilibrium can be stated due to the high number of interactions. Thus high energy nucleus-nucleus collisions can be described by using thermodynamic variables such as temperature and pressure. The space-time evolution of the fireball can be divided into different phases:

- Collision
  The collision is defined as the spacial superimposition of the two colliding nuclei and is characterized by a very short time τ_{coll}. The collision process lasts about 0.005 fm/c at the Large Hadron Collider (LHC) at CERN.

- Pre-equilibrium
  Secondary particles are produced from the inelastic interactions between nucleons of the colliding nuclei. At this stage of the collision, the system is not in equilibrium yet. A formation time τ_f is defined and it is estimated to be $\tau_f \approx 0.1$ fm/c at the LHC.

- QGP evolution
  The strongly interacting medium reaches equilibrium and expands. The system may be in a QGP state if the conditions for a phase transition are met as described in Sec. 1.3.2, otherwise the medium is characterized by a hadronic gas state. The conditions for QGP formation were met for the first time at the Relativistic Heavy Ion Collider (RHIC) at the Brookhaven National Laboratory (BNL) and then at the LHC. At the LHC, the time of thermal equilibrium is evaluated as $\tau_0 \approx 1$ fm/c from hydrodynamic considerations. The fireball space-time evolution with and without QGP formation is depicted in the right and left parts of Fig. 1.4, respectively.

- Hadronization
  If QGP has been formed, the fireball continues to cool down and to expand, until it reaches the critical value of energy density. At the LHC, with $\mu_B \approx 0$, this corresponds to a critical temperature $T_c \approx 160$ MeV. The hadronization process takes place, thus quarks and gluons are combined into baryons and mesons, and no more deconfined matter can be observed. Since a crossover is expected at the LHC running conditions, a smooth transition between the two phases is foreseen. Otherwise a first order transition, characterized by a mixed phase, would be expected. After the transition, the system is in a hadron gas state.

- Freeze-out
  Two freeze-out phases are observed while the cooling and expansion process goes on. When inelastic interactions are no longer permitted by the energy of the system, the chemical freeze-out takes place. From this moment the particle abundances are fixed, since hadrons can interact via elastic scatterings only. At the LHC the chemical freeze-out takes place when the temperature reaches a value of $T_{ch} \approx 150$ MeV. At $T_{fo} \approx 110$ MeV also the elastic collisions stop, thus the particle momenta are fixed. This final stage is called kinetic freeze-out.

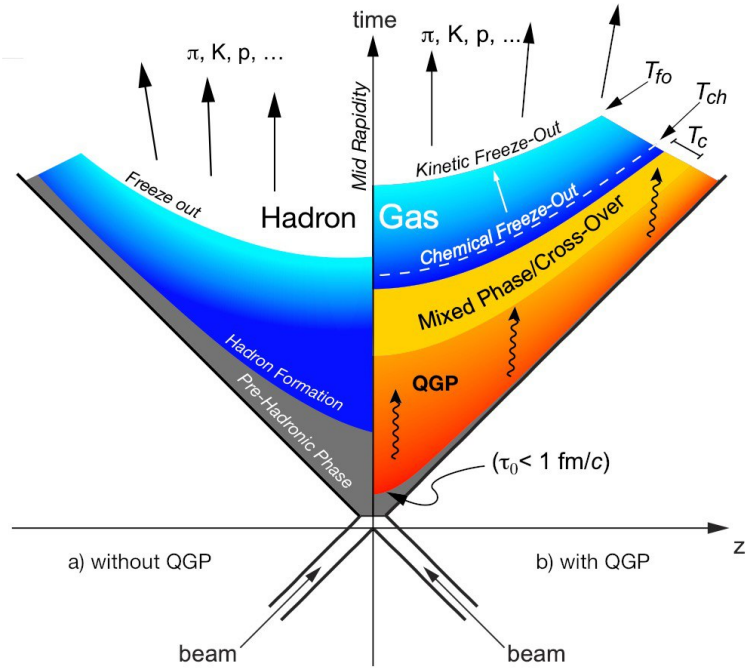

Fig. 1.4 Space-time diagram representing the evolution of a heavy ion collision with and without the formation of QGP (respectively on the right and on the left).

1.4 QGP probes

QGP formation can be experimentally tested through the measurement of the properties of the complex system produced in a ultra-relativistic heavy ion collision. Many different probes have been defined to characterize the QGP properties and its space-time evolution. These probes are mainly classified into three categories depending on their interaction with the system of particles produced in the hadronic collision: soft, hard and electroweak probes.

1.4.1 Soft probes

Soft hadrons, i.e. particles characterized by a low momentum, represent the majority ($\approx 99\%$) of the hadrons produced in an hadronic collision. The status of the emitting source can be described by studying the production of these particles: since at the kinetic freeze-out the elastic interactions between hadrons stop, soft probes provide indirect information about the late stages of the collision. Light flavour hadrons, made up of up, down and strange quarks, are considered as soft probes. Among this large variety of soft particles, light nuclei and strange particles play a crucial role and their study represents the subject of this work.

Radial flow Under the assumption of thermal equilibrium, in the low momentum region the spectra of the particles emerging from the system can be described at first order by a Boltzmann-Gibbs law as

$$\frac{1}{m_{\mathrm{T}}}\frac{\mathrm{d}^2N}{\mathrm{d}m_{\mathrm{T}}\mathrm{d}y} \propto e^{-\beta m_{\mathrm{T}}} \tag{1.6}$$

where $m_{\mathrm{T}} = \sqrt{m^2 + p_{\mathrm{T}}^2}$ is the transverse mass, which depends on the particle mass m and on its transverse momentum p_{T}. In this picture, a common emission temperature $T_{\mathrm{kin}} = 1/\beta$ drives the production of particles, and the particle production spectra are expected to have the same slope as a function of m_{T}, independently of the particle species. This behavior is called m_{T}-scaling [15] and was observed in pp collisions at low center of mass energy [16]. Nevertheless, deviations from this scaling law are observed in heavy ion collisions, where each particle spectrum shows a different slope, resulting in a different temperature [17]. This effect is clearly visible in Fig. 1.5, where the production spectra of pions, kaons and protons are reported as a function of the transverse momentum in Pb–Pb collisions at a center of mass energy $\sqrt{s_{\mathrm{NN}}} = 5.02$ TeV. The mass hierarchy going from pions to protons reflects into harder and harder spectra. This effect points to a decrease of temperature for higher mass

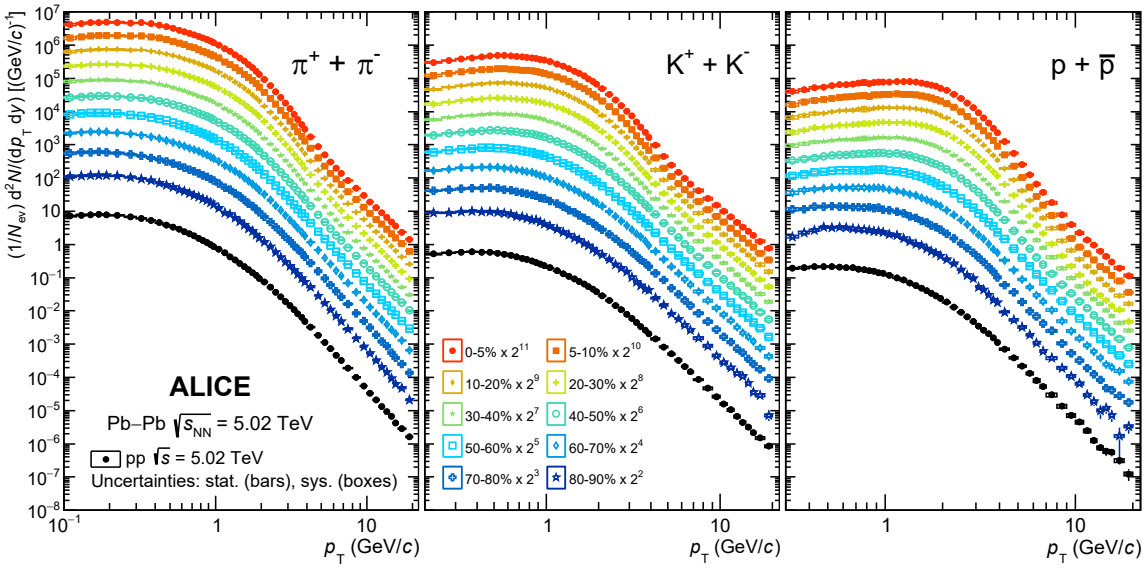

Fig. 1.5 Transverse momentum spectra of pions (left), kaons (center) and protons (right) in Pb–Pb collisions at $\sqrt{s_{\mathrm{NN}}} = 5.02$ TeV [18] for different centrality classes.

particles and can be interpreted as radial flow, i.e. a collective hydrodynamical expansion of all the particles along the transverse plane, caused by QGP induced pressure gradients.

Anisotropic flow The geometry of a nucleus-nucleus collision is schematically represented in Fig. 1.6 and is characterized by a finite impact parameter b. For increasing values of the impact parameter, the nuclei overlap region in the transverse plane becomes more and more anisotropic, leading to a peculiar almond-like shape of the interaction region. As a result, the collective flow of the medium is affected by anisotropic pressure gradients, due to the initial state spacial anisotropy. This effect reflects into azimutal anisotropies in the particle production spectra and can be studied with a Fourier expansion over the azimutal angle ϕ as

$$\frac{\mathrm{d}N}{\mathrm{d}\phi} \propto 1 + 2\sum_{n=1}^{\infty} v_{\mathrm{n}} \cos[n(\phi - \Psi_{\mathrm{n}})] \tag{1.7}$$

where the symmetry-plane angle Ψ_{n} is defined by the spatial distribution of the nucleons participating in the collision. For $n = 2$, the symmetry plane is equivalent to the reaction plane defined by the impact parameter vector and the momentum vectors of the colliding nuclei. The flow coefficients v_{n} account for the anisotropy with respect to the symmetry plane at the harmonic order n. Due to the shape of the interaction region, the second order flow coefficient v_2, called elliptic flow, is the dominant term in the Fourier expansion and its measurement is considered as a signature of QGP formation. Higher order coefficients are linked to

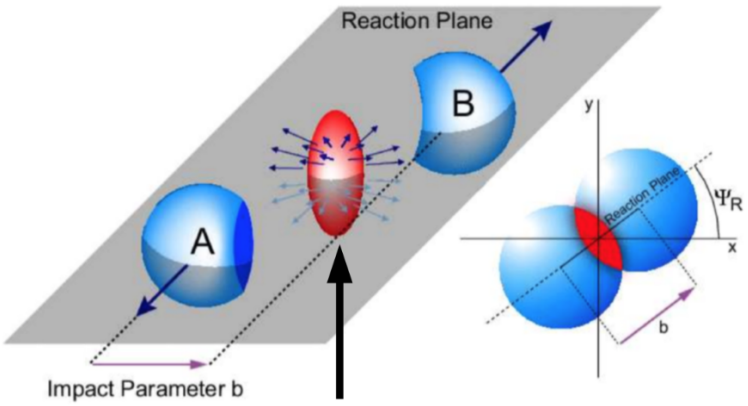

Fig. 1.6 Schematic representation of the geometry of a nucleus-nucleus collision. The overlap region of the two nuclei is represented in red, while the grey surface is the reaction plane. Figure adapted from [27].

non-homogeneous behaviors due to initial state fluctuations or non-linear hydrodynamical response of the medium [19, 20]. The integrated elliptic flow as a function of the center of mass energy $\sqrt{s_{\mathrm{NN}}}$ has been measured in different heavy ion experiments [21–23] and the measurements are reported in Fig. 1.7. A non-zero v_2, with a significantly increasing value going from RHIC to LHC energies is observed: a $\approx 30\%$ increase between Au–Au collisions at $\sqrt{s_{\mathrm{NN}}} = 200$ GeV and Pb–Pb collisions at $\sqrt{s_{\mathrm{NN}}} = 2.76$ TeV is present and is explained as an effect of the different average transverse momentum of the particles produced at different energies. For lower center of mass energy, the formation of QGP is not expected. In this region the elliptic flow is negative and the anisotropic emission of particles is driven by the presence of nucleons which are not involved in the collision and are responsible for the absorption of particles emitted along the reaction plane. Finally, at very low energies a steep rise to positive v_2 values is explained with the formation of a rotating system from the two colliding nuclei [23, 24]. The comparison between the measurements of the flow coefficients and the predictions from hydrodynamic models of the QGP, provides crucial constraints on the properties of the strongly interacting medium created in the collision, such as the bulk viscosity over the medium entropy ζ/s, its lifetime, and the shear viscosity to entropy ratio η/s [25, 26].

Strangeness enhancement The formation of a strongly interacting medium in heavy ion collisions is also expected to alter the relative abundances of light flavor particle species with respect to pp collisions. In particular, a larger production of strange hadrons, called strangeness enhancement [28], is foreseen if a QGP state is formed. In an ordinary hadronic

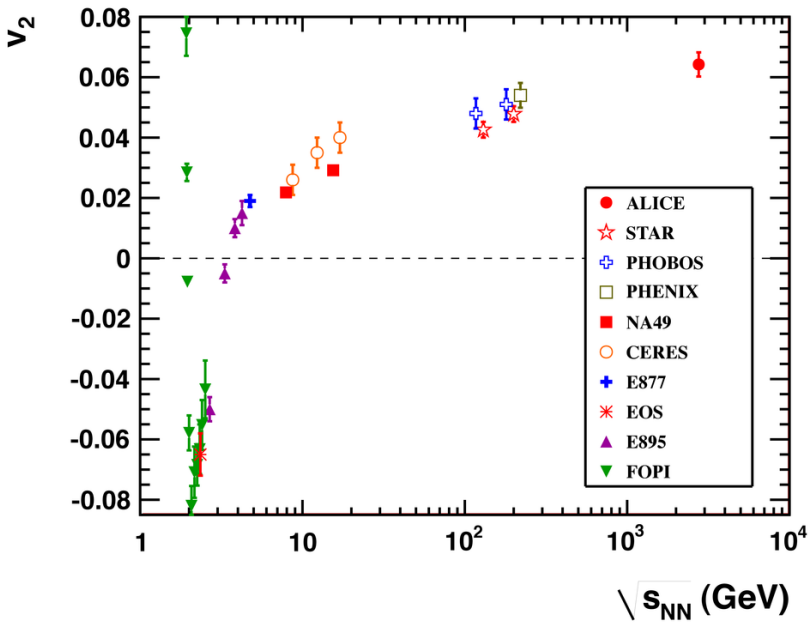

Fig. 1.7 Integrated elliptic flow as a function of the center of mass energy $\sqrt{s_{\mathrm{NN}}}$ measured in different experiments exploiting heavy ion collisions [21–23]. Each marker represent a result from a different experiment.

system, where the conditions for a phase transition to a QGP state are not met, the production of $\mathrm{s\bar{s}}$ pairs is strongly suppressed, since a kinematic threshold of about 1 GeV is due to the strange quark effective mass. However, in the QGP, chiral symmetry is restored [29], leading to a reduction of the strange quark mass of up to a factor 10. For this reason, a large production of $\mathrm{s\bar{s}}$ pairs is expected to be formed in the QGP via gluon fusion processes, resulting in an enhanced production of strange hadrons after the hadronization phase. This effect was observed in nucleus-nucleus collisions at different energies at the Super Proton Synchrotron (SPS) [30], at the RHIC [31] and at the LHC [32]. The ratios of the integrated yields of strange hadrons to the yields of pions are reported in Fig. 1.8 as a function of the average charged particle multiplicity at midrapidity $\langle \frac{\mathrm{d}N_{\mathrm{ch}}}{\mathrm{d}\eta_{\mathrm{lab}}} \rangle_{|\eta|<0.5}$. A significant increase in the strange to non-strange particle ratios is in general observed going from low multiplicity pp collisions (round markers) to Pb–Pb collisions (squared markers). Moreover, the observed enhancement becomes more and more pronounced as the strange quark content of hadrons is increased. These observations are considered as an important signature for the formation of a QGP state in Pb–Pb collisions. Moreover, a clear enhancement is also observed for the results obtained in pp collisions at a center of mass energy $\sqrt{s} = 7$ TeV when comparing the high multiplicity values ($\langle \frac{\mathrm{d}N_{\mathrm{ch}}}{\mathrm{d}\eta_{\mathrm{lab}}} \rangle_{|\eta|<0.5} \approx 20$) to the low multiplicity ones ($\langle \frac{\mathrm{d}N_{\mathrm{ch}}}{\mathrm{d}\eta_{\mathrm{lab}}} \rangle_{|\eta|<0.5} \approx 2$). This was the first observation of such an effect in pp collisions, and focused the experimental

attention on the so called small systems. It is currently under investigation whether the origin of this effect is connected to the formation of a deconfined QCD phase at high temperature and energy density in pp collisions as well.

1.4.2 Hard probes

High momentum particles and particles containing c and b quarks, called heavy flavor quarks, are produced via high transferred momentum processes, which take place in the early moments of the collision during the pre-equilibrium phase. The study of these hard probes is crucial, since they experience the whole evolution of the collision and they carry information about the medium in which they propagated.

Open heavy flavor An open heavy flavor particle, such as a D or a B meson, allows for the tagging of the specific heavy flavor quark which was responsible for the high transferred momentum process involved in the production of the particle itself. The study of open heavy flavor hadrons can be exploited via the measurement of the nuclear modification factor R_{AA}, which is defined as

$$R_{\mathrm{AA}} = \frac{1}{\langle N_{\mathrm{coll}} \rangle} \frac{\mathrm{d}^2 N_{\mathrm{AA}}/\mathrm{d}p_{\mathrm{T}}\mathrm{d}y}{\mathrm{d}^2 N/\mathrm{d}p_{\mathrm{T}}\mathrm{d}y} \tag{1.8}$$

where $\mathrm{d}^2 N_{\mathrm{AA}}/\mathrm{d}p_{\mathrm{T}}\mathrm{d}y$ and $\mathrm{d}^2 N/\mathrm{d}p_{\mathrm{T}}\mathrm{d}y$ are the particle production spectra measured in nucleus-nucleus and in pp collisions, respectively, and $\langle N_{\mathrm{coll}} \rangle$ is the average number of binary nucleon-nucleon collisions per AA event. In principle, if a nucleus-nucleus collision can be regarded as a simple superimposition of nucleon-nucleon collisions, the nuclear modification factor is expected to be identically to unity. Otherwise, if additional effects, such as the presence of a QGP state, enters the nucleus-nucleus interaction, a deviation from unity would be expected for the R_{AA}. Some additional cold matter effects, such as the Cronin enhancement [41] and the nuclear shadowing [42], are anyhow phenomena which can lead to deviations of the nuclear modification factor from such expectations. Cold matter effects can be distinguished with respect to effects due the formation of QGP by comparing nucleus-nucleus measurements with proton-nucleus results. The nuclear modification factor of D mesons, measured as a function of the transverse momentum for p–Pb collisions and for Pb–Pb collisions at $\sqrt{s_{\mathrm{NN}}} = 5.02$ TeV is reported in Fig. 1.9. The nuclear modification factor in Pb–Pb collisions (green, yellow, red points) is significantly smaller than unity for hard particles, meaning for $p_{\mathrm{T}} > 3$ GeV/c: this effect is linked to a decrease in the numerator of Eq. 1.8, due to the interaction of the D mesons with the medium produced in the nucleus-nucleus collision. On the contrary, the p–Pb reference (blue points) is compatible with unity,

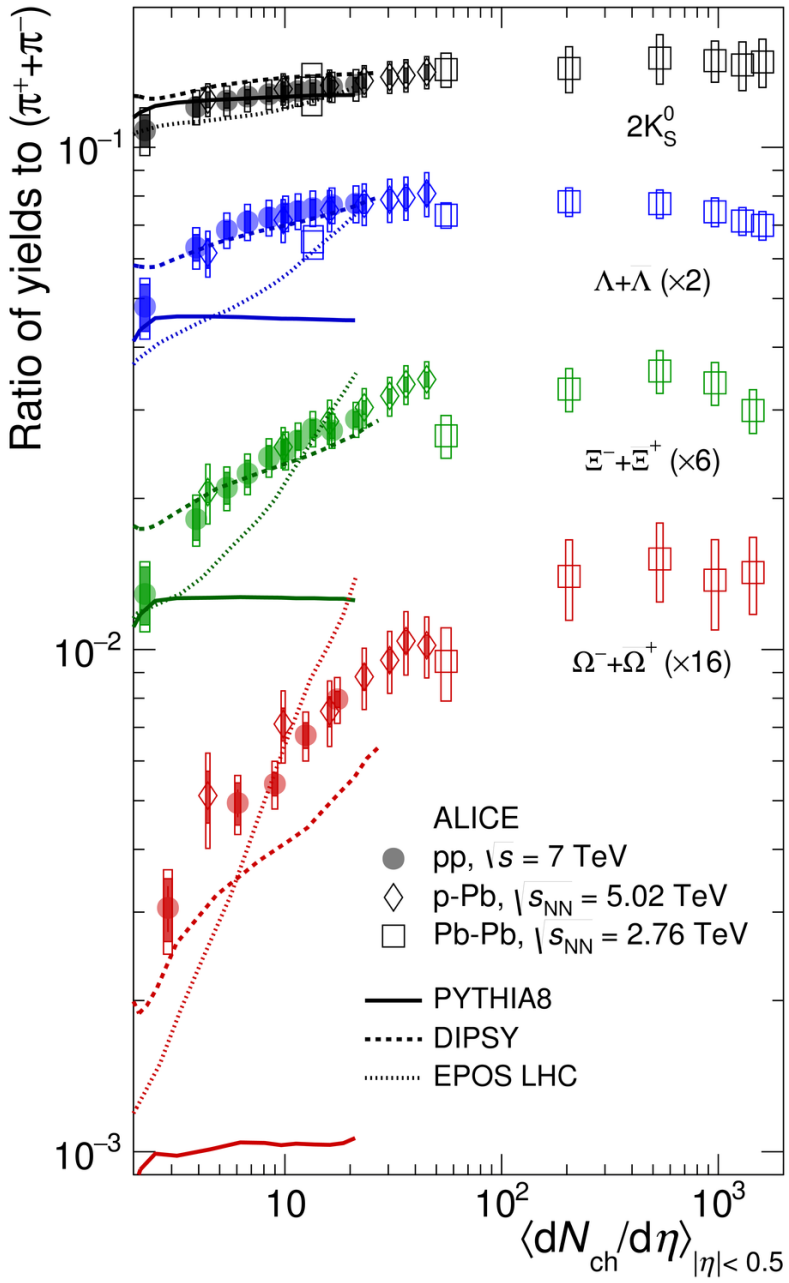

Fig. 1.8 Ratios between the integrated yields of strange hadrons and pions as a function of the average charged particle multiplicity measured at midrapidity $\langle \frac{dN_{ch}}{d\eta_{lab}} \rangle_{|\eta|<0.5}$. K^0_s (black), Λ (blue), Ξ (green) and Ω (red) particles measure in pp collisions at 7 TeV [33, 34], in p–Pb collisions at 5.02 TeV [35, 36] and in Pb–Pb collisions at 2.76 TeV [32, 37] are reported. The values are compared to calculations from MC models [38–40].

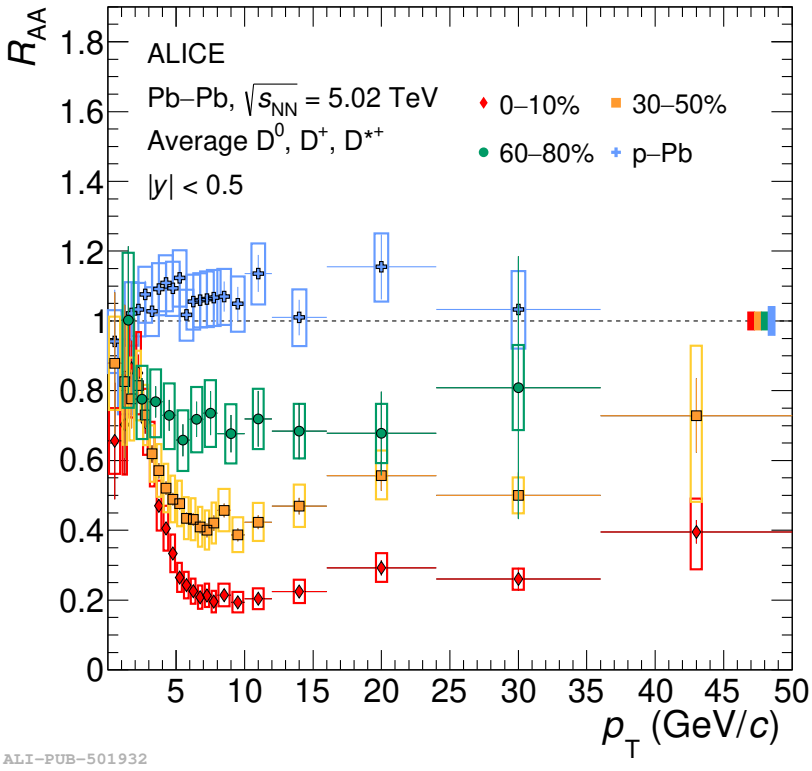

Fig. 1.9 Nuclear modification factor for the average of D^0, D^+ and D^{*+} mesons as a function of p_T measured in p–Pb collisions at $\sqrt{s_{NN}} = 5.02$ TeV [46] (blue) and in Pb–Pb collisions at $\sqrt{s_{NN}} = 5.02$ TeV [47, 43]. For the Pb–Pb results, three centrality classes are reported (green, yellow, red).

confirming that the suppression observed in Pb–Pb collisions is due to final-state effects induced by the formation of a hot and dense QGP medium. Additional studies of the nuclear modification factor are performed to understand the nature of the energy loss of heavy flavor particles in the QGP: the energy loss in the medium can be either collisional, being caused by the elastic scatterings with other particles, or radiative, due to inelastic scatterings. A combination of the two effects is currently considered as the explanation for the energy loss of heavy flavor particles in the QGP [43]. Finally, another relevant topic related to open heavy flavour physics is the study of the dead cone effect [44], whereby the gluon radiation emitted by a particle of mass m and energy E is suppressed at angular scales smaller than m/E with respect to the direction of the particle momentum. The direct observation of the dead cone effect in Pb–Pb collisions was achieved by the ALICE experiment [45] by tagging jets with a fully reconstructed charmed hadron, paving the way for a detailed characterization of the high-temperature phase of QCD matter in heavy ion collisions.

Quarkonium suppression QGP properties are also investigated through the study of quarkonium states, the bound states $c\bar{c}$ (charmonium) and $b\bar{b}$ (bottomonium). The suppression of the number of observed charmonium states in heavy ion collisions with respect to pp collisions, called charmonium suppression, is considered as a signature of a deconfined phase, and it is also sensitive to the temperature of the system [48, 49]. The main difference about $q\bar{q}$ states in the vacuum and in the QGP is due to the binding energy of the pair. In the vacuum it can be expresses through the Cornell potential as

$$V(r) = kr - \frac{\alpha}{r} \tag{1.9}$$

where r is the distance between the two quarks, k is called string tension and α is a Coulomb-like constant. For small distance scales, r is small and the second term is dominant, leading to a Coulomb-like potential. At large distances the linear term is dominant and it is responsible for the confinement phenomenon. However, in a deconfined phase, color charges are free and no deconfinement is observed, thus a new potential can be defined as

$$V'(r) = -\frac{\alpha}{r} e^{-\frac{r}{\lambda_D}} \tag{1.10}$$

where the new parameter λ_D is called Debye length. This potential resembles the one observed for a plasma of electrons and protons [50], where a screening effect is present. The extension of the color screening region, which defines the maximum distance between two quarks for the bound state to be formed, is driven by the Debye length and depends on the temperature of the system: the Debye length decreases with the increase of the QGP temperature, leading to a quarkonium suppression as the temperature increases. The R_{AA} of the J/ψ meson, the charmonium ground state, is reported in Fig. 1.10 as a function of the number of participant nucleons N_{part} which are involved in the collision. The measurement performed by the PHENIX Collaboration in Au–Au collisions at $\sqrt{s_{NN}} = 200$ GeV (left, black) is significantly lower than the result obtained by the ALICE experiment in Pb–Pb collisions at $\sqrt{s_{NN}} = 2.76$ TeV (left, red). This observation can be explained by the charmonium regeneration effect [51]: although in principle at higher energies a larger suppression would be expected, this is partially compensated by the statistical recombination of charm and anticharm quarks which are produced in uncorrelated hard scattering processes. As expected, this effect is particularly relevant in the low transverse momentum region ($p_T < 8$ GeV/c) exploited by the ALICE experiment. At higher transverse momentum ($6.5 < p_T < 30$ GeV/c), the CMS measurement [52] (right, red) shows a significantly lower nuclear modification factor with respect to the one measured by the ALICE experiment, since the quarkonium regeneration effect is expected to become negligible moving to high transverse momentum

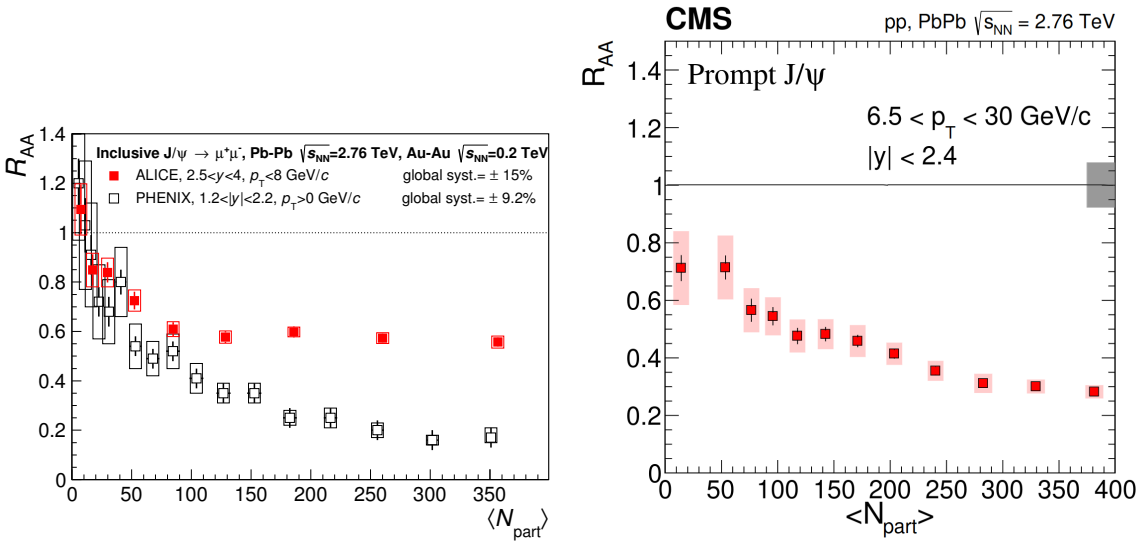

Fig. 1.10 Left: nuclear modification factor for the J/ψ meson as a function of the number of participant nucleons measured by the ALICE experiment in Pb–Pb collisions at $\sqrt{s_{\rm NN}} = 2.76$ TeV [53] (red) and by the PHENIX collaboration in Au–Au collisions at $\sqrt{s_{\rm NN}} = 200$ GeV [58] (black). Right: nuclear modification factor for the J/ψ meson as a function of the number of participant nucleons measured by the CMS experiment in Pb–Pb collisions at $\sqrt{s_{\rm NN}} = 2.76$ TeV [52]

values. Similar measurements have been performed for other charmonium states [53–55], and for the bottomonium [56, 57], even though for the latter a regeneration effect is not observed at LHC energies, due to the small number of b quarks produced.

Jet quenching A directional emission of particles produced by the hadronization of a quark or a gluon generated in a hard scattering process is known as jet. In the vacuum, due to momentum conservation, pairs of jets are typically produced in a back-to-back topology and with equal momentum. In a nucleus-nucleus collision, the partons will interact with the deconfined medium reducing their energy and changing their direction, leading to a modification of this configuration. As a consequence, depending on the length of the path followed by each parton inside the medium, the two jets are characterized by different energies: the most energetic one takes the name of leading jet, while the other one is called recoil jet. The ratio $\Delta I_{\rm AA}$ between the transverse momentum spectra of the recoil jet in Pb–Pb and pp collisions at $\sqrt{s_{\rm NN}} = 2.76$ TeV measured by the ALICE experiment [59] is reported in Fig. 1.11. The suppression of the recoil jet spectra in Pb–Pb collisions with respect to pp collisions is evident, indicating a larger energy loss in Pb–Pb collisions due to the presence of a deconfined medium. Additional measurements are exploited to characterize the effect of the QGP on the structure of the jet. In particular, the study of the nuclear modification

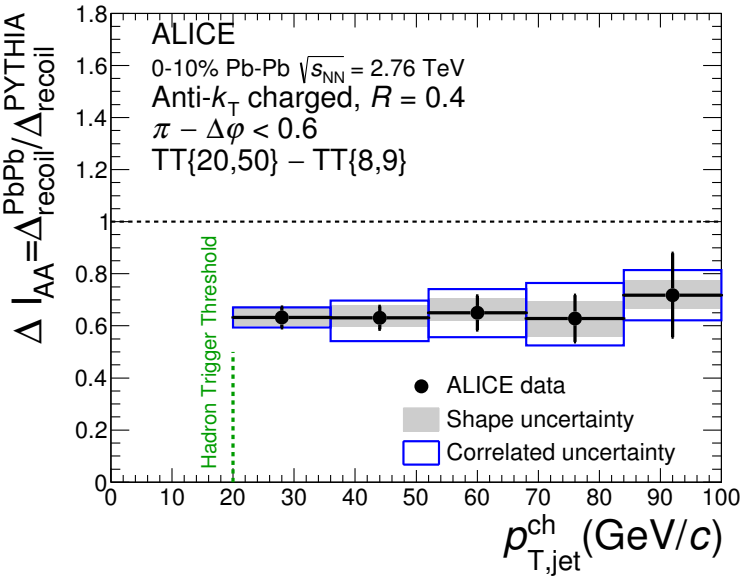

Fig. 1.11 Ratio between the recoil jet spectra measured in Pb–Pb collisions at $\sqrt{s_{\mathrm{NN}}} = 2.76$ TeV [59] and in pp collisions at the same center of mass energy. The spectrum for pp collisions is calculated using the PYTHIA event generator [61].

factor of jets [60] indicates that the interactions with the medium broadens the jet structure, transporting a portion of the parton energy at large angles from the hard-scattered parton direction.

1.4.3 Electroweak probes

In the Standard Model, leptons, Z and $W^{\pm}$ bosons are not coupled to the strong interaction, arising as color blind probes to directly and efficiently test the very first stages of the hadronic collision and the nature of the strongly interacting medium created by the nucleus-nucleus collision. For this reason, no modification of the production spectra of these particles is expected in heavy ion collisions with respect to pp collisions, except for the scaling due to the different number of elementary collisions. Measurements of the nuclear modification factor of the Z boson [62, 63] showed that this expectation is confirmed, and that the Z boson spectra are not influenced by the presence of QGP.
Another interesting probe is provided by photons, since no interaction at the tree level is expected with the QGP. Nevertheless, the deconfined medium emits thermal photons which can not be distinguished by the ones produced in the initial stages of the collision. The production spectra of direct photons, i.e. not produced by hadron decays, are reported in

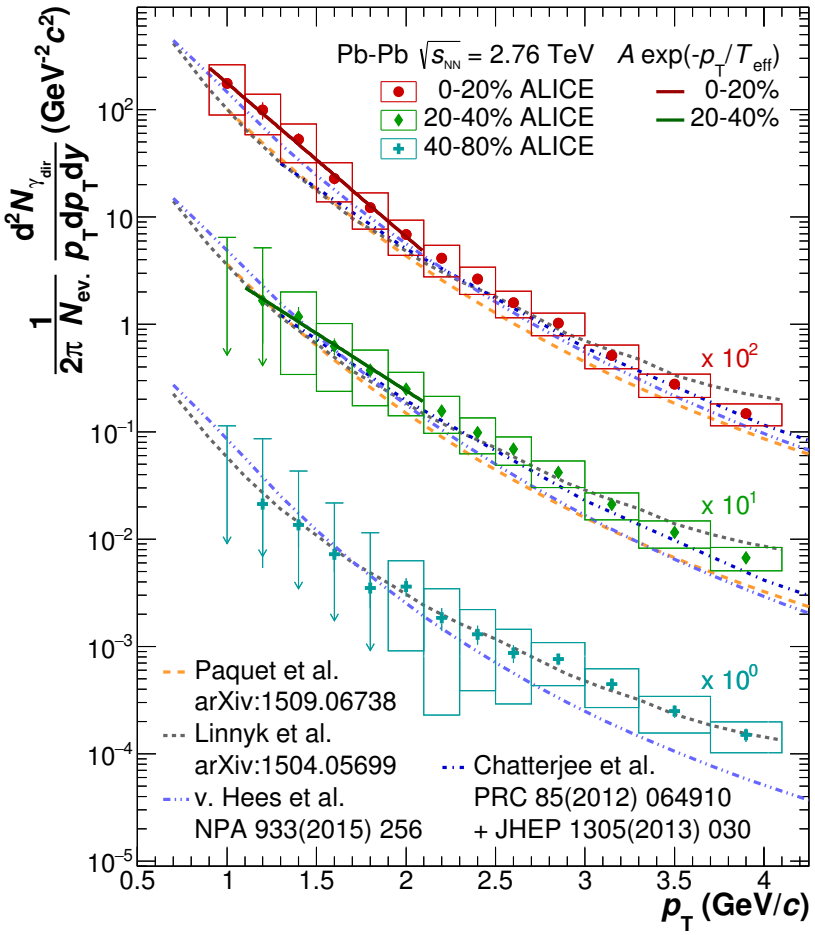

Fig. 1.12 Direct photon spectra in Pb–Pb collisions at $\sqrt{s_{\rm NN}} = 2.76$ TeV [64] for three different centrality classes. Predictions from models including the contribution from thermal photons emitted by the QGP [65–68] are also reported.

Fig. 1.12 for Pb–Pb collisions at $\sqrt{s_{\rm NN}} = 2.76$ TeV. In the low $p_{\rm T}$ region, the measured spectra are in agreement with the models taking into account both photons produced in the collision and emitted as thermal radiation by the QGP. Additionally, for $p_{\rm T} > 5$ GeV/c the spectra are described properly by perturbative QCD calculations for pp collisions scaled by the number of elementary collisions, confirming that this region of the spectra is dominated by photons produced in hard scatterings.

Chapter 2

The ALICE experiment

Among the four largest experiments at the Large Hadron Collider (LHC) [69], ALICE (A Large Ion Collider Experiment) [70] is the one mainly devoted to the study of heavy ion collisions at ultra-relativistic centre-of-mass energies. In this Chapter, a detailed description of the detectors composing the ALICE experiment will be given. The software framework and the detector performance will be also discussed.

2.1 The Large Hadron Collider

The Large Hadron Collider is the largest particle accelerator and hadronic collider in the world. It is formed of a two-ring structure whose circumference measures 26.7 kilometers, and it is located at the European Organization for Nuclear Research (CERN) near Geneva, between Switzerland and France. Thanks to a complex pre-acceleration chain, it was designed to work with protons, Xe and Pb ions at the TeV energy scale. The representation of the whole accelerating complex, which starts from smaller accelerators and ends up into the LHC, is reported in Fig. 2.1.
Thanks to a complex chain of pre-acceleration steps, protons and ions are injected into the LHC, where they finally reach their target center of mass energy. During its Run2 phase the LHC mainly delivered pp collisions at a center of mass energy of $\sqrt{s} = 5.02$, $\sqrt{s} = 7$, $\sqrt{s} = 8$ and $\sqrt{s} = 13$ TeV and Pb–Pb collisions at $\sqrt{s_{\rm NN}} = 5.02$ TeV, depending on the data taking period. The LHC also provided proton-lead (p–Pb) collisions at $\sqrt{s_{\rm pN}} = 5.02$ TeV and $\sqrt{s_{\rm pN}} = 8.16$ TeV and xenon-xenon (Xe–Xe) collisions at $\sqrt{s_{\rm NN}} = 5.44$ TeV.
The LHC supplies beams crossing in four intersection points, where the largest experiments seat, as illustrated in Fig. 2.1. They are:

- A Large Ion Collider Experiment (ALICE)
  A detector designed to study heavy ion collisions at ultra-relativistic centre-of-mass energies. The main goal of the ALICE experiment is the characterization of strongly interacting matter at extreme energy densities, with a particular focus on Quark-Gluon Plasma formation. The physics program of the experiment also includes the study of proton-nucleus and proton-proton collisions to address various QCD topics and to understand collective phenomena observed in small collision systems which are reminiscent of the behavior observed in heavy ion collisions.

- Compact Muon Solenoid (CMS)
  A general-purpose detector mainly aimed at the detection of the Higgs boson. Supersymmetry and dark matter searches are also carried out.

- A Toroidal LHC Apparatus (ATLAS)
  A multi-purpose experiment with detection techniques complementary to the CMS ones. It has been designed to perform both searches for physics beyond the Standard Model and precision measurements, together with the Higgs boson measurement.

- LHC beauty (LHCb)
  An experiment designed to investigate the physics of beauty quarks. The main goals of the experiment are the study of CP violation and the search for physics beyond the Standard Model, both of them performed in the B-meson sector.

2.2 ALICE design

In order to study the QCD matter created in ultra-relativistic heavy ion collisions, the ALICE detector is required to have a very efficient tracking system with a large solid angle coverage (acceptance) and very good particle identification (PID) capabilities, in particular in the low momentum region. These requirements must be fulfilled in a challenging environment, where an average of ≈ 2000 charged particles per rapidity unit is created in central Pb–Pb collisions. From the detector point of view, high granularity and low material budget are fundamental to cope with the unprecedented high number of particles produced and traversing the detectors. In the reconstruction process, two default coordinate systems are used by the ALICE apparatus. The first one is a right-handed orthogonal Cartesian system with the origin settled at the nominal beams interaction point, with the x axis aligned with the horizontal accelerator plane and pointing to the centre of the LHC. Since the y axis points upward, the z axis is parallel

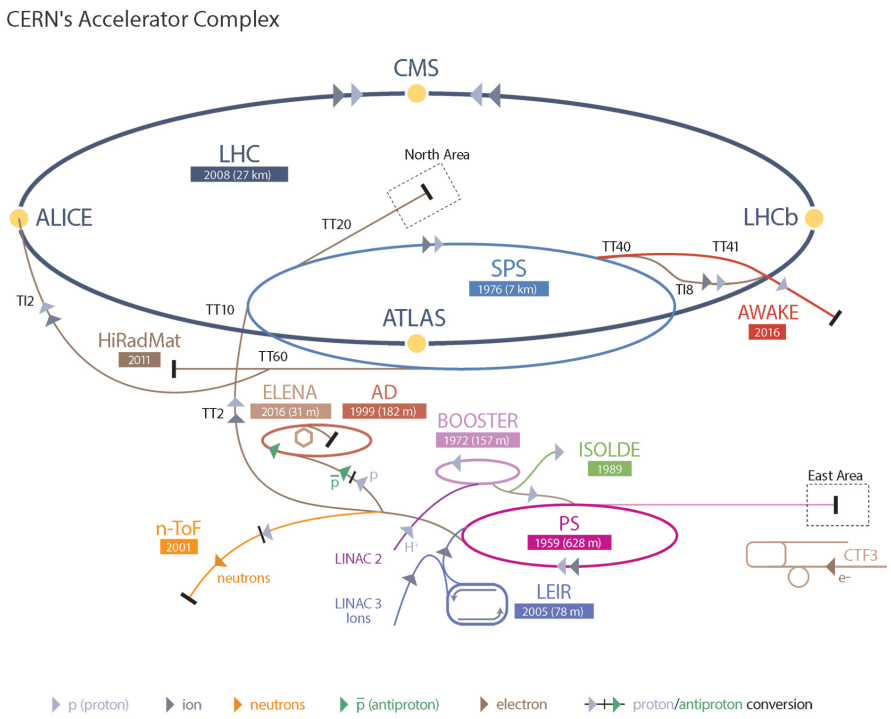

Fig. 2.1 Schematic view of the accelerator complex at CERN. Figure adapted from [71].

to the beam direction and its positive direction is defined by the chirality of the reference system. The other system, based on cylindrical-like coordinates, can be defined starting from the Cartesian one. With the same z axis, two angles are defined: the azimuthal angle ϕ, increasing counter-clockwise starting from $\phi = 0$ from the x axis with the observer standing at positive z, and the polar angle θ, increasing in the range $[0, 2\pi]$ going from z to -z.
Through the usage of these two coordinate systems, new variables can be defined in order to describe in an easier way the position of a particle with respect to the interaction point. The rapidity is defined as

$$y = \frac{1}{2} \log \left(\frac{E + p_z}{E - p_z} \right) \tag{2.1}$$

where $p^\mu = (E, \vec{p})$ is the four-momentum of the particle. Since the evaluation of rapidity is non-trivial, due to the dependence on energy and momentum measurements, another quantity called pseudorapidity is introduced as

$$\eta = \frac{1}{2} \ln \frac{|p| + p_z}{|p| - p_z} = -\ln \left[tan \left(\frac{\theta}{2} \right) \right] . \tag{2.2}$$

The ALICE apparatus is formed by three main parts:

- Central Barrel
  Detectors located in the central pseudorapidity region, with a coverage of about $|\eta| < 0.9$, mainly devoted to tracking and particle identification. For this purpose, a solenoidal magnetic field $B = 0.5$ T is produced in this region by a resistive magnet previously used for the L3 [72] experiment at the Large Electron Positron collider at CERN. Tracking detectors are the Inner Tracking System (ITS), the Time Projection Chamber (TPC) and the Transition Radiation Detector (TRD). These detectors, together with the Time Of Flight (TOF) and the High-Momentum Particle Identification (HMPID), can also be exploited for particle identification. Additional detectors have specific goals: the physics of high p_{T} photons and jets is explored thanks to the ElectroMagnetic Calorimeter (EMCal) and the Photon Spectrometer (PHOS), while the ACORDE, an array of 60 large scintillators, is devoted to the study of high-energy cosmic rays.

- Muon Spectrometer
  With a pseudorapidity coverage of $-4 < \eta < -2.5$, it is dedicated to the study of heavy-quark vector mesons. It is composed by a front absorber with small atomic number Z, a spectrometer with five tracking stations placed inside a dipole magnet and four trigger planes situated behind an iron wall.

- Other forward Detectors
  They cover the forward-backward pseudorapidity regions as close as possible to the beam line and are devoted to auxiliary measurements which can complement the main measurements performed by the central barrel detectors. They include a Forward Multiplicity Detector (FMD), which is a silicon strips detector, the Photon Multiplicity Detector (PMD), the Zero Degree Calorimeters (ZDC), consisting of two hadronic calorimeters for protons and neutrons, and an electromagnetic calorimeter. In addition to such detectors, a scintillator hodoscope, the VZERO (V0), and a Cherenkov-based counter, the TZERO (T0), are located at each side of the interaction point.

The overall layout of the ALICE experiment and detectors is reported in Fig. 2.2, together with some additional details in Table 2.1.

2.3 The ALICE detector

The different characteristics of each ALICE sub-detector grant the possibility to perform a large variety of physics studies, ranging from the measurement of charged particle produc-

	Acceptance		
Detector	Polar	Azimuthal	Main purpose
SPD	$\|\eta\| < 2.0$	full	tracking, vertex, trigger
	$\|\eta\| < 1.4$	full	tracking, vertex, trigger
SDD	$\|\eta\| < 0.9$	full	tracking, PID
	$\|\eta\| < 0.9$	full	tracking, PID
SSD	$\|\eta\| < 1.0$	full	tracking, PID
	$\|\eta\| < 1.0$	full	tracking, PID
TPC	$\|\eta\| < 0.9$	full	tracking, PID
TRD	$\|\eta\| < 0.8$	full	tracking, $e^{\pm}$ id, trigger
TOF	$\|\eta\| < 0.9$	full	PID
PHOS	$\|\eta\| < 0.1$	$220° < \phi < 320°$	γ, trigger
EMCal	$\|\eta\| < 0.7$	$80° < \phi < 187°$	γ, jets, trigger
HMPID	$\|\eta\| < 0.6$	$1° < \phi < 59°$	PID
ACORDE	$\|\eta\| < 1.3$	$30° < \phi < 157°$	cosmic rays, trigger
PMD	$2.3 < \eta < 3.9$	full	γ
FMD	$3.6 < \eta < 5.0$	full	ch. particles
	$1.7 < \eta < 3.7$	full	ch. particles
	$-3.4 < \eta < -1.7$	full	ch. particles
V0A	$2.8 < \eta < 5.1$	full	ch. particles, trigger
V0C	$-3.7 < \eta < -1.7$	full	ch. particles, trigger
T0A	$4.6 < \eta < 4.9$	full	time, vertex, trigger
T0C	$-3.3 < \eta < -3.0$	full	time, vertex, trigger
ZDC	$\|\eta\| > 8.8$	full	forward n, trigger
	$6.5 < \eta < 7.5$	$\|\phi\| < 10°$	forward p, trigger
	$4.8 < \eta < 5.7$	$\|\phi\| < 32°$	γ, trigger
MCH	$-4.0 < \eta < -2.5$	full	μ tracking
MTR	$-4.0 < \eta < -2.5$	full	μ trigger

Table 2.1 Geometrical acceptance and main purposes of the ALICE sub-detectors. When more than one position value is specified the detector is divided in two or several parts. This table has been taken and adapted from the description of the ALICE apparatus in [70].

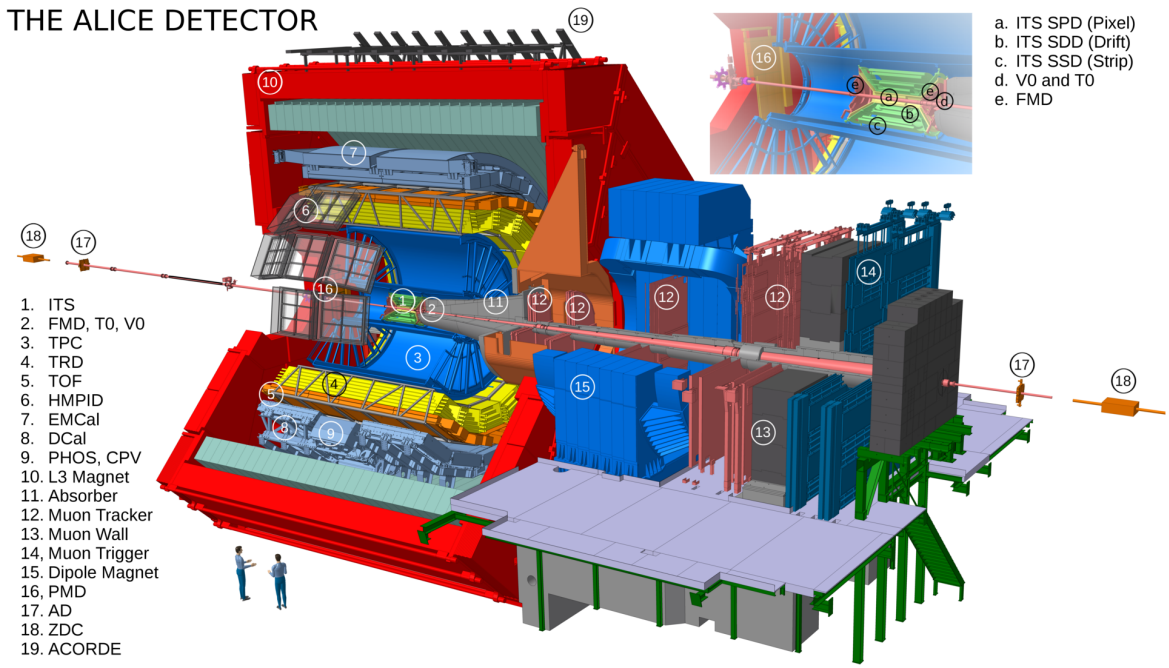

Fig. 2.2 The overall ALICE experimental setup. The top right inset shows a zoom on the V0, T0, FMD and the ITS detectors. Figure taken from the ALICE figure repository ©.

tion to the reconstruction of flavour-tagged jets. In particular, for the measurement of the production of nuclei and strange particles which are described in this work, some detectors play a crucial role:

- ITS for the reconstruction of primary and secondary vertices, and for tracking;
- TPC for PID and tracking;
- TOF for PID;
- V0 for the evaluation of the multiplicity or centrality of the events, for proton-proton or Pb–Pb collisions, respectively;
- T0 for the measurement of the collision time.

These sub-detectors are described in detail in the next sections.

2.3.1 Inner Tracking System (ITS)

The ITS [73] is the innermost detector of the ALICE experiment and it is mainly devoted to vertex and track reconstruction. Its six cylindrical layers of silicon surround the beam

Sub-detector	r (cm)	z (cm)	Active area (m^2)	Channels
SPD (1^{st} layer)	3.9	14.1	0.07	3276800
SPD (2^{nd} layer)	7.6	14.1	0.14	6553000
SDD (3^{rd} layer)	15.0	22.2	0.042	43008
SDD (4^{th} layer)	23.9	29.7	0.89	90112
SSD (5^{th} layer)	38.0	43.1	2.20	1148928
SSD (6^{th} layer)	43.0	48.9	2.80	1459200

Table 2.2 Dimensions of the ITS layers [73].

vacuum tube and are organized in couples based on different technologies. The two innermost layers are made of Silicon Pixel Detectors (SPD), whose high granularity is necessary to achieve excellent resolution on the impact parameter and on the vertex position, even in the high particle multiplicity environment of heavy ion collisions. Thanks to a total amount of $9.8 \cdot 10^6$ cells, the SPD can achieve a spatial resolution of 12 μm and 100 μm in the $r\phi$ and z direction, respectively. For the two intermediate layers Silicon Drift Detectors (SDD) have been chosen, in order to cover a larger area with a relatively small number of chips and front-end electronics. In particular, a spatial resolution of 38 μm in the $r\phi$ direction and ranging from 25 μm up to 60 μm in the z direction can be reached. Finally, Silicon Strip Detectors (SSD) have been chosen for the two outer layers, granting a resolution of 20 μm and 800 μm in the $r\phi$ and z directions, respectively. The outlook of the different ITS layers is reported in Table 2.2.

The excellent spatial resolution of the ITS layers mainly lead to a very precise reconstruction of the primary vertex position with a resolution better than 100 μm in pp collisions. Moreover this allows to easily separate primary vertices from secondary ones which are coming from the weak decays. Moreover the SDD and the SSD analogue read-out allows for particle identification via specific energy loss ($\frac{dE}{dx}$) measurements. In order to improve the ITS performances at very low momentum, a low amount of material budget was employed: the detector effective thickness, measured in units of the radiation length X_0, is about 0.4%. This is a major feature which helps to improve the ITS resolution, since low p_T particles are affected by multiple scattering within the detector material. Including the shields and support structures, the total material traversed by a particle crossing the ITS, at $\eta = 0$, is around 7.2% of X_0. Such a configuration is very important to complement the TPC capabilities in terms of tracking and PID: with the ITS measurement it is possible to extend the tracking of low p_T particles down to 80 MeV/c and the PID to particles with momentum below 200 MeV/c.

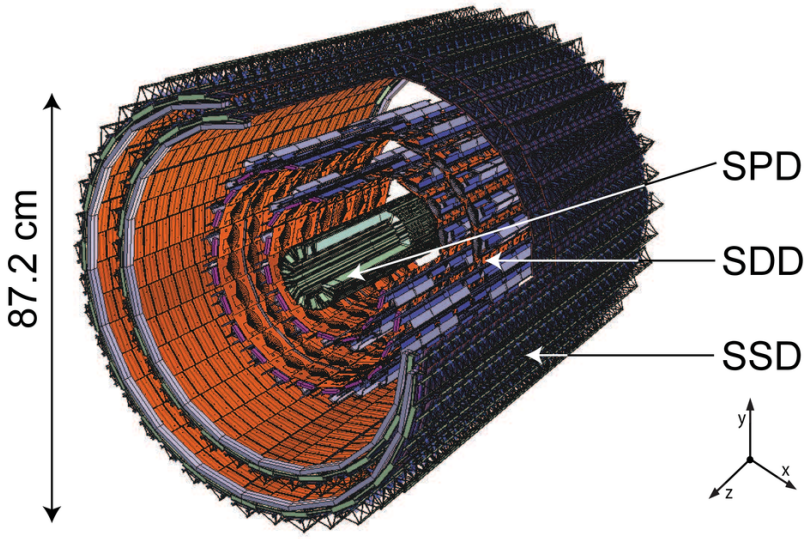

Fig. 2.3 View of the ITS silicon layers. Figure from [74].

2.3.2 Time Projection Chamber (TPC)

The TPC [75] is a gaseous ionization detector formed by a cylindrical chamber which is closed by two end-plates, whose main purposes are track reconstruction and charged particle identification via $\frac{dE}{dx}$. With its overall length of 500 cm, inner radius of 80 cm and outer one of 250 cm, it is the largest detector of the central barrel and it covers a pseudorapidity range of $|\eta| < 0.9$. The electrons produced via ionization by the charged particles traversing the detector gas travel towards the read-out detectors placed at the end plates through a mixture of high-purity gas. The original mixture was 90% Ne and 10% CO_2, then an additional 5% of N_2 was added to provide a more stable operation of the readout chambers at high gain. The Ne was replaced with Ar for the data taking of 2015, 2016 and 2018 to achieve a more stable behavior over a long data taking period. A central 100 kV electrode and two axial resistive potential dividers are devoted to generate a highly uniform electrostatic field which is responsible for the drift of the ionization electrons. Drift electrons are turn into electric signal when they reach the end-plates of the TPC, which are segmented into 18 trapezoidal sectors equipped with Multi-Wire Proportional Chambers (MWPC). The schematic view of the TPC detector is reported in Fig. 2.4.
Similarly to the ITS detector, the TPC is mainly devoted to tracking and PID. In particular, it allows to reconstruct over 90% of the tracks which pass through the detector, with a momentum resolution of 2% at $p_{\mathrm{T}} \simeq 10$ GeV/c in Pb–Pb collisions. As mentioned before, PID is performed via specific energy loss measurements with a resolution of about 5.5% and 7% in pp and in Pb–Pb collisions, respectively.

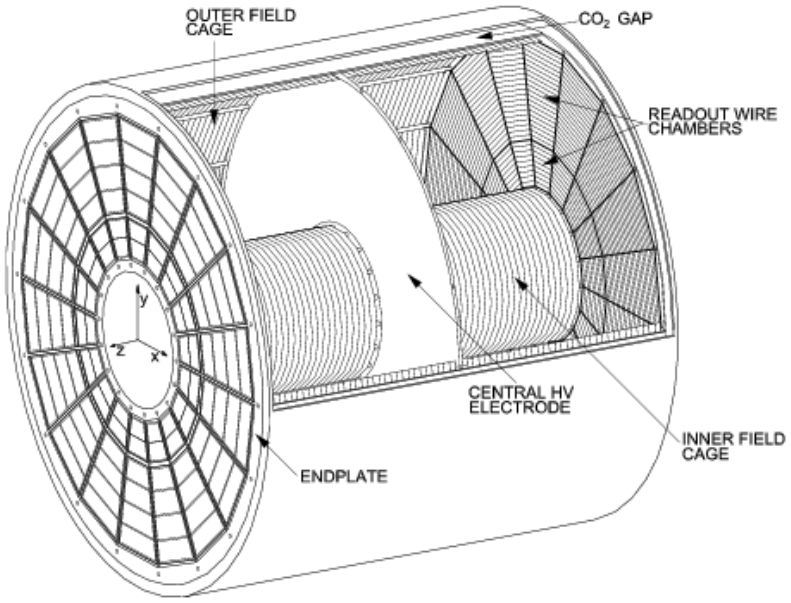

Fig. 2.4 The ALICE TPC structure. Figure from [76].

2.3.3 Time Of Flight (TOF)

The TOF detector [77] complements the TPC PID information in the intermediate momentum range $0.2 \sim 4$ GeV/c through the measurement of the time of flight of a particle from the interaction point to the TOF detector. As for the TPC detector, it is placed in the central barrel region with a pseudorapidity coverage $|\eta| < 0.9$. The TOF is a large array of Multi-gap Resistive Plate Chambers (MRPC) with a cylindrical shape. It is centered around the beam axis, with an internal radius of 370 cm, an external one of 399 cm and a total length of 7.45 m along the beam direction. Its thickness corresponds to 30% of X_0. The detector is filled by a mixture of 90% $C_2H_2F_4$, 5% C_4H_{10} and 5% SF_6 and it works in an avalanche regime, where the electrons generated by charged particles in the TOF gas are multiplied and collected thanks to the high electric field $E \approx 5$ kV/mm inside the MRPC.

2.3.4 TZERO (T0)

The T0 detector [78] is composed by two arrays of Cherenkov counters named T0A and T0C, which are placed in the backward and forward rapidity regions, respectively. The T0A is 375 cm far from the interaction point in the beam direction and it covers the pseudorapidity range $4.61 < \eta < 4.92$, while the T0C is -72.5 cm far from it and covers the range $-3.28 < \eta < -2.97$, both of them with a full azimuthal coverage.

The T0 detector can both provide the collision time t_0, which is exploited by the TOF detector, and the vertex position along the beam line, with a precision of 1.5 cm in the beam direction. Its time information is also used in the first level trigger (L0) to reject events at the data acquisition level, as described in Sec 2.4.

2.3.5 VZERO (V0)

The V0 detector [79] consists of two arrays of scintillator counters, the V0A and V0C. They are located 340 cm and 90 cm away from the interaction point, respectively, in the ATLAS and CMS directions. They cover the pseudorapidity range $2.8 < \eta < 5.1$ and $-3.7 < \eta < -1.7$, respectively, and they have full coverage over the azimuthal angle.
The V0 detector can measure the charged particle multiplicity at forward rapidity for pp collisions and is used to estimate the centrality of the collision for Pb–Pb events, where it also provides the minimum-bias and centrality triggers. Finally it is used for the rejection of background events such as beam-gas interactions, which feature a wrong time difference between the signals in V0A and V0C.

2.4 Trigger and Data Acquisition

The ALICE experiment relies on two separate triggers to acquire data, named Central Trigger Processor (CTP) [80] and High Level Trigger (HLT) [81]. The CTP is a low-level hardware trigger designed to provide several output signals built-up from different logical compositions of the inputs coming from different detectors. It is divided into three levels, characterized by different response times. The L0 trigger requires a decision ~ 1.2 μs after the collision based on the fast detectors, i.e. the V0, the SPD, the T0, the EMCal and the muon trigger. L1 trigger is applied ~ 6.5 μs after L0 and collects the output of the high-latency detectors which were not included in L0. Finally, ~ 88 μs after L0, L2 is performed to guarantee a past-future protection that reject other events in the time window around the collision under investigation. If L2 gives a trigger signal, then the Data AcQuisition (DAQ) is forced to start and the HLT to be processed. The HLT performs a fast online analysis to reconstruct tracks and primary vertices, allowing for the implementation of complex logics. As an example, the Minimum Bias (MB) and the centrality triggers, which will be discussed in the following, are defined at this stage. Once the DAQ process starts, dedicated farms of computers called Local Data Concentrators (LDCs) build subevents from the partial information received through optical connections, the Detector Data Links (DDLs). Global Data Collectors (GDCs) are

finally responsible for composing the full event thanks to the fast tracking and reconstruction information coming from the HLT. When the event building is complete, the data are buffered into a local disk pool and they are transferred to the CERN computing centre, where they are stored on tape.

2.5 ALICE offline framework

The ALICE experiment needs to properly handle the huge amount of data collected by the detectors in order to analyze the reconstructed events and make them available for the physics analyses. In terms of disk space ALICE collected between 50 and 70 Petabytes per year during Run2. Moreover, a large number of Monte Carlo (MC) simulations needs to be performed to determine the detection efficiency of the ALICE detector and to replicate its geometrical acceptance. The offline analysis framework, together with the Worldwide LHC Computing Grid (WLCG) [82], holds such a task. The WLCG is the infrastructure realized at CERN to provide global computing resources to store, distribute and analyze the data and MC samples which are used for the physics analyses.

2.5.1 Monte Carlo simulations

MC simulations are a fundamental part of the physics analyses of the ALICE experiment. The simulation process can be divided into three steps, which start with the event generation. The event generation is carried out by dedicated codes which mimic the production of all the stable and weakly decaying particles coming out of every collision. In this context, particles coming from strong decays are considered in the generation step, due to the extremely small time scale of strong interactions. Among the different event generators, HIJING [83] is usually used for Pb–Pb collisions and PYTHIA [84] for pp collisions. After the event generation, the propagation of particles through the experimental apparatus is simulated thanks to a dedicated code. In this step the kinematic parameters which where provided by the event generator are updated for each interaction of the particles moving through the detectors. Three transport codes are available: GEANT3 [85], GEANT4 [86] and FLUKA [87]. The ALICE geometry and material budget are precisely described in the aforementioned software, allowing for a precise simulation of the energy loss of particles in the detector material, of the generation of secondary particles from spallation processes and of the decay of unstable particles. In the final stage of the simulation, the impact point of a particle on the sensitive

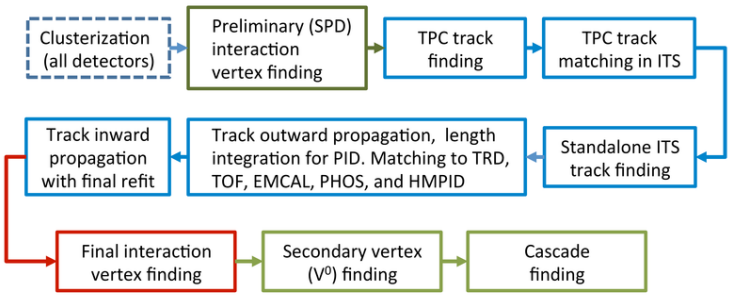

Fig. 2.5 Vertex and track reconstruction flow in ALICE.

area of a detector is stored as a hit. The detector response is also simulated and recorded in the same raw data format as for real data.

2.5.2 Event reconstruction

Starting from the raw data format used for both data and MC simulations, the events are fully reconstructed in a new format that can be used for physics analyses. The first step of the reconstruction, performed separately for each detector, consists in the conversion of the raw detector hits into clusters. Each cluster is defined by spatial position, signal amplitude and time, and also contains any additional information related to the specific detector, such as the measured energy loss or time of flight. The clusters from the SPD, which is the detector closest to the interaction point, are used to provide a first and fast estimation of the vertex position. The tracking process, described in details in Sec. 2.6.1, is initially carried out separately in each detector and then the information from each detector involved is combined to form global tracks. Finally, the vertex reconstruction takes place and relies on the fully reconstructed tracks. All the tracks are prolonged to the nominal beam line position and the point of closest approach between the tracks is chosen as the first estimate of the primary vertex. Specific physics processes, such as photon and strange hadron decays, are reconstructed only after primary vertex and full track reconstruction. The overall flow of the event reconstruction is schematically reported in Fig. 2.5.

2.5.3 Multiplicity and centrality determination

Reconstructed events can be classified depending on the number of charged particles produced in the collision. Among different possible strategies to estimate this quantity, also known as charged particle multiplicity, a forward-backward estimator is chosen in this work, in order to

avoid to estimate the multiplicity in the same region where the measurement of the analysis is performed. This choice is meant to exclude a possible bias, observed for light-flavor particles measured in pp collisions at $\sqrt{s} = 7$ TeV [34], which is introduced if both the measurement of particle production and the multiplicity estimation are carried out with the central barrel detectors. For this purpose, the information coming from the V0 detector can be exploited: the event multiplicity is evaluated from the V0 signal amplitude, which is proportional to the number of charged particles traversing the V0 scintillators. The multiplicity estimator is chosen as the sum of the signals of the V0A and V0C detectors and is labeled as V0M. From the integral of the normalized V0M signal, percentile classes are selected as shown in the left panel of Fig. 2.6 for pp collision at $\sqrt{s} = 13$ TeV [88]. Finally, a large number of collisions is simulated through a dedicated MC code and the response of the V0 detector is studied. In this way the correspondence between multiplicity and V0M signal is obtained and an average charged-particle multiplicity at mid-rapidity $\langle \frac{dN_{ch}}{d\eta_{lab}} \rangle$ is extracted and is associated to each multiplicity class.

This approach acquires a specific geometrical meaning in Pb–Pb collisions. In particular, a heavy-ion collision is characterized by the impact parameter b, which is the distance between the center of the two colliding nuclei in the plane transverse to the beam. Since this quantity can not be directly measured, a Glauber Model [89] is exploited to correlate the impact parameter to the charged particle multiplicity measured by the V0 detector. Thus for Pb–Pb collisions a new observable called centrality is defined as

$$c(b) = \frac{1}{\sigma_{AA}} \int_0^b \frac{d\sigma}{db'} db' \tag{2.3}$$

where σ_{AA} is a normalization factor defined as $\int_0^\infty \frac{d\sigma}{db'} db'$. By assuming that the impact parameter depends monotonically on the charged particle multiplicity and that the total cross section can be replaced by the number of observed events it is possible to express the centrality as

$$c(b) \approx \frac{1}{\sigma_{AA}} \int_d^{N_{ch}^\infty} \frac{dn}{dN'_{ch}} dN'_{ch} \, . \tag{2.4}$$

The distribution of the V0M signal is fitted with a function taken from a Monte Carlo Glauber model to connect this experimental quantity with the impact parameter of the collision as shown in the right panel of Fig. 2.6. As a remnant for the geometrical meaning of centrality, events from a class with a large V0M signal, thus a small impact parameter, are called central, while events with low V0M signal are defined as peripheral. As well as for multiplicity in pp collisions, the centrality distribution is divided into centrality classes and for each centrality class an average charged-particle multiplicity at mid-rapidity $\langle \frac{dN_{ch}}{d\eta_{lab}} \rangle$ is evaluated.

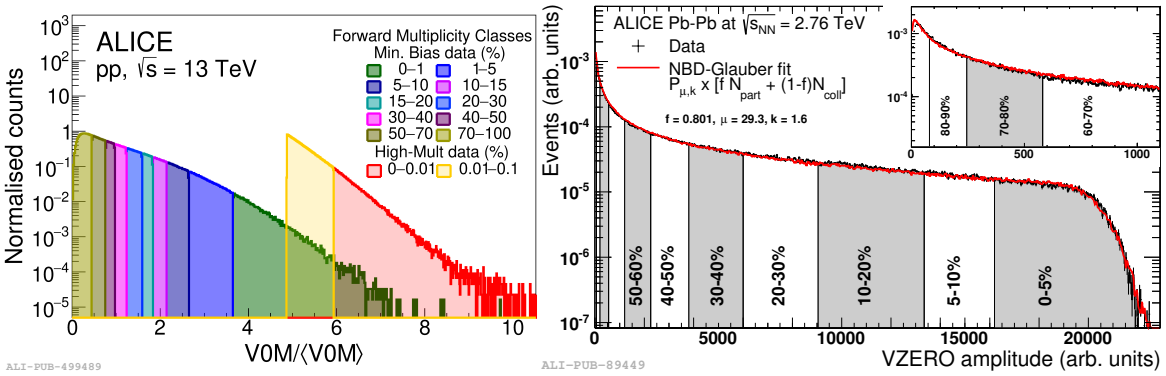

Fig. 2.6 Left: distribution of the V0M amplitude/⟨V0M amplitude⟩ for pp collisions at $\sqrt{s} =$ 13 TeV [88]. The sample is divided into percentile multiplicity classes. Right: distribution of the V0M amplitude in arbitrary units for Pb–Pb collisions at $\sqrt{s_{\mathrm{NN}}} = 2.76$ TeV [90], divided into centrality classes. The fit performed with a Glauber Model is also reported in red.

2.5.4 ALICE analysis framework

Collected and simulated data are accessible to the whole collaboration through the JAlien (Java ALICE Environment) [91] grid middleware software infrastructure. An optimized access pattern, called analysis train, allows the users to analyze different data samples at the same time limiting the usage of computing resources. This is a guarantee of reproducibility of the results, since it defines standard analysis flows which can be validated by each user. Both reconstructed and simulated data are stored in two formats. The first one is called Event Summary Data (ESD) and it is mainly used for calibration and detector performance studies. Thanks to the reduced amount of disk space needed, the Analysis Object Data (AOD) format is the preferred one for physics analyses. The main part of the ALICE offline software is the AliRoot [92] package, which is based on the ROOT [93] framework and it includes the analyses related code, which is called AliPhysics.

2.6 ALICE performance

The ALICE detector was specifically designed to cope with the very demanding experimental environment created in the hadronic collisions provided by the LHC. In order to perform physics analyses in this challenging conditions, excellent PID performances are needed, together with precise vertex and track reconstruction capabilities. The performance achieved by the ALICE detectors during the data taking are described in the following.

2.6.1 Tracking

Tracking is a complex procedure which requires in parallel different information from many detectors of the central barrel. The process starts building track seeds moving from the outer region of the TPC inwards, by subsequently attaching inner TPC clusters to the track. Whenever a compatible cluster is found, a dedicated algorithm based on a Kalman filter [94] is responsible for updating the track parameters. Shared clusters between multiple tracks are permitted, but a predefined threshold is usually set between 25% and 50%: if in a track the fraction of shared clusters is above the threshold, the candidate tracks with the worst quality parameters are rejected by a dedicated algorithm. In order to improve the quality of the TPC track reconstruction, tracks with less than 20 clusters out of a maximum of 159 or that miss more than 50% of the expected clusters are also rejected. The tracking reconstruction efficiency of the TPC detector is shown as a function of the track momentum for pp collisions at $\sqrt{s} = 8$ TeV and for two different centrality classes in Pb–Pb collisions at $\sqrt{s_{\mathrm{NN}}} = 2.76$ TeV in Fig. 2.7. The reconstruction process moves then to the ITS, with a procedure which is the same as described for the TPC detector: the TPC tracks are prolonged to the second layer of the SSD and progressively inwards to match ITS clusters. Tracks with a smaller amount of compatible clusters are penalized in the reconstruction. If both the TPC and ITS reconstruction are successful, the ITS+TPC track is then propagated outwards to match the other central barrel detectors. The algorithm starts building TRD tracklets, which are segments connecting two clusters belonging to two consecutive layers, and searches for matches between ITS+TPC tracks and TRD tracklets. Then the track is extrapolated to match one of the TOF clusters and to get additional information about the track from the HMPID, PHOS and EMCal detectors. Finally the track is refitted from the TRD back to the innermost ITS layer to get its global parameters and a specific refit flag is switched on if the procedure ends successfully. The track reconstruction process is schematically described in Fig. 2.8.
The complete tracking process provides a very precise measurement of position, direction, inverse curvature and covariance matrix of the track, which are needed for the particle momentum measurement and the vertex determination. The momentum of a charged particle traveling in a magnetic field B can be calculated as

$$p = \frac{L^2 qB}{8s} \tag{2.5}$$

where L is the lever arm length of the tracking detectors, q is the charge of the particle and s is the sagitta of the track, which is provided by the position sensitive detectors located in the

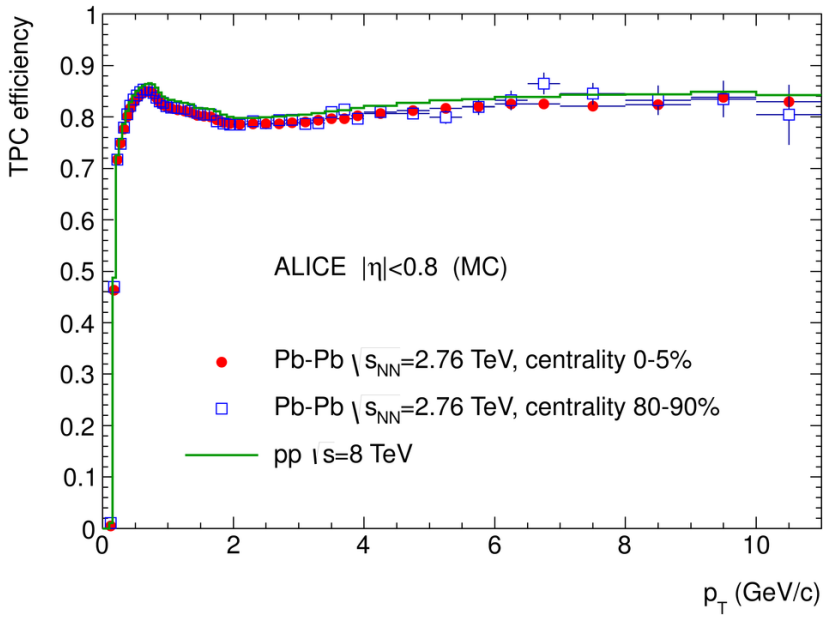

Fig. 2.7 TPC track reconstruction efficiency for pp (green line) collisions at $\sqrt{s} = 8$ TeV and for different centralities (red dots and blue open squares) in Pb–Pb collisions at $\sqrt{s_{\mathrm{NN}}} = 2.76$ TeV. The tracking efficiency appears not to depend on the event multiplicity. Figure from [95].

space surrounding the interaction point. This quantity can be evaluated with a resolution

$$\frac{\sigma_{\mathrm{p}}}{p} \propto p \frac{\sigma_{\mathrm{s}}}{BL^2} \tag{2.6}$$

which depends on the resolution over the track sagitta σ_s. The large radial coverage of the ALICE experiment allows for a precise measurement of particle momentum over a wide momentum range. The resolution on the quantity $1/p_{\mathrm{T}}$ is reported in Fig. 2.9 for p–Pb collisions at $\sqrt{s_{\mathrm{NN}}} = 5.02$ TeV for tracks obtained at different steps of the tracking procedure.

2.6.2 Vertexing

The capability to reconstruct vertices with an excellent precision is another relevant feature of the ALICE experiment. The vertexing process is meant to reconstruct both the primary vertex, i.e. the collision point, and secondary vertices coming from the weak decays of particles, and to separate them efficiently.

Primary vertex The primary vertex evaluation starts with a very fast vertex estimation provided by the SPD layers of the ITS in the event reconstruction process, as described in Sec. 2.5.2. The algorithm builds SPD tracklets from the SPD clusters in a fixed azimuthal

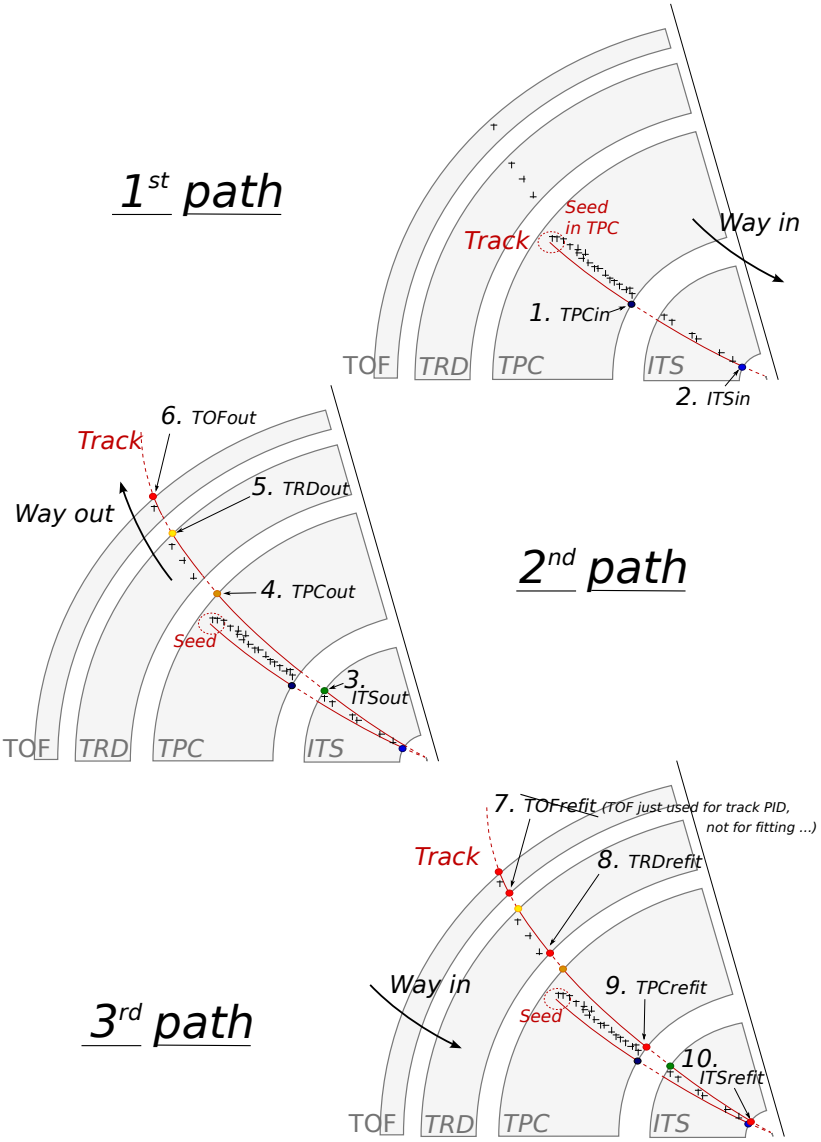

Fig. 2.8 Schematic view of the tracking of an event, divided into three subsequent steps. Figure from [95].

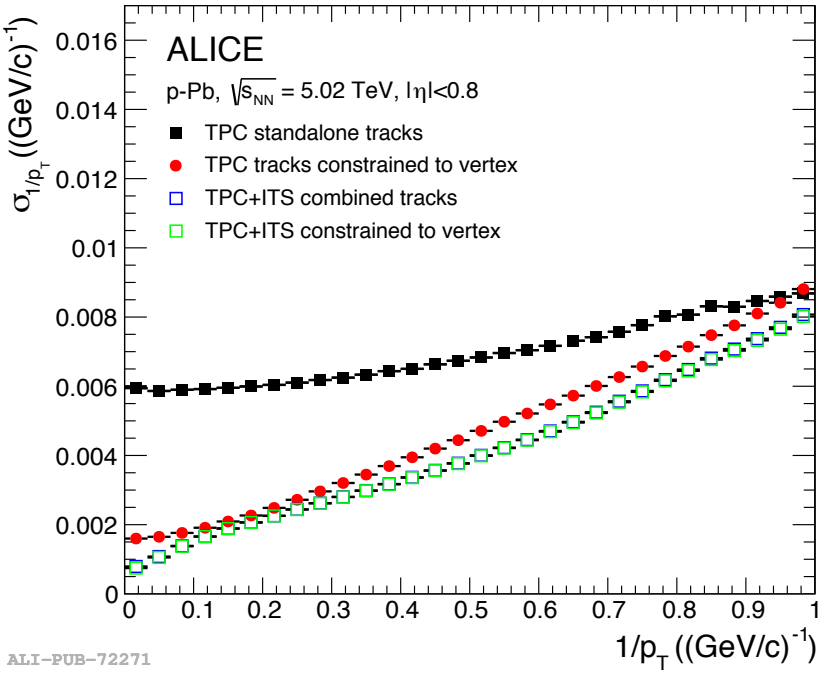

Fig. 2.9 Resolution on the $1/p_{\mathrm{T}}$ quantity as a function of $1/p_{\mathrm{T}}$ in p–Pb collisions at $\sqrt{s_{\mathrm{NN}}} = 5.02$ TeV for tracks reconstructed at different steps of the tracking process with different colors. No significant difference is observed when ITS+TPC tracks (blue markers) are matched to the primary vertex (green markers). The choice of the $1/p_{\mathrm{T}}$ quantity depends on the fact that it can be directly extracted from the covariance matrix of the Kalman filter fit. Figure from [95].

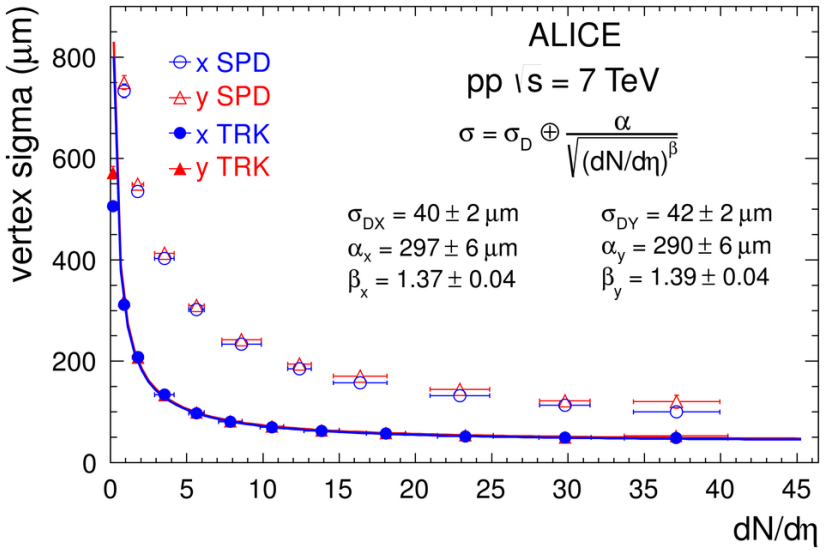

Fig. 2.10 Resolution on the primary vertex position using the SPD clusters only (open markers) and the full track information (full markers) as a function of the charged particle multiplicity in pp collisions at $\sqrt{s} = 7$ TeV. The red points correspond to the y coordinate while the blue ones to the x coordinate.

angle window and extrapolate the tracklets to the nominal interaction point. If at least two tracklets are present, the primary vertex is evaluated as the point which minimizes the distance from all of them. This rough estimate is superseded by the vertex estimation which is performed at the end of the tracking process: when full tracks have been reconstructed, they are propagated to the nominal beam line and the vertex position is evaluated again by excluding tracks too far from it. The results coming from the two approaches are reported in Fig. 2.10 as a function of charged particle multiplicity. Higher multiplicity events grant a better resolution in terms of primary vertex estimation, reaching a precision of the order of $\sim 50\ \mu$m.

Secondary vertex The search for additional vertices coming from the decay of unstable particles takes place once the primary vertex position has been estimated. A dedicated algorithm, called weak decay finder, is implemented in the ALICE software and is responsible to search for the weak decays of both charged and neutral particles. The process starts from the latter: pairs of tracks with opposite sign and close in the phase space are matched and backward reconstructed to form a neutral mother particle (V0) which decays in the minimum distance point between the daughter tracks. Among the huge number of two-particle combinations, the pairs must fulfill some quality criteria in order to be stored as V0 candidates. The Distance of Closest Approach (DCA), which is the minimum distance

between the prolonged charged tracks, must be small enough, as well as the minimum distance between the tracks and the estimated secondary vertex. The cosine of the pointing angle ($\cos(\theta_{\mathrm{p}})$), where θ_{p} is the angle between the total momentum vector of the daughter pair and the straight line connecting the primary and secondary vertices, is required to be large. After the reconstruction of V0s, such as $\mathrm{K}^0_{\mathrm{S}}$ mesons and Λ baryons, an additional iteration of the weak decay finder combines V0s and charged tracks to reconstruct the weak decays of charged particles. As well as for the reconstruction of the V0 vertex, selection criteria on the DCA between the V0 and the charged particle, and on cosine of pointing angle are applied to reduce the combinatorial background. Finally, the secondary vertex position is estimated as halfway between the point of closest approach of the V0 and the point of closest approach of the charged track. Two operating modes are available for the weak decay finder algorithm. The offline finder is executed after the full track reconstruction, while the on-the-fly one is already used during the track fitting procedure. In this work, the offline finder will be used to reconstruct the decays of the Ξ and Ω baryons, whose analysis will be described in details in Chapter 5.

2.6.3 Particle Identification

A key feature of the ALICE experiment is the excellent particle identification capability of the detectors, characterized by high resolution over a wide momentum range. The PID is mainly carried out by the ITS, TPC, TOF and HMPID detectors, and is based on different physical principles depending on the detector technology. The ITS and the TPC identify charged particles via specific energy loss measurements, the TOF detector measures the time of flight and the HMPID evaluates the relativistic $\beta = v/c$ measuring the Cerenkov light angle. In each physics analysis the particle identification is performed by combining the information of a subset of PID detectors, depending on the analysis requirements. This is done in order to achieve the desired purity without drastically reducing the detection efficiency. In the following, the PID detectors used for this work will be described.

TPC The TPC detector performs particle identification through specific energy loss measurements in the detector gas. The 159 padrows located in the end-plates collect the free charges drifting through the detector which have been produced via ionization by the charged particles traversing the detector. The particle energy loss depends on the collected electric charge with some contributions given by the value of the electric field and by gain factors, which are known parameters for each data taking period. The final $\frac{\mathrm{d}E}{\mathrm{d}x}$ is evaluated as the truncated mean of each single padrow measurement. If the particle momentum is known, the

specific energy loss is evaluated as

$$f(\beta\gamma) = \frac{P_1}{\beta^{P_4}} \left\{ P_2 - \beta^{P_4} - \ln\left[P_3 + \frac{1}{(\beta\gamma)^{P_5}} \right] \right\} . \tag{2.7}$$

This parameterization, which is provided by the ALEPH collaboration [96], relies on the particle velocity β and on the Lorentz factor γ, while P_i are parameters fixed by a fit to experimental data. An additional parameterization is provided by the ALICE analysis framework through splines which allow to calculate the energy loss as a function of the rigidity p/z for particles with electric charge z. The specific energy loss obtained through splines is reported in Fig. 2.11 for p–Pb collisions at $\sqrt{s_\mathrm{NN}} = 5.02$ TeV.
Relying on $\frac{\mathrm{d}E}{\mathrm{d}x}$ measurements, a precise identification of the particle species is possible for low momentum tracks, where the specific energy loss varies significantly for different particle types. On the contrary, for higher momenta, particles reach the Minimum Ionizing Particle region and cannot be distinguished on a $\frac{\mathrm{d}E}{\mathrm{d}x}$ measurement basis, since the expected $\frac{\mathrm{d}E}{\mathrm{d}x}$ values are similar for all species. The $\frac{\mathrm{d}E}{\mathrm{d}x}$ resolution of the ALICE TPC is about 5.5% in pp collisions and 7% in Pb–Pb collisions. The identification is commonly performed evaluating the difference between the measured $\frac{\mathrm{d}E}{\mathrm{d}x}$ and the expected one for a certain particle species. The $n\sigma$ value is calculated as

$$n\sigma = \frac{\frac{\mathrm{d}E}{\mathrm{d}x}_\mathrm{meas} - \frac{\mathrm{d}E}{\mathrm{d}x}^\mathrm{i}_\mathrm{exp}}{\sigma^\mathrm{i}_\mathrm{exp}} \tag{2.8}$$

where $\sigma^\mathrm{i}_\mathrm{exp}$ is the expected detector $\frac{\mathrm{d}E}{\mathrm{d}x}$ resolution for the species i obtained with a Gaussian fit to the $\frac{\mathrm{d}E}{\mathrm{d}x}$ distribution in different momentum intervals. $\frac{\mathrm{d}E}{\mathrm{d}x}_\mathrm{meas}$ is the measured signal for the candidate track and $\frac{\mathrm{d}E}{\mathrm{d}x}^\mathrm{i}_\mathrm{exp}$ is the expected signal for the same species i, obtained from the ALEPH parameterization or the ALICE splines.

TOF The time measurement provided by the TOF detector can be exploited for particle identification purposes. If a TOF cluster is attached to a track during the tracking process, the velocity β of the particle is evaluated as

$$\beta c = \frac{\Delta t_\mathrm{meas}}{L} \tag{2.9}$$

where $\Delta t_\mathrm{meas} = t_\mathrm{TOF} - t_0$ is the time of flight of the particle and L is the integrated track length. The collision time t_0 is provided by the T0 detector as described in Sec. 2.3.4, while t_TOF is the time measured by the TOF detector. The measured β value for tracks with an attached TOF cluster is reported as a function of the transverse momentum in Fig. 2.12 for pp collisions at 5.02 TeV.

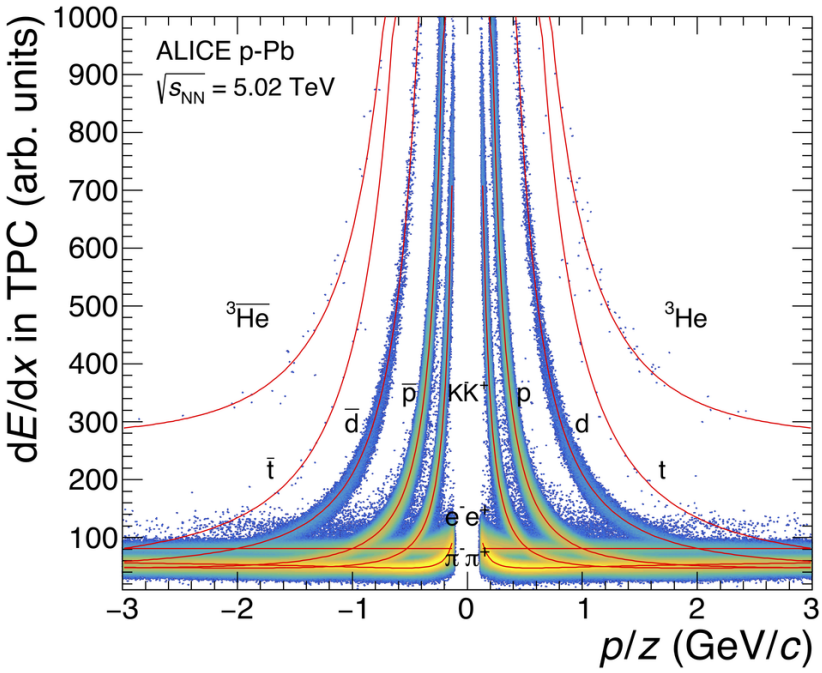

Fig. 2.11 TPC specific energy loss as a function of the rigidity p/z for charged particles and antiparticles in p-–Pb collisions at $\sqrt{s_{\mathrm{NN}}} = 5.02$ TeV. The red lines represent the expected detector response for different particle species. Figure taken from the ALICE figure repository ©.

As well as for the TPC detector, the particle identification can be performed by using the $n\sigma$ method through the formula

$$n\sigma = \frac{\Delta t_{\mathrm{meas}} - \Delta t^{\mathrm{i}}_{\mathrm{exp}}}{\sigma^{i}_{\mathrm{exp}}} \tag{2.10}$$

where Δt_{meas} is the time of flight of the measured track, $\Delta t^{\mathrm{i}}_{\mathrm{exp}}$ is the expected time of flight for the particle species i and $\sigma^{i}_{\mathrm{exp}}$ is the expected resolution on Δt_{meas} for the species i. Another possible strategy is the evaluation of the particle mass, starting from the TOF time measurement, which can be calculated as

$$m^2_{\mathrm{TOF}} = \frac{p^2}{c^2}\left(\frac{c^2 \Delta t^2_{\mathrm{meas}}}{L^2} - 1\right) \tag{2.11}$$

where p is the momentum of the particle and L is the integrated length of the track. Both methods can be applied to perform particle identification in an intermediate to high momentum region, which is typically not reachable with a TPC measurement, extending the physics analyses towards higher momenta.

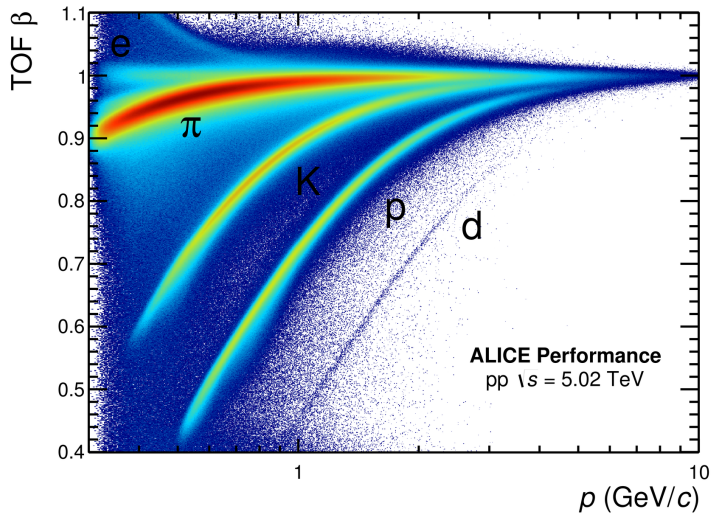

Fig. 2.12 Velocity of the particles in pp collisions at $\sqrt{s} = 5.02$ TeV computed using the time of flight information from the TOF detector as a function of the measured track momentum. The mismatch background, due to tracks incorrectly matched to TOF clusters, is well visible. Figure taken from the ALICE figure repository ©.

Chapter 3

Light nuclei and strangeness production in high energy physics

The goal of probing and characterizing the QGP is pursued by the ALICE experiment by studying many different and complementary observables. The production of light nuclei in small colliding systems and strange hadrons in Pb–Pb collisions are two outstanding examples of the large variety of measurements which can be carried out to explore the physical processes underlying high energy hadronic collisions, ranging from small to large colliding systems. In the following, those observables will be described together with the theoretical models available up to date to describe the production mechanism of light nuclei and strange particles in high energy physics.

3.1 Light flavor particle production from small to large colliding systems

As was mentioned in Sec. 1.4.1, light nuclei and strange particles can be classified as soft probes, being produced during the hadronization phase, shortly after the chemical freeze-out. In this context, the understanding of the mechanism which governs light flavor particle production is a key information to describe properly the latest stages of the evolution of an hadronic collision. The production of light nuclei is theoretically described using two phenomenological models: the coalescence model [97] and the Statistical Hadronization Model (SHM) [98]. The coalescence model assumes that light nuclei, being composite objects formed by more than one nucleon, can be produced via a coalescence process. The SHM

describes the mechanism responsible for the production of various particle species by using a thermal-driven approach for different collision systems at the LHC energies. In particular, it is suitable to describe both the production of light nuclei and strange particles. On the other hand, the production of strange particles is also explained by either hydrodynamic [99] and microscopic [100, 101] models or general purpose event generators [102]. The former aim to describe the fireball expansion and the subsequent system evolution through the principles of hydrodynamics and via the microscopic interactions between the medium constituents, while the latter are built to describe the hadronic collision as a whole, starting from the very short distance scales of quark-quark interactions, up to the typical scale of hadron formation and decay. A detailed discussion of these models will be given in the following, while the comparison between the model predictions and the experimental results from this work will be discussed in Chapter 4 and Chapter 5 for light nuclei and strange particles, respectively.

3.1.1 Coalescence model

The formation of light nuclei might be explained via the coalescence mechanism: the fundamental assumption of the so called coalescence model is that nucleons which are close enough in phase space at the kinetic freeze-out can bind together to form a nucleus. In this static model, whose first implementation was developed for explaining nuclei production in proton-nucleus collisions [103], there is no attempt to give a detailed description of the interactions that lead to the formation of nuclei. Starting from the invariant momentum distribution of the constituents nucleons $E_{\mathrm{p}}(\mathrm{d}^3N_{\mathrm{p}}/\mathrm{d}p_{\mathrm{p}}^3)$, the coalescence model predicts the momentum spectra of light nuclei $E_{\mathrm{i}}(\mathrm{d}^3N_{\mathrm{i}}/\mathrm{d}p_{\mathrm{i}}^3)$. The key parameter of this model is usually known as coalescence parameter B_{A} and it is proportional to the probability to form a certain nucleus starting from A protons and neutrons. The invariant momentum distribution of the produced nuclei can be evaluated from the model as

$$E_{\mathrm{i}}\frac{\mathrm{d}^3N_{\mathrm{i}}}{\mathrm{d}p_{\mathrm{i}}^3} = B_{\mathrm{A}}\left(E_{\mathrm{p}}\frac{\mathrm{d}^3N_{\mathrm{p}}}{\mathrm{d}p_{\mathrm{p}}^3}\right)^A \tag{3.1}$$

where A is the mass number of the nucleus i under investigation, while E_{i} and E_{p} are the energies of the nucleus and of the constituent nucleons, respectively. Equation 3.1 is obtained under the assumption of proton-neutron isospin symmetry, since it is not possible for the ALICE experiment to measure neutral particles such as neutrons, due to the absence of a hadronic calorimeter. This is however a reasonable assumption, due to the expected vanishing baryo-chemical potential at the LHC energies.

A very simple implementation of the coalescence model, thus called naive coalescence [97], takes into account only the nucleon momentum correlations, without considering any dependence on the spacial coordinates. Nucleons are required to have similar momenta in order to meet the conditions for coalescence to happen, but no constraints on their position within the fireball is set. With this approximation, the coalescence parameter can be written as

$$B_{\mathrm{A}} = \left(\frac{4}{3}\pi p_0^3\right)^{A-1} \frac{m_{\mathrm{A}}}{m_{\mathrm{p}}^A} \tag{3.2}$$

where m_{A} and m_{p} are the nucleus and proton masses, respectively. The only free parameter is the p_0 value, which is the maximum radius in the momentum space for which a coalescence process is allowed. No dependence of B_{A} on multiplicity, thus on the system size, nor on transverse momentum is expected. This simplified approach is reasonable in small colliding systems, such as pp collisions, since the system size ($r \approx 1$ fm [104]) is similar or even smaller than the nucleus radius ($R \approx 2$ fm [105–107]) and nucleons are close in space.
However, when a larger system such as a Pb–Pb collision ($r \approx 6$ fm in central Pb–Pb collisions [108, 109]) is inspected, two nucleons can be produced far from each other but with similar momenta: in this case, the naive implementation would allow a coalescence process to happen, even though in principle the nucleons are well separate in space, thus a coalescence process could not happen. For this reason a more advanced implementation is required to describe the trend of the experimental data across different collision systems. A Wigner formalism can be used to describe the quantum-mechanical nature of the coalescence process and in this advanced approach [110] the starting point is the definition of a nucleus wave-function as

$$\psi_{\mathrm{A}}(\vec{r}) = \left(\pi R_{\mathrm{A}}^2\right)^{-\frac{3}{4}} e^{-\frac{r^2}{2R_{\mathrm{A}}^2}} \tag{3.3}$$

where the nucleus is approximated as a harmonic-oscillator characterized by a radius R_{A}. The complete space-time dependence is taken into account with an average correction factor which enters the calculation and has the form

$$\langle C_{\mathrm{A}} \rangle = \prod_{\mathrm{i}=1}^{\mathrm{A}} \left(1 + \frac{R^2}{4R_{\mathrm{i}}^2}\right)^{-\frac{1}{2}(A-1)} \tag{3.4}$$

where R is the size of the emitting source created in the collision. The behavior of the $\langle C_{\mathrm{A}} \rangle$ correction factor as a function of R is reported in the upper panel of Fig. 3.1 for different assumption on the value of the deuteron radius. $\langle C_{\mathrm{A}} \rangle$ is identically null for a point-like source ($R \to 0$) and it increases smoothly with increasing R, saturating to unity for large source size values. Thanks to this approach, the model provides an analytical expression for

the coalescence parameter which derives from quantum mechanical principles and can give predictions across different colliding systems with a continuous behavior, depending only on the interplay between the sizes of the system and of the nucleus. The B_{A} parameter is evaluated as

$$B_{\mathrm{A}}(R) = \frac{g_{\mathrm{A}}}{2^A}\frac{1}{\sqrt{A}}\frac{1}{m_{\mathrm{T}}^{A-1}}\left[\frac{2\pi}{R^2+\left(\frac{R_{\mathrm{A}}}{2}\right)^2}\right]^{\frac{3}{2}(A-1)} \tag{3.5}$$

where g_{A} is the spin degeneracy factor of the nucleus and $m_{\mathrm{T}} = \sqrt{m^2+p_{\mathrm{T}}^2}$ is its transverse mass. As an example, the coalescence parameter of deuterons B_2 is reported in the lower panel of Fig. 3.1 as a function of the system radius. The interplay between the system and nucleus sizes drives the behavior of the coalescence parameter in this approach: for small sources such as pp collisions, R is negligible and the coalescence parameter does not depend on it, retrieving the naive coalescence implementation. On the contrary, for large systems the inverse proportionality on R is the dominant factor, leading to a decrease in the coalescence parameter as a function of the system radius.

Another similar implementation [111] exploits again the Wigner formalism in order to compute production yields of light nuclei produced via coalescence. The phase-space distribution of the fireball is described as a thermalized expanding spherical distribution with a kinetic freeze-out temperature T_{k} and radius R via the formula

$$f_{\mathrm{p,n}}(x,k) = \frac{N_{\mathrm{p,n}}}{(2\pi)^3\left(m_{\mathrm{A}}T_{\mathrm{k}}R_{\mathrm{p,n}}^2\right)^{\frac{3}{2}}}e^{-\frac{k^2}{2m_{\mathrm{A}}T_{\mathrm{k}}}-\frac{x^2}{R^2}} \tag{3.6}$$

where m_{A} is the nucleus mass and $N_{\mathrm{p,n}}$ is the number of neutrons or protons within the fireball. The full calculation allows for the evaluation of the total number of produced nuclei. As an example, the number of deuterons is obtained as

$$N_{\mathrm{d}}(R) = \frac{3N_{\mathrm{p}}N_{\mathrm{n}}}{4\left(m_{\mathrm{d}}T_{\mathrm{k}}R^2\right)^{\frac{3}{2}}}\frac{1}{\left(1+\frac{1}{m_{\mathrm{d}}T_{\mathrm{k}}R_{\mathrm{d}}^2}\right)^{\frac{3}{2}}}\frac{1}{\left(1+\frac{R_{\mathrm{d}}^2}{4R^2}\right)^{\frac{3}{2}}} \tag{3.7}$$

where R_{d} is the size parameter of the deuteron. Keeping in mind that typically $T_{\mathrm{k}} \approx 100$ MeV, thus $m_{\mathrm{A}}T_{\mathrm{k}} \gg 1/R_{\mathrm{d}}^2$, and dividing by the total number of produced protons, it is possible to obtain predictions on the yield ratios between the produced nuclei and protons. For deuterons

the ratio is expressed as

$$\frac{N_{\mathrm{d}}}{N_{\mathrm{p}}}(R) = \frac{3N_{\mathrm{n}}}{4\left(m_{\mathrm{d}}T_{\mathrm{k}}R^2\right)^{\frac{3}{2}}} \frac{1}{\left[1+\left(\frac{1.6\ \mathrm{fm}}{R}\right)^2\right]^{\frac{3}{2}}} \tag{3.8}$$

while for helions it is evaluated as

$$\frac{N_{^3\mathrm{He}}}{N_{\mathrm{p}}}(R) = \frac{N_{\mathrm{n}}N_{\mathrm{p}}}{4\left(m_{^3\mathrm{He}}T_{\mathrm{k}}R^2\right)^3} \frac{1}{\left(1+\frac{R^2_{^3\mathrm{He}}}{2R^2}\right)^3}\ . \tag{3.9}$$

The last factor of both Eq. 3.8 and Eq. 3.9 describes the interplay between the nucleus size and the emitting source size. In particular, when R is of the order of the nucleus size, this factor is responsible for the decrease of the nuclei to proton ratios with respect to the saturation value, expected from the model for large system size.
Thus the coalescence models are able to predict a smooth evolution of two key observables, the coalescence parameter B_{A} and the nuclei-to-proton ratios, as a function of the system size, going from small systems such as pp collisions to large collision systems, namely Pb–Pb collisions at the LHC. These predictions will be compared to the experimental results from this work in Sec. 4.10 and in Sec. 4.11.

3.1.2 Statistical hadronization model

The statistical hadronization model (SHM) [98], also known as thermal-model, relies on the principles of statistical mechanics. Thanks to the very large number of particles produced in the hadronic collision, SHM assumes that, at the chemical freeze-out, the fireball has reached thermal and chemical equilibrium. The system is treated as a gas of ideal non-interacting hadrons and resonances, including all the known contributions up to a temperature of 190 MeV. Within this approach, the fireball can be described with a partition function and by using statistical mechanics. Two different versions of the SHM are devoted to explain particle production in small and large colliding systems and they depend on the conservation laws that are applied in the calculations. They are based on either a canonical or a grand canonical ensemble.

Grand canonical ensamble In large colliding systems a grand canonical (GC) ensemble is used. With this approach, the conservation laws for energy and quantum numbers are

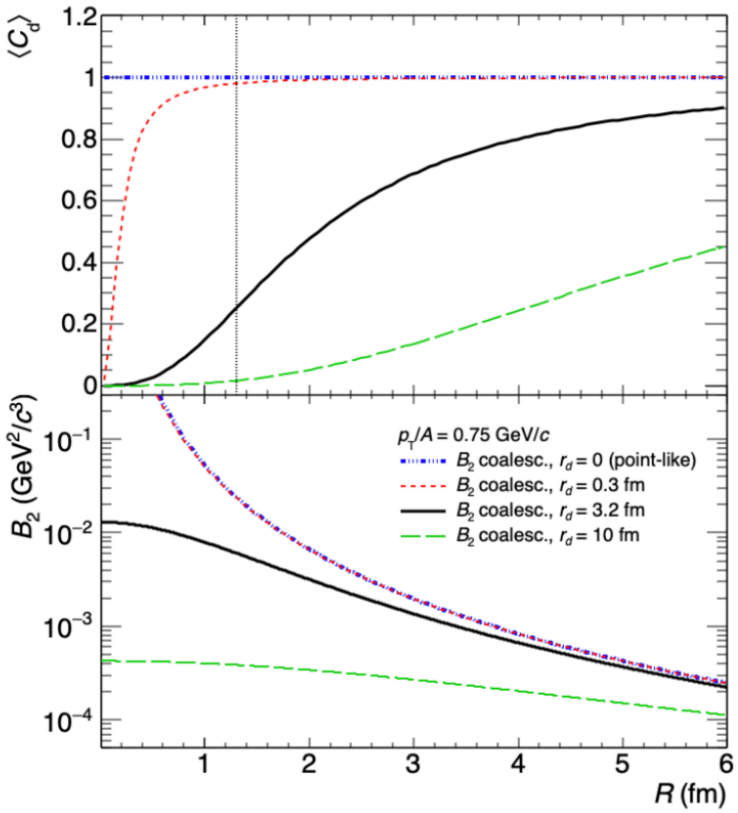

Fig. 3.1 Quantum-mechanical correction factor $\langle C_{\mathrm{A}} \rangle$ (top) and coalescence parameter B_2 (bottom) as a function of the radius R of the emitting source. The predictions obtained by assuming different deuteron radius R_{d} values are reported with different colors. Figure taken from [110]

fulfilled on average over the system. The fireball is described via its partition function Z as

$$Z(T,V,\mu) = \prod_{\mathrm{j}} Z_{\mathrm{j}}(T,V,\mu_{\mathrm{j}}) \tag{3.10}$$

where T, V and μ are the variables characterizing the system, namely its temperature, volume and chemical potential. For the specie j, the single partition function can be written through its logarithm as

$$\ln Z_{\mathrm{j}}(T,V,\mu_{\mathrm{j}}) = \frac{V g_{\mathrm{j}}}{2\pi^2} \int_0^{\infty} \pm p^2 \mathrm{d}p \ln\left(1 \pm e^{-\frac{E_{\mathrm{j}}-\mu_{\mathrm{j}}}{T}}\right) \tag{3.11}$$

where $g_{\mathrm{j}} = 2s+1$ is the spin degeneracy factor and $E_{\mathrm{j}} = \sqrt{p^2+m_{\mathrm{j}}^2}$ is the total energy. The $+$ and $-$ signs are for fermions, according to the Fermi-Dirac statistics, and for bosons, according to Bose-Einstein statistics, respectively. The chemical potential for the single species is defined as the sum of the globally conserved quantum numbers. Since the SHM includes contributions up to 190 MeV, the only quark species available are u, d and s, limiting the quantum numbers to be conserved to three: charge Q, strangeness number S and baryon number B. Thus the chemical potential for each species j can be expressed as

$$\mu_{\mathrm{j}} = Q_{\mathrm{j}}\mu_{\mathrm{Q_j}} + S_{\mathrm{j}}\mu_{\mathrm{S_j}} + B_{\mathrm{j}}\mu_{\mathrm{B_j}} \tag{3.12}$$

The initial state of the collision gives anyway constraints on the three quantum numbers to be conserved. The strangeness content of the colliding nuclei is null, fixing $\mu_{\mathrm{S}} = 0$. Moreover the μ_{Q} value is fixed by the net charge of the colliding particles. Thus the only truly free component of the chemical potential is due to the baryo-chemical potential μ_{B}, which depends on the energy of the collision. Starting from the partition function and keeping in mind these constraints, it is possible to evaluate the average number of produced particles for the species j as

$$\langle N_{\mathrm{j}}^{(\mathrm{gce})} \rangle (T,V,\mu_{\mathrm{B_j}}) = (1 + \sum_{\mathrm{i}} \Gamma_{\mathrm{i}\to\mathrm{j}}) \frac{VTg_{\mathrm{j}}}{2\pi^2} \sum_{\mathrm{k}=1}^{\infty} \frac{(\pm 1)^{\mathrm{k}+1}}{k^2} e^{\frac{k}{T}\left(Q\mu_{\mathrm{Q}} + B_{\mathrm{j}}\mu_{\mathrm{B_j}}\right)} m_{\mathrm{j}}^2 K_2\left(\frac{k m_{\mathrm{j}}}{T}\right) \tag{3.13}$$

where the first term of the equation accounts for the decay of any possible hadronic resonance i into the species j via its branching ratio $\Gamma_{\mathrm{i}\to\mathrm{j}}$, resulting in an increase with respect to a thermal-only production. The second term describes the thermal production of the species j with a mass m. K_2 is a modified Bessel function of the second kind. The grand canonical approach to SHM grant predictions for a large variety of particle species in Pb–Pb collisions: for what concerns this work, predictions for the production of both strange particles and light nuclei arise naturally when the chemical freeze-out temperature and the baryo-chemical

potential are set to $T = 156$ MeV and $\mu_B = 0.7$ MeV, the specific values constrained by the LHC running conditions [112].

Canonical ensamble In small colliding systems a canonical description of the fireball is used, giving rise to the Canonical Statistical Model (CSM). In pp collisions, where the spacial extension of the fireball is small, the hadron resonance gas is required to undergo local conservation of quantum charges. Thus an exact conservation of Q, S and B is demanded over the whole correlation volume V_c. At given temperature and correlation volume, the partition function is defined as

$$Z(Q,S,B) = \int_{-\pi}^{\pi} \frac{d\phi_Q}{2\pi} \int_{-\pi}^{\pi} \frac{d\phi_S}{2\pi} \int_{-\pi}^{\pi} \frac{d\phi_B}{2\pi} e^{-i\left(Q\phi_Q + S\phi_S + B\phi_B\right)} \times e^{\sum_j Z_j e^{i\left(Q_j\phi_Q + S_j\phi_S + B_j\phi_B\right)}} \tag{3.14}$$

where j runs over all the species included in the gas. Q_j, S_j and B_j are the quantum charges associated to each species. Z_j is the single partition function for the specie j and it is expressed as

$$Z_j = \frac{V_c g_j}{2\pi^2} \int dm \rho_j(m) m^2 T K_2\left(\frac{m}{T}\right) \tag{3.15}$$

where g_j and $\rho_j(m)$ are the degeneracy factor and the mass distribution of the species j, respectively. K_2 is again the modified Bessel function of the second kind. As well as before, the average number of produced particles for the species j is evaluated starting from the partition function as

$$\langle N_j^{(ce)} \rangle = (1 + \sum_i \Gamma_{i\to j}) \frac{Z(Q - Q_j, S - S_j, B - B_j)}{Z(Q,S,B)} \langle N_j^{(gce)} \rangle \tag{3.16}$$

where $\langle N_j^{(gce)} \rangle$ is the result obtained for the specie j in a GC ensemble. Similarly to the grand canonical ensemble result, the first term of the equation accounts for the feed-down contribution from hadronic resonance decays. The second factor acts on the grand canonical production reducing the expected yields due to the local conservation of the Q, S and B charges.

As an overall effect, the CSM expected yields are suppressed with respect to a GC description. This effect, known as canonical suppression, can be observed in Fig. 3.2, where the ratio between the predictions obtained with a SHM implementing a GC and a canonical ensemble is reported as a function of the correlation volume. For particles with varying strangeness content, ranging from π mesons to Ω baryons, this ratio is reported with different colors depending on the quantum numbers conserved in the calculations. As described previously, the CSM implements the local conservation of B, S and Q simultaneously, thus it is represented

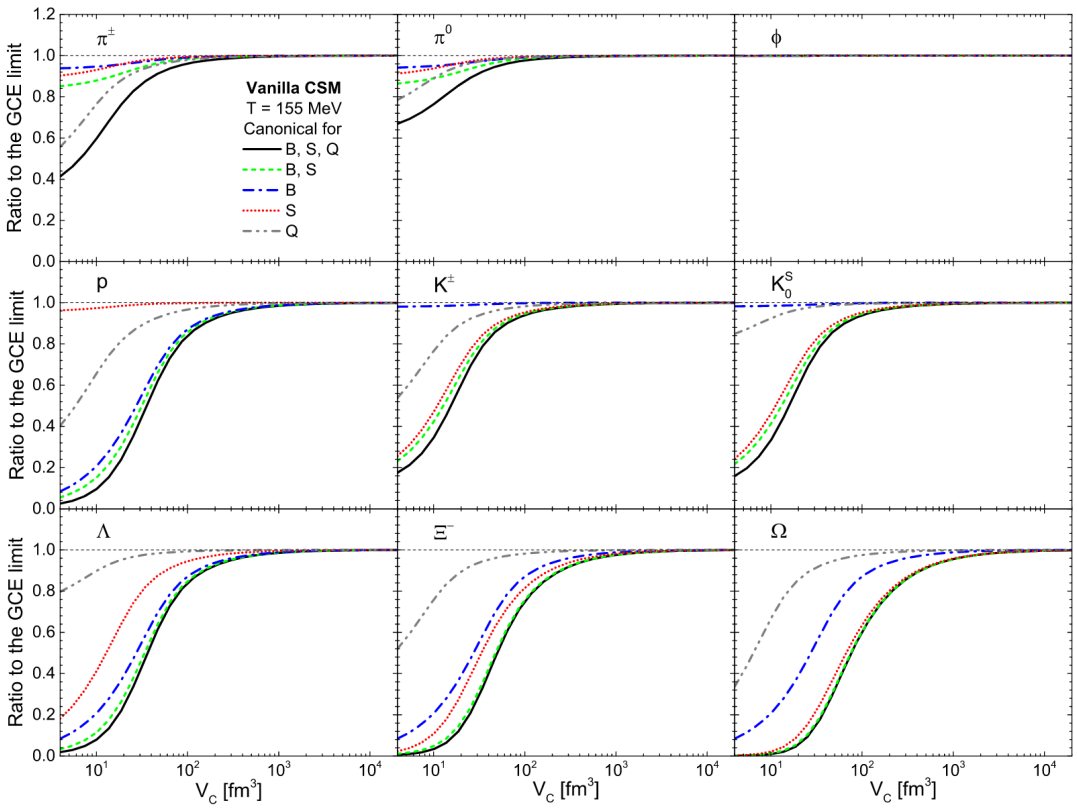

Fig. 3.2 Correlation volume dependence of the ratios of various final hadron yields calculated in different canonical approaches over the GC values. Calculations are performed at $T = 155$ MeV. Figure taken from [113].

by the continuous black line, while the other lines correspond to intermediate configurations between a CSM and a GC approach. Except for the ϕ meson, which is not sensitive to the variation of the conservation laws, the other hadron species behave qualitatively similarly as a function of V_c: for large correlation volumes, corresponding to central Pb–Pb collisions, the CSM predictions saturate, reaching the values of the GC SHM. Moving to lower correlation volumes, a smooth decrease of the ratio is observed, until a minimum is reached for low multiplicity pp collisions, namely for $V_c \approx 1$ fm^3. This effect will be discussed in details and compared to the experimental measurements of the light nuclei and strange particles production in Sec. 4.11 and in Sec. 5.10, respectively.

3.1.3 Hydrodynamic models

At present, there is not a unique theoretical description capable of modelling the nucleus-nucleus collisions provided by the LHC. Alongside the coalescence and SHM models

discussed in the previous Sections, a large sample of models inspired by the principles of hydrodynamics [99] was exploited to describe low-momentum ($p_{\mathrm{T}} \lesssim 3$ GeV/c) particle production in heavy ion collisions. In particular, this class of models tries to describe the fireball evolution, as long as the thermal equilibrium condition is met, by requiring a set of equations to be conserved during the relativistic hydrodynamic evolution of the system. Typically, models apply the conservation of quantum numbers, energy and momentum. The hydrodynamical evolution of the system may be carried out within the ideal limit, meaning with null viscosity, if it is performed in a perfect medium without dissipations, or with viscosity. When finally the thermal equilibrium condition is broken, the transition from the hydrodynamical fluid to free particles is performed with a Cooper-Frye freeze-out approach [114], assuming the same momentum distribution for local fluid elements and particles which are produced within that volume. Since these models describe only the evolution of the fireball, they must be provided with a set of initial conditions which are used as a starting point for the hydrodynamic calculations. Usually, the conditions used as inputs are an equation of state, an energy density and a pressure.

An example from this class of models is the New causal Viscous Israel-Stewart Hydrodynamics in 2+1 space-time dimensions (VISHNew) [115] model. The initial conditions used by this model are provided by a Glauber Model [89], a phenomenological model which describes the nucleus-nucleus collisions in terms of the elementary collisions of the constituent nucleons, based on geometrical assumptions only. On top of these initial conditions, a system evolution based on the conservation of energy-momentum in a Eulerian space defined by curvilinear coordinates (τ, x, y, η) is applied. In this coordinate system, x and y represent the two directions transverse to the beam axis z, $\tau = \sqrt{t^2 - z^2}$ is the longitudinal proper time and $\eta = \frac{1}{2} \ln \frac{t+z}{t-z}$ is the space-time rapidity. The particle invariant spectra are calculated with a Cooper-Frye integral as

$$E_{\mathrm{i}} \frac{\mathrm{d}^3 N_{\mathrm{i}}}{\mathrm{d}p_{\mathrm{i}}^3} = \frac{g_{\mathrm{i}}}{(2\pi)^3} \int_{\Sigma} p \cdot \mathrm{d}^3\sigma(x) \left[f_{\mathrm{eq}}^{(\mathrm{i})}(x,p) + \delta f^{(\mathrm{i})}(x,p) \right] \tag{3.17}$$

where Σ is the surface of the fireball at the kinetic freeze out, supposed to happen at a constant temperature $T = 130$ MeV and $\mathrm{d}^3\sigma$ is its normal versor. The integral is performed over two terms: the first one, $f_{\mathrm{eq}}^{(\mathrm{i})}(x,p)$, is the local thermal equilibrium distribution provided by the hydrodynamical evolution of the system for the particle species i and depends on the spatial and momentum coordinates x and p. The second term, $\delta f^{(\mathrm{i})}(x,p)$, describes any possible deviation from local thermal equilibrium due to viscous effects and can be approximated as

$$\delta f^{(\mathrm{i})}(x,p) = f_{\mathrm{eq}}^{(\mathrm{i})}(x,p) \cdot \frac{1}{2} \frac{p^\mu p^\nu}{T^2} \frac{\pi_{\mu\nu}}{e+p} \tag{3.18}$$

where $\pi_{\mu\nu}$ is the viscous pressure tensor, p^{μ} is the 4-momentum vector and $e+p$ is the equilibrium enthalpy of the system. The main limit of this approach is due to the fact that, even if the latter is generally a small correction to the former term, it grows quadratically with momentum, thus it leads to a breakdown of the hydrodynamical viscous approach at high momentum, where the integral is no more dominated by the equilibrium distribution. Anyhow, comparisons to the Relativistic Heavy-Ion Collider (RHIC) results [116] obtained in Au–Au collisions at $\sqrt{s_{NN}} = 200$ GeV have shown that a hydrodynamical description within the ideal limit, meaning with null viscosity, describes the evolution of a QGP state better than viscous hydrodynamics.

3.1.4 Microscopic models

Another possible approach to describe the evolution of an hadronic collision relies on modelling as precisely as possible the interactions characterizing the fireball expansion. In particular, one has to deal with a large number of possible interactions and mechanisms which depend on the energy scale of the collision. While at energy scales up to the critical temperature for the QCD phase transition $T_c \approx 160$ MeV a description in terms of hadrons and resonances is appropriate, at higher energies the quark and gluon degrees of freedom become the leading actors of the interactions.
An example of microscopic model is given by the Ultra-relativistic Quantum Molecular Dynamics (UrQMD) model [100, 101]. The description of the model starts from the definition of the colliding nuclei, which are treated as a Fermi gas with Gaussian-shaped nucleons. Then the trajectories and interactions of all particles are determined individually throughout the evolution of the system. This is done by solving the collisional Boltzmann equation with a potential which is given by the sum of Yukawa, Coulomb and Skyrme [117] effective potentials. The most relevant input for this calculation stands in the knowledge of all the possible interaction cross sections and the decay widths for the unstable particles, which must be well constrained in order to obtain a reliable description of the microscopic processes characterizing the fireball. The main difficulty of this approach is due to the presence of the hot and dense medium formed in the collision, which might change significantly these quantities with respect to the ones known in vacuum. For this reason important approximations are needed whenever an hadronic cross section is not known: in such a case, the Additive Quark Model (AQM) [118] is used to extrapolate the hadronic cross section from the known one coming from elementary quarks.
Usually, in order to avoid extrapolation, the UrQMD model is coupled to an event generator which is responsible for the description of the in-medium interactions: as an example, the

combination of the UrQMD model and the EPOS3 [119, 120] event generator was able to describe the production of hadronic resonances measured by the ALICE experiment in Pb–Pb collisions at $\sqrt{s_{\rm NN}} = 2.76$ TeV [121].

3.2 (Anti)nuclei production in pp collisions

The measurement of nuclei and antinuclei production in pp collisions can provide an interesting comparison between the predictions of the CSM and the coalescence model.
In particular, the CSM is implemented into a package called Thermal-FIST [122], where charge, strangeness content and baryon number are exactly set to zero in the initial status. The remaining free parameters of the models, as described in Sec 3.1.2, are the chemical freeze-out temperature T and the correlation volume $V_{\rm c}$, whose effect on the predictions can be tested with a variation of the used values. From previous measurements performed in Pb–Pb collisions at $\sqrt{s_{\rm NN}} = 2.76$ TeV [123], a temperature value $T = 155$ MeV seems to be favoured, even though another configuration with $T = 170$ MeV is also tested. Since the correlation volume in which the charges are conserved may change event by event, also this parameter is varied: in this study the two values $V_{\rm c} = {\rm d}V/{\rm d}y$ and $V_{\rm c} = 3({\rm d}V/{\rm d}y)$ are tested. The predictions from the model are reported as a function of pion multiplicity ${\rm d}N_\pi/{\rm d}y$ in Fig. 3.3 together with ALICE measurements [124–127] in different collision systems. The nuclei-to-proton yield ratio is evaluated for deuterons (a), helions (b), hypertritons (c) and alpha particles (d). For the two lightest among these nuclear species, deuterons and helions, measurements are available in both pp and Pb–Pb collisions. The measurement of such a ratio was not performed in pp collisions for heavier particles such as hypertritons, a bound state of a deuteron and a Λ particle, and alpha particles, made up of two protons and two neutrons because a higher statistics is needed. This is due to the combination between the canonical suppression effect and the exponential decrease of the production yields as a function of the mass number of the nucleus [128]. The predictions grow monotonically from low to high pion multiplicity, reaching a saturation region which corresponds to the grand canonical value. The comparison to data helps in testing the different parameterizations of the Thermal-FIST model: when the values $T = 155$ MeV and $V_{\rm c} = 3({\rm d}V/{\rm d}y)$ are assumed, the level of agreement is better with respect to other configurations of the free parameters.
As described in Sec. 3.1.1, a refined implementation of a coalescence model which takes into account both spacial and momentum distributions of nucleons can provide predictions of nuclei-to-proton ratios as well. In particular, the expectations from such a model [111] are reported in Eq. 3.8 and Eq. 3.9 and depend on the neutron multiplicity $N_{\rm n}$, on the temperature

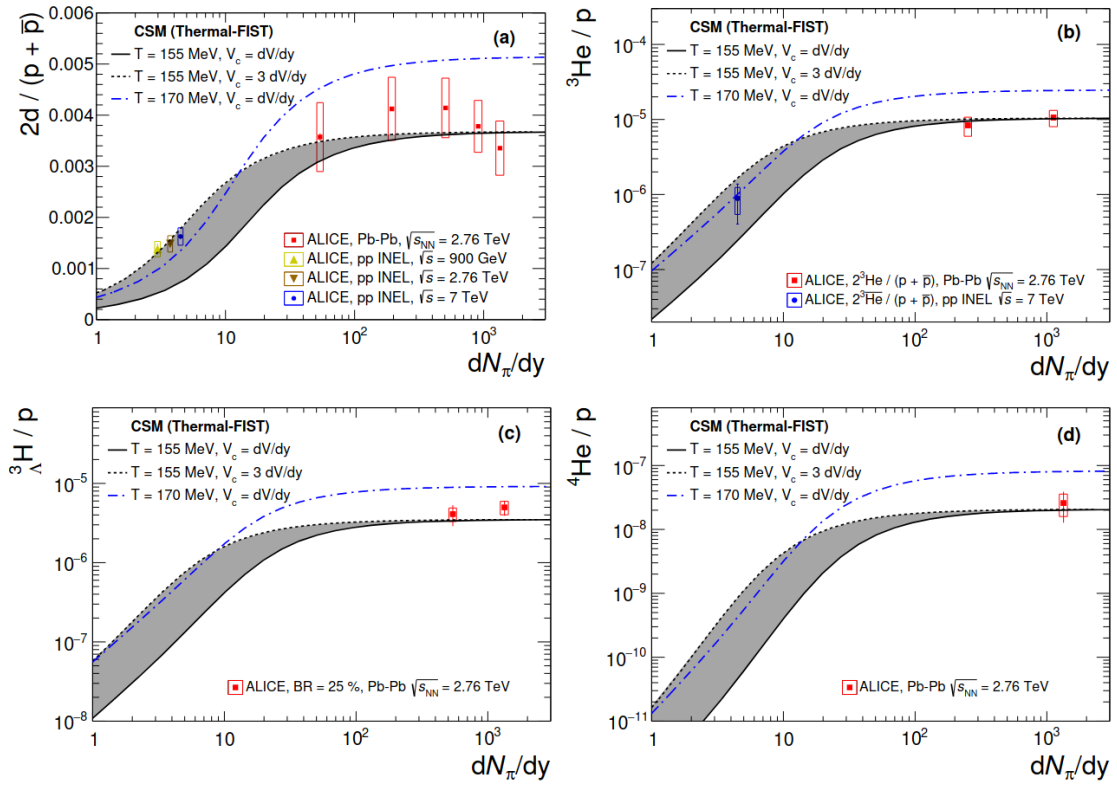

Fig. 3.3 Predictions from the Thermal-FIST package for the deuteron-to-proton (top left), helion-to-proton (top right), hypertriton-to-proton (bottom left) and 4-helion-to proton yield ratios. Three parameterizations of the CSM are reported: $T = 155$ MeV for $V_c = \frac{dV}{dy}$ (solid black line), $T = 155$ MeV for $V_c = 3\frac{dV}{dy}$ (dashed black line) and $T = 170$ MeV for $V_c = \frac{dV}{dy}$ (dash-dotted blue line). Experimental data from the ALICE experiment [124–127] are also reported. Figure taken from [122].

of kinetic freeze-out T_{k} and on the emitting source radius R. In order to fix these parameters, the model takes into account the ALICE measurements [129–131] of pion, kaon and proton production across different collision systems performed as a function of charged particle multiplicity. The nuclei-to-proton ratio predictions for deuteron and helion together with the triton-to-helion ratio are reported in Fig. 3.4 as a function of the charged particle multiplicity of the event. For nuclei with mass number $A = 3$, the coalescence predictions are reported both for a two body coalescence (red), meaning for a coalescence between a deuteron and a proton, and for a three body coalescence, where three nucleons form a nucleus via coalescence at the same time. A smooth behavior across multiplicity is foreseen also by this implementation of the coalescence model, similarly to what was shown for a CSM.
Nuclei production in high-energy hadronic collisions can thus be explained by using models which are based on really different assumptions and relies on complementary mechanisms, leading to similar behavior, at least from a qualitative point of view. In this context, a more comprehensive discussion and comparison between these two models is needed, in order to understand the mechanism responsible for nuclei production. In the concluding part of next Chapter such a comparison will be discussed in details and a comparison with the results obtained from this work and from previous analyses will be reported.

3.3 Strange particle production in Pb–Pb collisions

The production of strange particles in heavy-ion collisions is considered a relevant research field since the strangeness enhancement phenomenon, introduced in Sec. 1.4.1, was suggested as a key signature for the observation of the QGP formation [28]. In order to described the production of strange particles in heavy-ion collisions, very different approaches based on SHM, hydrodynamic and microscopic models can be exploited.
The grand canonical SHM provides a good description of the production yields measured, for different particle species, in heavy-ion collisions: the fit to the ALICE measurements in Pb–Pb collisions at 2.76 TeV [130, 132, 133, 32, 124, 126, 125] in the centrality class 0–10% is reported in Fig. 3.5. Four different parameterizations of the SHM are reported: THERMUS [134], SHARE [135], GSI-Heidelberg [112] and Thermal-FIST [122]. All the models show similar qualitative results, being able to describe properly the production of light flavor particles with the usage of a common chemical freeze-out temperature $T \approx 155$ MeV. When referring explicitly to the strangeness sector, meaning the K and ϕ mesons and the Λ, Ξ and Ω baryons, discrepancies smaller than 2σ between the fit result and the ALICE data are observed.

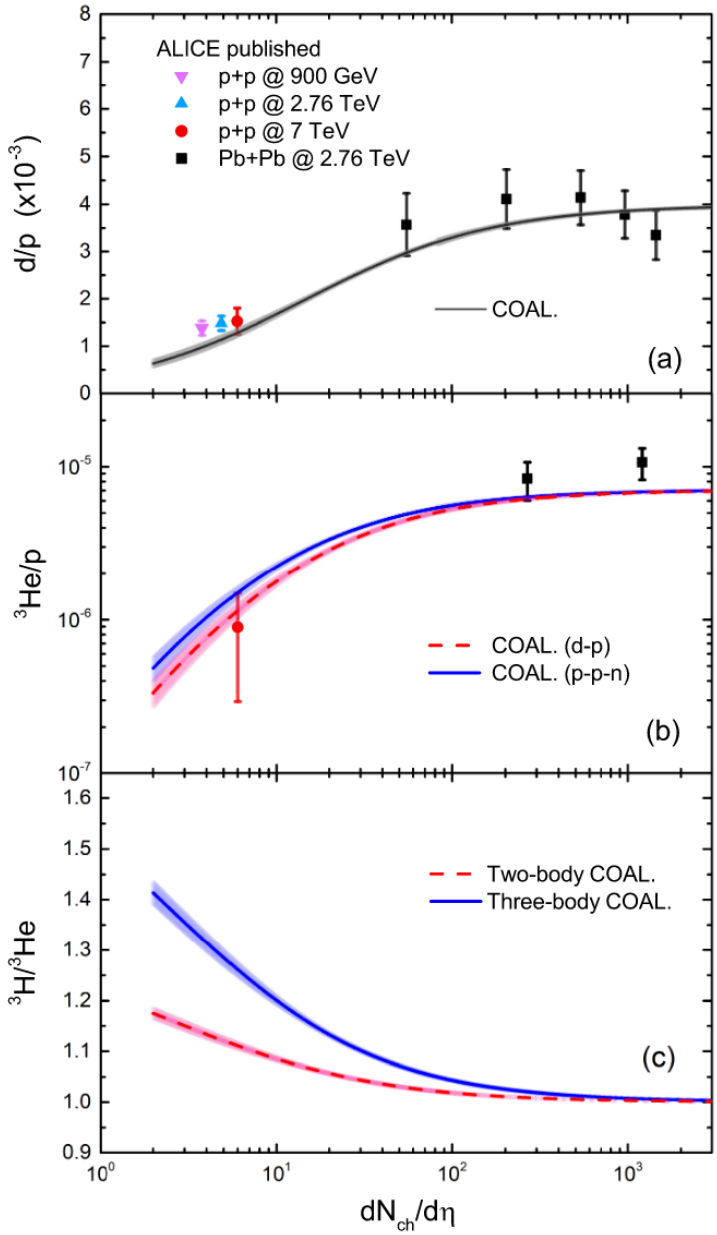

Fig. 3.4 Deuteron-to-proton (top), helion-to-proton (center) and triton-to-helion (bottom) yield ratios as a function of charged particle multiplicity. Data collected both in pp and in Pb–Pb collisions by the ALICE experiment [124, 127, 130, 131] are also reported. The predictions of the coalescence model, with theoretical uncertainties due to the emission source radius, are reported with the shaded bands. For nuclei with three nucleon content the magenta and the blue lines correspond to two-body and three-body coalescence, respectively. Figure taken from [111].

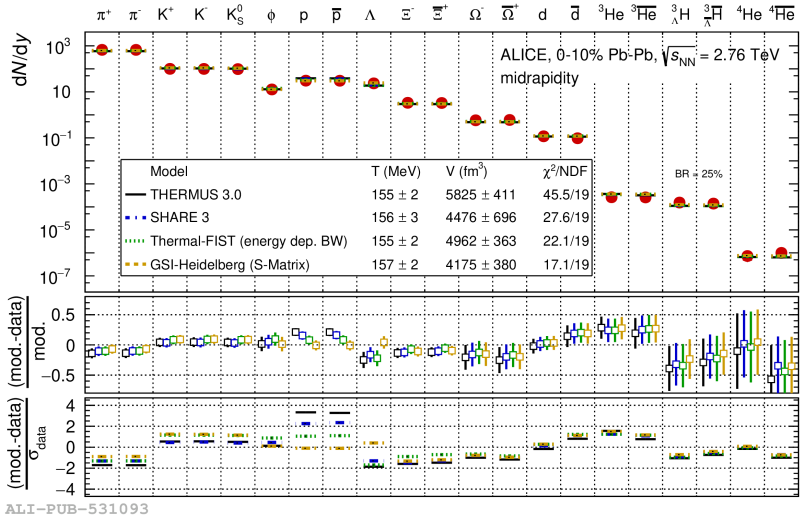

Fig. 3.5 Thermal model fit to the light-flavor hadron yields in central Pb–Pb collisions at 2.76 TeV [130, 132, 133, 32, 124, 126, 125]. Four different implementations of the model are reported with different colors: THERMUS [134] (solid black), SHARE [135] (dash-dotted blue), Thermal-FIST [122] (dotted green) and GSI-Heidelberg [112] (dashed yellow). Figure taken from the ALICE figure repository ©.

As for nuclei production, a canonical approach to the SHM can also be used for the strangeness sector: the THERMUS package provides predictions for the ratios between strange hadrons and pion yields. The results obtained with a specific implementation of the package [136] are reported for various strange particles in Fig. 3.6 together with a comparison to ALICE data [33, 137, 138, 35, 132, 130, 32, 133] as a function of pion multiplicity. For what concerns the model, the radius of the emitting source was varied in order to test the data ranging from small multiplicities (pp collisions) up to high pion multiplicities which are typical of central Pb–Pb collisions. A chemical freeze-out temperature $T_{\rm ch}$ in the range between 146 and 166 MeV is set in order to take into account its effect on the predictions, even though it shows a mild effect due to the chosen normalization: both data and the model predictions are normalized to the data ratio in the 0–60% most central Pb–Pb collisions. Except for the K^{0*} and ϕ mesons, whose interpretation is not straightforward in the strangeness sector due to additional effects like rescattering [139, 140] and potential out of equilibrium production [133], the model describes qualitatively the data and predicts the aforementioned strangeness enhancement with a smooth behavior across the different colliding systems. This is another important demonstration on how reliable predictions can be when they are provided by a static model like the SHM.

The dynamics of strange particles can also be studied with respect to the evolution of the fireball by using hydrodynamic and microscopic models. In particular, a hybrid approach

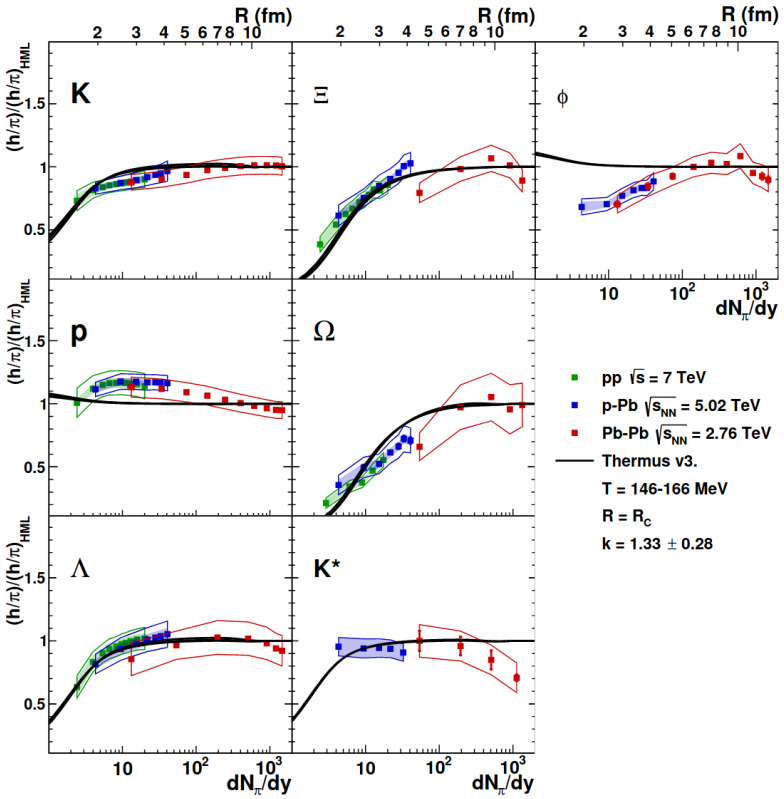

Fig. 3.6 Ratio between strange particle and pion yields evaluated via the THERMUS package. ALICE results [33, 137, 138, 35, 132, 130, 32, 133] obtained across different collision systems and at various energies are also reported. Figure taken from [136].

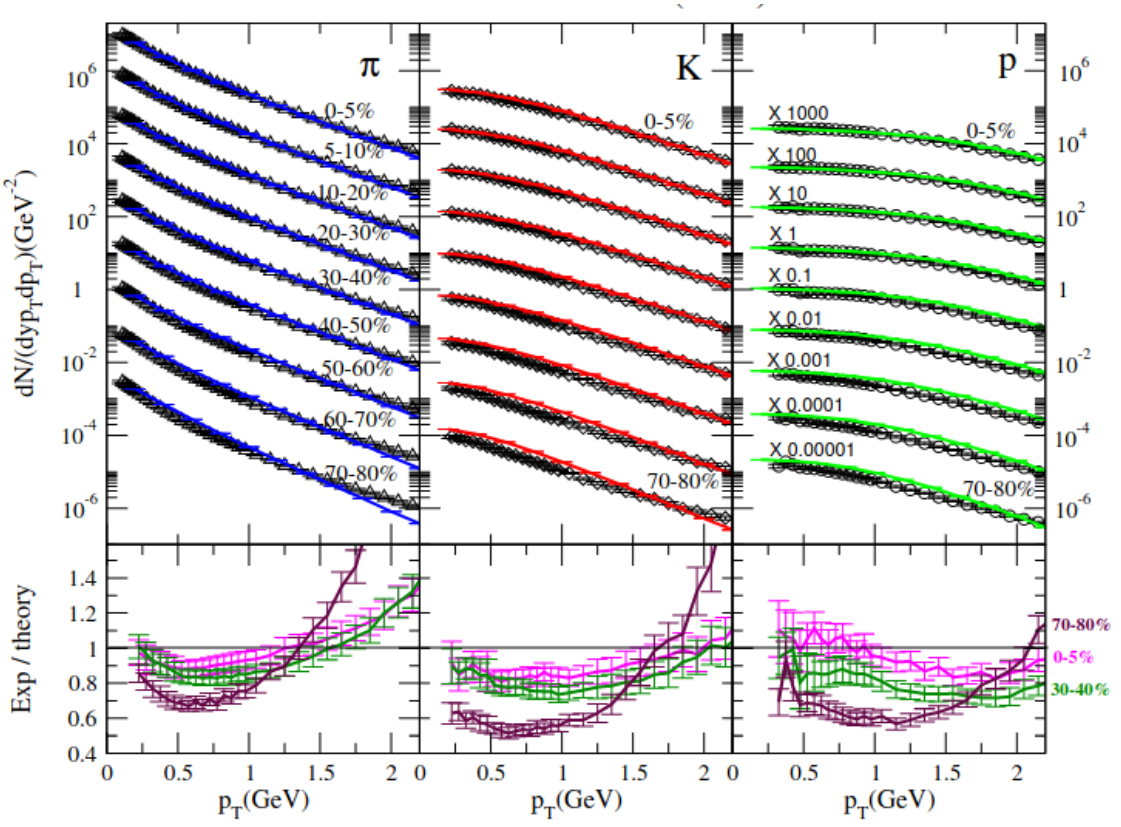

Fig. 3.7 Top: transverse momentum spectra in different centrality classes measured by the ALICE experiment in Pb–Pb collisions at 2.76 TeV [130] for pions (left), kaons (center) and protons (right). Theoretical curves from a VISHNU simulation are also reported. Bottom: ratio between data and model predictions for the 0–5%, 30–40% and 70–80% centrality classes. Figure taken from [142].

based on the combination of the VISHNew [115] and UrQMD [100, 101] models, called VISHNU [141], is used to describe particle production spectra in the low transverse momentum region. The VISHNU basic workflow consists on performing a hydrodynamical evolution of an initial state, which is usually provided by a MC generator or by a Glauber model simulation, by using the VISHNew model. At the end of the hydrodynamic calculation, the fluid cells are converted into particles as described in Sec. 3.1.3 and are then forced to undergo a subsequent dynamical evolution via a UrQMD model, where each particle is considered in its trajectory, interactions and eventual decay. At the end of this stage, the obtained final state of stable particles can be compared to data. This approach showed promising results in describing the production spectra of light flavor particles: the comparison between the transverse momentum spectra measured by the ALICE experiment [130] for pions, kaons and protons in different centrality classes and the VISHNU predictions [142] is reported in the top panel of Fig 3.7. The ratio between data and model predictions, reported

in the lower panel, shows how the VISHNU code can reproduce reasonably well, at least from a qualitative point of view, the data in the central (0–5%) and semi-central (30–40%) regions, in particular for protons. On the other hand for peripheral collisions (70–80%) a large difference between data and VISHNU predictions is observed over the whole transverse momentum range of the measurement. This behavior is expected since models based on hydrodynamics usually perform better for central collisions: the system radius is larger in central than in peripheral collisions, and so the hydrodynamic expansion lasts longer. From this comparison a hydrodynamic evolution of the system seems to be more suitable for central than for peripheral collisions.

Finally, an additional approach based on a revised combination of hydrodynamic and microscopic evolution of the system is given by the EPOS4 [102] event generator. The initial stage of this framework consists in the simulation of the hadron-hadron interaction, which is carried out via the S-matrix theory [143], a field theory calculation dedicated to solve parton scattering problems. The main difference with respect to the VISHNU model resides in how the system created in the collision is treated. In the EPOS4 model the system is divided in two parts: core and corona [144]. The core, characterized by high energy density and hard scattering processes, can be identified with the deconfined medium and evolves under the principles of hydrodynamics until a hadronization phase, whose occurrence is set depending on the energy density of the system. The corona part, which surrounds the core, is characterized by a confined phase and no hydrodynamic evolution is foreseen. As a final step, a microscopic evolution via a UrQMD model is applied to the system, until no further interaction between the hadrons of the system is observed. The EPOS4 model is able to provide a good description of the ALICE measurements: as an example, the yield ratio to pions (left) and the average transverse momentum are reported in Fig. 3.8 for the Ω baryon measured in pp collisions at $\sqrt{s} = 7$ TeV [33] and in Pb–Pb collisions at $\sqrt{s_{\rm NN}} = 2.76$ TeV [32]. Four different predictions from the EPOS4 model are reported in order to disentangle the effect of the procedure used in the calculation: full EPOS4 model (red), core-corona without UrQMD evolution (yellow), corona-only (blue) and core-only (green). For both the observables, the core contribution is always significantly higher than the corona one, which anyway can not be neglected in order to obtain a good description of data. On the contrary, the effect of the UrQMD evolution has a minor effect, even though not negligible, in particular for the yield ratio. An overall qualitatively good description of data can be obtained when the full calculation is performed.

In conclusion, in order to understand the properties of the medium produced in high-energy hadronic collisions, the results coming from SHM and microscopic models need to be considered: on one hand the SHM is able to provide a good description of data over a wide range

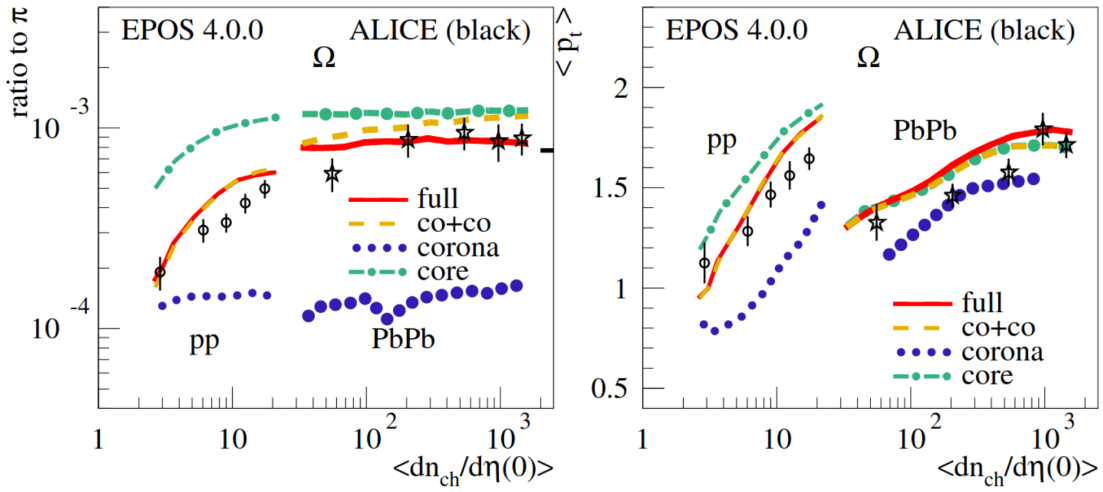

Fig. 3.8 Predictions for the ratio of the Ω and π yields (left) and average transverse momentum of the Ω baryon (right) as a function of the average particle multiplicity produced at midrapidity $\langle \mathrm{d}\rangle \mathrm{n_{ch}}/\mathrm{d}\eta(0)$, compared to the ALICE measurements in pp collisions at $\sqrt{s} = 7$ TeV [33] (circles) and in Pb–Pb collisions at $\sqrt{s_{\mathrm{NN}}} = 2.76$ TeV [32] (stars). Four different implementations from the EPOS4 model are reported: full EPOS4 model (red), core-corona without UrQMD evolution (yellow), corona-only (blue) and core-only (green). Figure taken from [102].

of physical processes with a statistical-only approach. On the other hand, the underlying processes which are not taken into account in SHM are implemented in hydrodynamical and microscopic models and should be considered to provide further constraints on the medium properties. In the final part of Chapter 5, the SHM, the VISHNU model and the EPOS4 event generator will be compared with measurements in the strangeness sector from previous analyses and from this work in order to test the capability of these approaches to describe the strange particle production in high energy collisions across different collision systems.

Chapter 4

Light nuclei production in pp collisions at 5.02 TeV

The initial part of the thesis project aims to measure the production of protons (p), deuterons (d), helions (^{3}He) and their antimatter counterparts ($\overline{\mathrm{p}}$, $\overline{\mathrm{d}}$, $\overline{^3\mathrm{He}}$) in pp collisions at $\sqrt{s} =$ 5.02 TeV. Since particles and antiparticles are analyzed in the same way in this thesis work, the particle names (symbols) protons, deuterons and helions (p, d, ^{3}He) will refer both to matter and antimatter. Explicit reference will be made only when necessary to highlight specific differences and avoid ambiguities. In the following, each step of the work which has been carried on during this part of the thesis project will be discussed in details. Whenever part of it has been inherited from previous works, this will be highlighted and references will be given.

4.1 Analysis strategy

The measurement of light nuclei production is a complex procedure based on different steps, which will be described in detail in the following sections. First of all, a defined set of selections is applied to both events and reconstructed tracks in order to restrict the analysis to high-quality data: in particular, only tracks with complete information from the central barrel detectors and with good enough resolution are used for this analysis. The second step consists on the selection of good light-nuclei candidates through the application of particle identification techniques to the above selected tracks, a task which is performed using either the TPC or the TOF detectors. For transverse momentum up to $p_{\mathrm{T}} = 1$ GeV/c, the TPC information is sufficient to separate nuclei from the other particle species. At higher p_{T}, the

TOF detector is introduced to improve purity. The number of detected nuclei tracks has to be corrected for the detector efficiency and acceptance, the fraction of candidates not coming from the interaction point and the number of events lost due to trigger inefficiencies. This information can not be extracted from the experimental data and must be obtained from MC simulations. The first results of this analysis consist on the nuclei transverse momentum spectra, which are obtained by combining the signal extraction and the subsequent corrections. Two key observables such as the average transverse momentum and the production yields of nuclei are extracted with a fit to the spectra, allowing for a comparison between this work and previously published analyses. Finally, the coalescence parameters and the ratio between the production yields of nuclei and protons are evaluated and compared to the predictions coming from the theoretical models described in the previous Chapter.

4.2 Data and Monte Carlo samples

This analysis consists of nearly $1.1 \cdot 10^9$ pp collisions at $\sqrt{s} = 5.02$ TeV, the whole pp data sample collected by ALICE in 2017. Two complementary detector read-out strategies were adopted to enhance the number of collected inelastic events, both of them triggered requiring a coincidence signal from the V0A and V0C detectors. The first one consists in reading-out all the central barrel detectors and it is called CENT. Its main disadvantage is due to the limited number of events which can be collected, since one of the read-out detectors, the SDD, has a significantly larger busy time (≈ 1 ms) than the other central barrel detectors. In order to cope with this issue, the FAST read-out strategy was adopted, consisting in the exclusion of the SDD detector from the data acquisition.
Monte Carlo (MC) simulations played a crucial role in many steps of this analysis, ranging from the efficiency and acceptance correction to the evaluation of systematic uncertainties, as described in Sec. 4.7. Simulated samples were developed to mimic real data by implementing the same conditions and experimental setup which characterized the data taking period exploited for this analysis (anchoring procedure). A detailed list of the MC productions used is reported in details in Table 4.1. Inelastic collision events were generated by means of the PYTHIA [145] code, which does not provide a sizeable nuclei sample at reasonable CPU cost. For this reason it was necessary to inject deuterons and helions in each event. As an example, on top of each MC event used for the Efficiency x Acceptance correction, nuclei were injected with the following scheme: one d and one ^{3}He (or their antimatter counterparts) where injected with a flat transverse momentum distribution in the range $0 < p_{\mathrm{T}} < 6$ GeV/c. Additionally, some MC Pb–Pb events, produced with the HIJING [83] event generator, were

Purpose	n. of Events	Event Generator	Transport Code
Eff x Acc	$2.06 \cdot 10^8$	PYTHIA	GEANT4
Secondary Nuclei	$3.95 \cdot 10^8$	PYTHIA	GEANT3
Material Budget	$4.08 \cdot 10^5$	HIJING	GEANT3
Trigger-induced Signal Loss	$3.06 \cdot 10^8$	PYTHIA	GEANT4

Table 4.1 Overview of the MC samples used in the nuclei analysis.

used to estimate the amount of matter, called detector material budget, traversed by the nuclei candidates. This sample is characterized by significantly larger track densities with respect to PYTHIA-based simulations and, moreover, the material budget did not change during the whole Run2 campaign and does not depend on the collision system. Depending on the MC production, either the GEANT3 [85] or the GEANT4 [86] transport codes were used to deal with the energy loss of particles in the detector, the generation of secondary particles from the material and the decay of unstable particles.

4.3 Event selection

On top of the online trigger selection described previously, a further offline event selection procedure is required in order to solely retain events for which the ALICE apparatus can provide prime reconstruction capabilities. Following the prescription of the Data Preparation Group of ALICE for the analysis of pp collision events acquired during the LHC Run2 campaign, a standard set of event selections are adopted and summarized in Table 4.2. The first selection consists on retaining events with at least one charged particle track in the acceptance region $|\eta| < 1$ (INEL > 0) and rejecting events containing pile-up. The so called in-bunch pile-up, which consists of two or more inelastic events happening in the same bunch crossing or in bunch crossings separated by less than the SPD read-out time (≈ 300 ns), is rejected exploiting the correlation between the number of clusters and tracks in the SPD detector. Additional selections are related to the vertex reconstruction quality and position. The vertex position along the beam axis is evaluated with the SPD ($v_z^{(\mathrm{SPD})}$) and after the complete tracking process ($v_z^{(\mathrm{TRK})}$): if the difference between the coordinates obtained with the two methods is larger than 0.5 cm, the vertex estimation is considered as not precise enough and the event is rejected. Finally, only events with an estimated vertex position v_z in the fiducial region ± 10 cm around the collision point are accepted, in order to grant a symmetric acceptance. The number of selected events for each step of the selection chain is reported in Fig. 4.1.

Event Selections
$\lvert v_z \rvert \leq 10$ cm
Pile-up rejection
$\left\lvert v_z^{(\mathrm{SPD})} - v_z^{(\mathrm{TRK})} \right\rvert \leq 0.5$ cm

Table 4.2 List of event selection criteria.

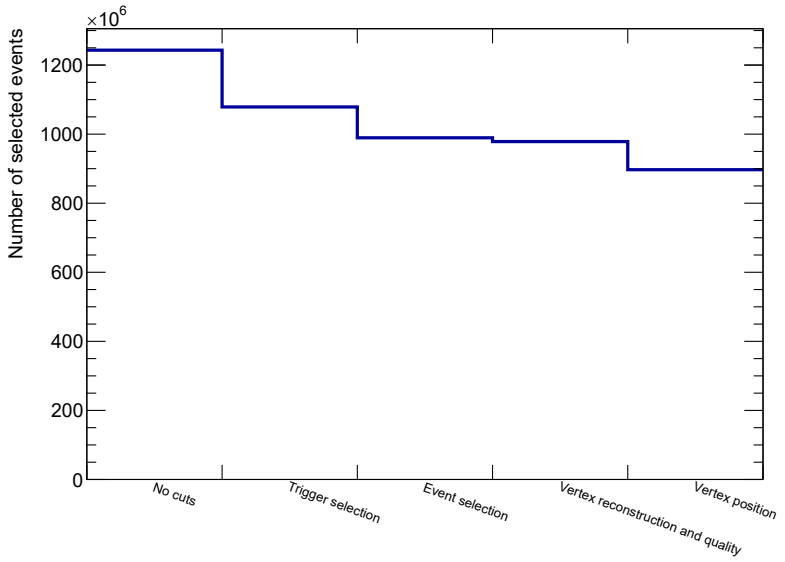

Fig. 4.1 Number of accepted events at each step of the event selection.

All the accepted events, both in data and MC samples, are characterized by a certain number of produced charged particles in the acceptance region $|\eta| < 0.5$ and are consequently split into charged particle multiplicity classes. The chosen multiplicity classes are reported in Table 4.3 for protons and deuterons and in Table 4.4 for helions, together with the mean charged particle multiplicity ($\langle \frac{\mathrm{d}N_{\mathrm{ch}}}{\mathrm{d}\eta_{\mathrm{lab}}} \rangle$) of the events included in each class [88]. The number of multiplicity classes exploited for the helion analysis is smaller than for protons and deuterons due to the limited number of helion candidates with respect to the proton and deuteron ones: this effect is due to the suppression of the production yields of nuclei depending on their mass number A, as will be discussed in Sec. 4.9.

4.4 Track selection

A second set of offline selections is applied directly on each reconstructed track to ensure a high quality data sample. First of all, tracks are retained in the mid-rapidity region

Class	Multiplicity (%)	$\langle \frac{dN_{ch}}{d\eta_{lab}} \rangle$
I	0 - 1	$18.45^{+0.26}_{-0.22}$
II	1 - 5	$14.47^{+0.20}_{-0.16}$
III	5 - 10	$11.92^{+0.16}_{-0.13}$
IV + V	10 - 20	$9.72^{+0.14}_{-0.11}$
VI	20 - 30	$7.76^{+0.11}_{-0.09}$
VII	30 - 40	$6.34^{+0.09}_{-0.07}$
VIII	40 - 50	$5.22^{+0.08}_{-0.06}$
IX	50 - 70	$3.94^{+0.06}_{-0.05}$
X	70 - 100	$2.43^{+0.04}_{-0.03}$
INEL > 0	0 - 100	$5.49^{+0.08}_{-0.06}$

Table 4.3 Summary of the multiplicity classes and the related mean charged particle multiplicity $\langle \frac{dN_{ch}}{d\eta_{lab}} \rangle$ for protons and deuterons. The $\langle \frac{dN_{ch}}{d\eta_{lab}} \rangle$ values were measured for $|\eta_{lab}| < 0.5$ [88].

Class	Multiplicity (%)	$\langle \frac{dN_{ch}}{d\eta_{lab}} \rangle$
I - III	0 - 10	$13.81^{+0.19}_{-0.15}$
IV - X	10 - 100	$4.91^{+0.07}_{-0.06}$
INEL > 0	0 - 100	$5.49^{+0.08}_{-0.06}$

Table 4.4 Summary of the multiplicity classes and the related mean charged particle multiplicity $\langle \frac{dN_{ch}}{d\eta_{lab}} \rangle$ for helions. The $\langle \frac{dN_{ch}}{d\eta_{lab}} \rangle$ values were measured for $|\eta_{lab}| < 0.5$.

Variable	Selection
$\lvert\eta\rvert$	< 0.5
$\lvert y\rvert$	< 0.8
TPC clusters	≥ 70
ITS clusters	> 1
SPD clusters	> 0
$\lvert\mathrm{DCA_z}\rvert$	< 1 cm
$\left\lvert\mathrm{DCA_{xy}}\right\rvert$	< 0.12 cm
χ^2 per TPC cluster	≤ 2.5
χ^2 per ITS cluster	≤ 36
ITS refit	true
TPC refit	true
Kink topologies	rejected

Table 4.5 Outlook of the track selections applied in this work.

$|y| < 0.5$ and in the pseudorapidity region $|\eta| < 0.8$ only, in order to provide full-length track reconstruction and to ensure near to nominal PID capabilities. Good transverse momentum and specific energy loss resolutions (2% and 6%, respectively) can be obtained by requiring tracks to have at least 70 clusters in TPC and two clusters in the ITS, with at least one of them in the SPD. Secondary nuclei are rejected thanks to additional selections on the DCA, which has been defined in Sec. 2.6.2. Since primary nuclei are expected to come from the primary vertex, only tracks with $|\mathrm{DCA_z}| < 1$ cm and $\left|\mathrm{DCA_{xy}}\right| < 0.12$ cm are accepted. A resolution better than 300 μm on the $\mathrm{DCA_z}$ and on the $\mathrm{DCA_{xy}}$ is obtained by applying the above-mentioned rejection of tracks without clusters in the SPD. Additional selections are related to the track fitting procedure: tracks are required to be refitted both in TPC and ITS, with a maximum value of χ^2 per cluster of 2.5 and 36 for TPC and ITS, respectively. Finally, the leptonic weak decays of pion and kaon mesons are identified and rejected based on the presence of a kink in the particle track. Table 4.5 summarizes the described track selections.

4.5 Signal extraction

The number of produced light nuclei (raw signal) is extracted as a function of the transverse momentum for each multiplicity class defined in Sec. 4.2. Depending on the transverse momentum region where the analysis is performed, two different detectors are used to perform particle identification: the TPC and the TOF. The signal extraction method depends on the detector used for PID and on the nucleus under study. A detailed explanation of the two techniques is given in the following.

TPC PID By means of the TPC PID technique, which is described in Sec. 2.6.3, for each track fulfilling the above mentioned selections it is possible to obtain the distance in nσ units from the expected d$E/$dx for a given particle hypothesis. The nσ distributions can be described by the sum of a signal and a background function to take into account the possible contamination from other particle species, whose exact functional form depends on the particle under study. The raw signal is extracted integrating the signal function over the complete nσ range. The analysis is performed in p_{T} and multiplicity intervals, whose width is driven by the abundance of candidates.

TOF PID The alternative particle identification strategy relies on the TOF capability to evaluate particle masses, starting from a time-of-flight measurement. As described in details in Sec. 2.6.3, two variables can be arranged starting from the TOF signal: the nσ information and the squared mass of a particle m^2_{TOF}. In order to increase purity in the TOF analysis, an additional 3σ cut on the TPC nσ value is performed, so that the nσ_{TOF} and m^2_{TOF} distributions can be optimally modeled with a sum of a signal and a background function. In some transverse momentum regions the background component is not null, thus the raw signal is evaluated with the same procedure described for the TPC analysis in the previous paragraph. Otherwise the bin counting method is applied.

4.5.1 Proton

The proton analysis relies on both the TPC and the TOF particle identification. For low transverse momentum values, namely from 0.30 GeV/c up to 1.00 GeV/c, the information coming from the TPC is used. The TPC nσ signal distribution is described with a gaussian with two exponential tails, defined as

$$sig(x) \propto N_{\mathrm{raw}} \begin{cases} e^{-(x-\mu-\frac{\alpha_1\sigma}{2})\frac{\alpha_1}{\sigma}} & \text{for } x < \mu + \alpha_1\sigma \\ e^{-\frac{(x-\mu)^2}{2\sigma^2}} & \text{for } \mu + \alpha_1\sigma \leq x \leq \mu + \alpha_0\sigma \\ e^{-(x-\mu-\frac{\alpha_0\sigma}{2})\frac{\alpha_0}{\sigma}} & \text{for } x > \mu + \alpha_0\sigma \end{cases} \tag{4.1}$$

where N_{raw} is the number of signal counts, μ and σ are respectively the mean and the standard deviation of the gaussian and α_1 and α_0 are the number of σs from μ at which the function becomes an exponential, on the left and on the right side of the gaussian, respectively. Such a complex functional form is preferred to a simple gaussian function because, in case of distributions with a large number of counts as in the whole proton analysis, a

simple gaussian is not suitable in reproducing the exponential decrease of the distribution tails. Since the background coming from the contamination of other particle species is quite different depending on the transverse momentum region, two different functions have been used to parameterize it: a Gaussian function for $0.55 \leq p_{\mathrm{T}} < 0.60$ GeV/c and the sum of two Gaussian functions for $0.60 \leq p_{\mathrm{T}} < 1.00$ GeV/c. For $p_{\mathrm{T}} < 0.55$ GeV/c no background is present, so that a simple bin counting technique is adopted.
For higher transverse momentum values the TOF $n\sigma$ information is used. The $n\sigma$ distributions are described as the sum of a gaussian function with an exponential tail on the right, defined as

$$sig(x) \propto N_{raw} \begin{cases} e^{-\frac{1}{2}\left(\frac{x-\mu}{\sigma}\right)^2} & \text{for } x \leq \mu + \alpha\sigma \\ e^{-\alpha\left(\frac{x-\mu}{\sigma} - \frac{\alpha}{2}\right)} & \text{for } x > \mu + \alpha\sigma \end{cases} \tag{4.2}$$

where N_{raw}, μ and σ stand for the same quantities used for the TPC analysis, while α is the number of σs from μ on the right side of the gaussian at which the function becomes an exponential. Background is parameterized with different functions according to the p_{T} interval and the multiplicity class under study. As an example, for the multiplicity class X, at low p_{T} ($1.0 \leq p_{\mathrm{T}} < 1.7$ GeV/c) the background is described with a single exponential. The sum of an exponential and of either a single Gaussian function or two Gaussian functions are used in the $1.7 \leq p_{\mathrm{T}} < 2.5$ GeV/c or $2.5 \leq p_{\mathrm{T}} < 3.5$ GeV/c regions. An example of the signal extraction procedure is reported for different p_{T} intervals and multiplicity classes for TPC and TOF in Fig. 4.2 and in Fig. 4.3, respectively. The blue line represents the sum of signal and background extracted from the fit, while the green shaded area is the one obtained for signal. The azure and red functions are the background contributions of the fitting procedure. For this part of the analysis, the sum of matter and antimatter is considered.

4.5.2 Deuteron

The deuteron signal is extracted with the same strategy used for the proton one. The TPC nσ technique is exploited between 0.7 and 1.0 GeV/c, while in the region $1.0 \leq p_{\mathrm{T}} < 3.4$ GeV/c the TOF squared-mass information is used. The deuteron signal is parameterized as a gaussian with two exponential tails and with a gaussian with an exponential tail on the right for the TPC and TOF analyses, respectively. The main difference with respect to the proton signal extraction lays in the background estimation, since contamination from other particle species is rather different. In particular, for $p_{\mathrm{T}} \leq 1.6$ GeV/c no background is present, while in the rest of the transverse momentum region an exponential background due to misassociated TOF hits and other particles contamination is observed. The m^2 distributions are re-centered

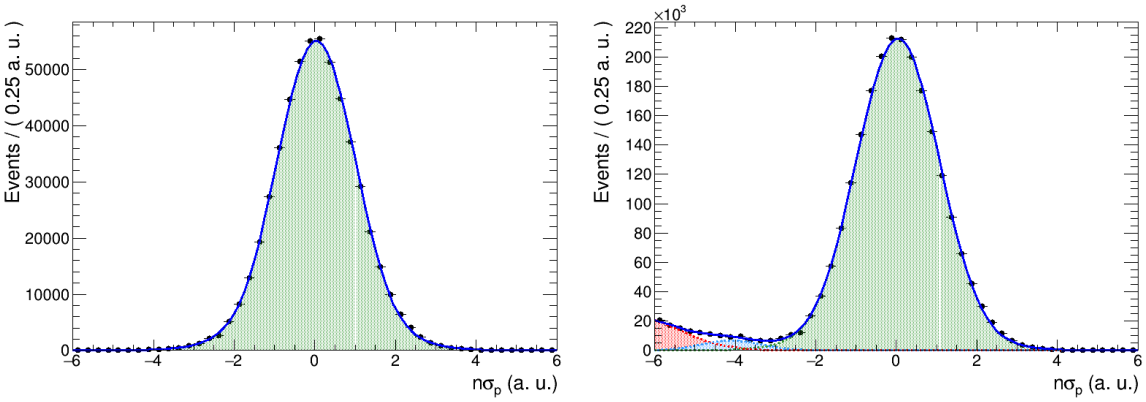

Fig. 4.2 Distribution of the TPC nσ variable in arbitrary units for the multiplicity class II in the regions 0.35 GeV/$c \leq p_{\mathrm{T}} <$ 0.40 GeV/c (left) and 0.60 GeV/$c \leq p_{\mathrm{T}} <$ 0.70 GeV/c (right). The green shaded area represents signal. If background is present, the red and blue ones represent the background component obtained through the fit procedure. The blue line is the sum of signal and background components.

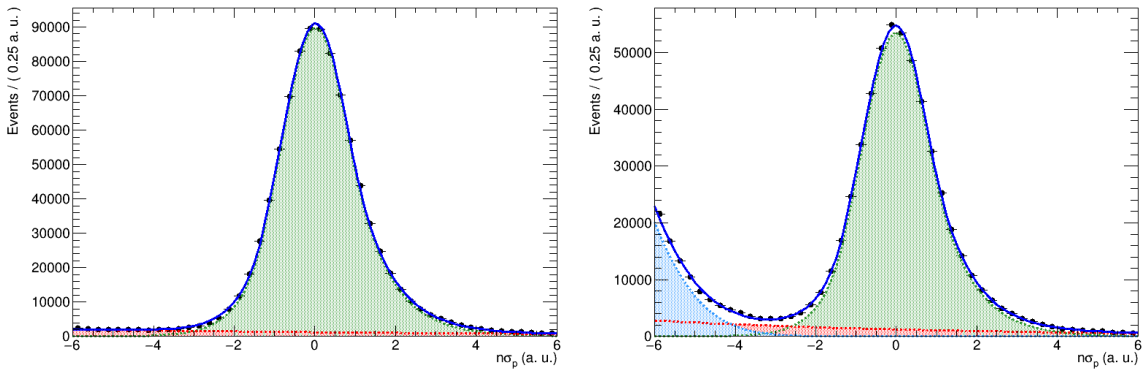

Fig. 4.3 Distribution of the TOF nσ variable in arbitrary units for the multiplicity class IV + V in the regions 1.7 GeV/$c \leq p_{\mathrm{T}} <$ 1.9 GeV/c (left) and 2.2 GeV/$c \leq p_{\mathrm{T}} <$ 2.5 GeV/c (right). The green shaded area represents signal. If background is present, the red and blue ones represent the background component obtained through the fit procedure. The blue line is the sum of signal and background components.

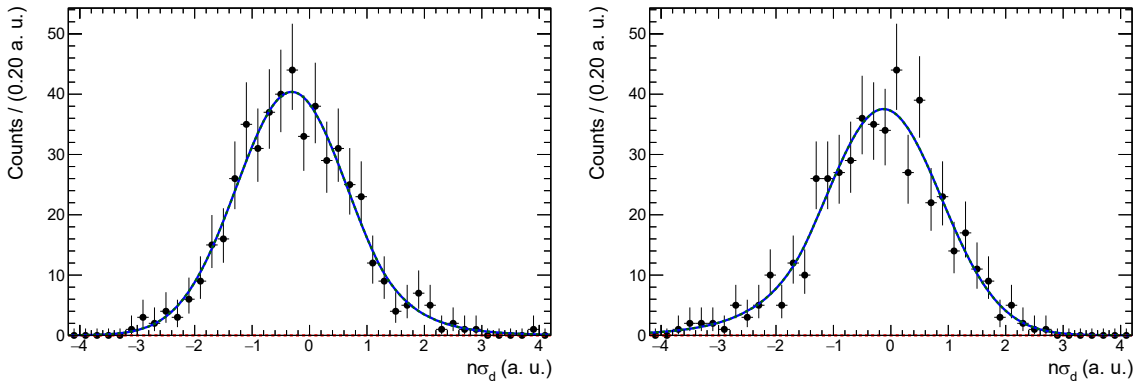

Fig. 4.4 Distribution of the TPC σ variable in arbitrary units for the multiplicity class I in the regions 0.7 GeV/$c \leq p_{\mathrm{T}} <$ 0.8 GeV/c (left) and 0.9 GeV/$c \leq p_{\mathrm{T}} <$ 1.0 GeV/c (right). The blue line represents the signal function obtained via the fit procedure.

by subtracting the deuteron PDG mass m_{d}^2 to the measured value: as observed in previous analyses [146], this distribution is shifted towards positive $m^2 - m_{\mathrm{d}}^2$, but this effect does not introduce any bias in the raw signal evaluation, which is based on an asymmetric bin counting procedure. Since the m^2 fit procedure leads to high χ^2 values and a systematic underestimation of the signal peak value when no background is present, the bin counting method is used for $1.0 \leq p_{\mathrm{T}} < 1.6$ GeV/c. Such technique consists in computing the integral of the signal in the range $[\mu - 3\sigma, \mu + 5\sigma]$, where μ and σ are the mean and standard deviation of the fit function used for the first step of the signal extraction. As can be noticed, the bin counting interval is asymmetric to take into account the exponential tail which characterizes the signal shape. An example of the deuteron signal extraction procedure is reported for multiplicity class I and two different p_{T} intervals for both TPC and TOF in Fig. 4.4 and Fig. 4.5, respectively. The blue line represents the sum of signal and background extracted from the fit, while the green and red dashed lines, when visible, are those describing signal and background separately. This part of the analysis is performed separating deuterons and antideuterons, while the final results are merged together in a later stage of the analysis, as it will be seen in the coming sections.

4.5.3 Helion

Helion production is strongly suppressed with respect to the proton and deuteron ones, due to its higher mass number. For this reason, the combination of both the TPC and TOF detectors would drastically reduce the amount of observed helions. Moreover, the TPC detector stand-alone is suitable enough to extract the helion signal over the whole transverse

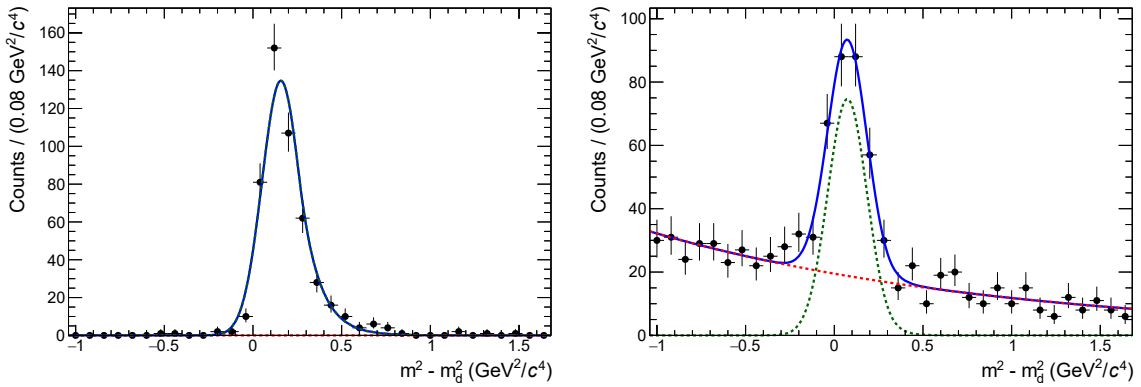

Fig. 4.5 Distribution of the measured TOF $m^2 - m_{\rm d}^2$ difference for the multiplicity class I in the regions 1.2 GeV/$c \leq p_{\rm T} <$ 1.4 GeV/c (left) and 2.2 GeV/$c \leq p_{\rm T} <$ 2.6 GeV/c (right). The blue line represents the sum of the signal (dashed green) and the background (dashed red) functions. As explained in the text, the background component is not present for $p_{\rm T} \leq$ 1.6 GeV/c.

momentum region of interest (0.9 $\leq p_{\rm T} <$ 4.2 GeV/c in the INEL $>$ 0 multiplicity class). In order to maximize the $p_{\rm T}$ reach of the analysis, the signal extraction is performed for the sum of matter and antimatter. A non negligible contamination due to tritons can not be completely separated by the TPC PID and is estimated through the fitting procedure. Due to the limited number of signal and background counts, each of them is parameterized by a gaussian function. Figure 4.6 shows an example of the fit to the nσ distributions for helions in the integrated multiplicity class for two different transverse momentum regions. As described above, green, red and blue lines represent the result of the fit performed to reproduce the signal, the background and their sum, respectively.

4.6 Corrections to the raw signal

In order to extract the $p_{\rm T}$-differential production spectra for nuclei it is necessary to apply some corrections to the results obtained at the signal extraction stage of the analysis. These corrections take into account the detector efficiency and acceptance, the contribution from secondary nuclei and the signal loss due to trigger inefficiencies, and are computed exploiting the MC productions described in Sec. 4.2.

Efficiency x Acceptance Among all the particles produced in an hadronic collision, only a fraction is detected by the experimental apparatus. The first reason for this is linked to the geometrical coverage of the active area of the detector (acceptance), which is not hermetic.

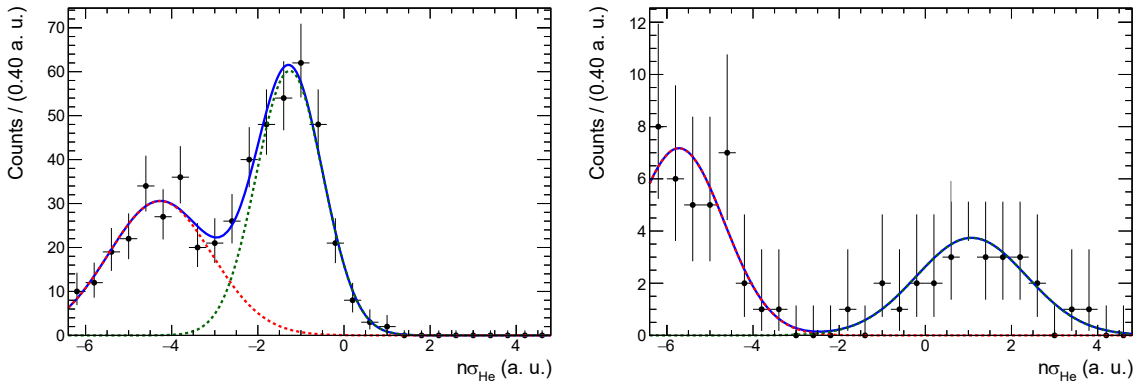

Fig. 4.6 Distribution of the TPC nσ variable in arbitrary units for the INEL > 0 multiplicity class in the regions 0.9 GeV/$c \leq p_{\mathrm{T}} <$ 1.3 GeV/c (left) and 2.1 GeV/$c \leq p_{\mathrm{T}} <$ 2.6 GeV/c (right). The blue line represents the sum of the signal (dashed green) and the background (dashed red) functions.

Moreover, particle detectors and the tracking algorithm itself are not fully efficient and some nuclei may be rejected by the selection criteria described in Sec. 4.4 (efficiency). Since in a MC production, which embeds the realistic data taking conditions period-by-period, the real number of particle generated in an event and crossing the detector is known, the efficiency and acceptance correction ($\varepsilon \times Acc$) can be calculated as

$$\varepsilon \times Acc\,(p_{\mathrm{T}}^{\mathrm{rec}}) = \frac{N_{\mathrm{rec}}\left(p_{\mathrm{T}}^{\mathrm{rec}}\right)(|\eta| < 0.8, |y| < 0.5)}{N_{\mathrm{gen}}\left(p_{\mathrm{T}}^{\mathrm{gen}}\right)(|y| < 0.5)} \tag{4.3}$$

where $p_{\mathrm{T}}^{\mathrm{gen}}$ and $p_{\mathrm{T}}^{\mathrm{rec}}$ are respectively the transverse momentum attributed to the particle by the event generator and the one reconstructed by the tracking algorithm; N_{gen} is the number of particles generated in the rapidity region $|y| < 0.5$ and in the azimuthal region $0 < \phi < 2\pi$ and N_{rec} is the number of reconstructed particles that pass all selections.. The correction as a function of p_{T} is reported for the integrated multiplicity class in Fig. 4.7, Fig. 4.8 and Fig. 4.9 for the proton, deuteron and helion analyses, respectively. Matter is reported in black, antimatter in red, and the sum of them in blue, whereas squares and circles represent the TPC and the TOF analyses. As for the signal extraction procedure, the correction is evaluated for the sum of matter and antimatter for protons and helions, while it is evaluated separately for deuterons and antideuterons. Since it is observed that the $\varepsilon \times Acc$ is compatible within the different multiplicity classes for deuterons and helions, the INEL > 0 efficiency and acceptance correction is used in order to have more statistical precision. On the contrary, significant differences between the integrated sample and multiplicity classes are observed for protons in the low-p_{T} ($p_{\mathrm{T}} \lesssim 0.6$ GeV/c) region. This effect, which amounts to 8% for multiplicity class I in the region 0.30 GeV/$c \leq p_{\mathrm{T}} <$ 0.35 GeV/c, is connected to a more

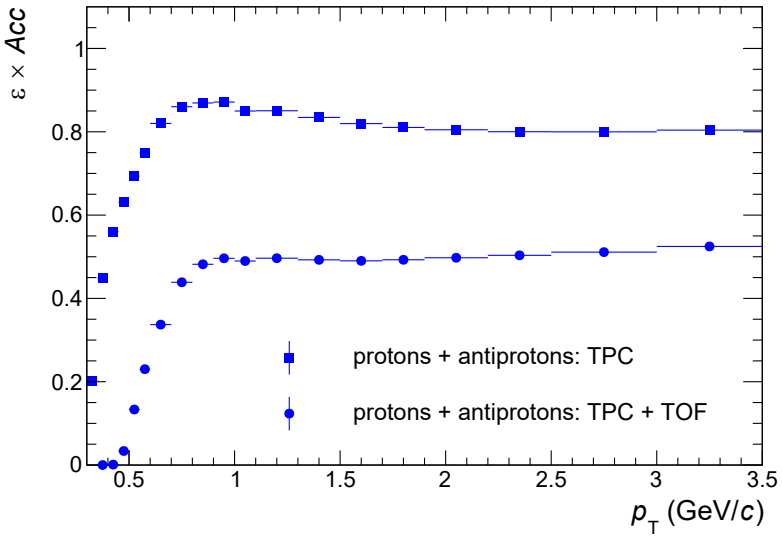

Fig. 4.7 Efficiency $\times$ acceptance correction of the sum of protons and antiprotons for the INEL > 0 multiplicity class as a function of transverse momentum for the TPC (squares) and the TOF (circles) analyses.

challenging reconstruction of low-p_{T} tracks as the number of charged particles per event increases. For this reason, the raw spectra of protons are corrected with the efficiency $\times$ acceptance evaluated in each multiplicity class. For both the TPC and TOF analyses, the efficiency $\times$ acceptance increases rapidly from low to intermediate p_{T}. This is mainly due to the reduced acceptance towards small p_{T} and in minor part to the energy loss and the multiple scattering of the particles within the detector material. For higher values of transverse momentum the energy loss becomes smaller and the efficiency $\times$ acceptance saturates for protons, while it decreases mildly for deuterons and helions. The described correction is then applied, for each different multiplicity class, dividing the raw extracted yields by the $\varepsilon \times Acc$ correction.

Secondary nuclei An important source of background is given by the contamination due to secondary nuclei. Since this work aims to compare with theoretical predictions describing the production of nuclei in the primary hadronic collision, this contribution must be rejected in order to avoid a bias in the measurement. Secondary nuclei are mainly produced via knock-out from the interactions of the primary particles, i.e. coming from the interaction point, with the material of the beam pipe and of the experimental apparatus. Due to baryonic quantum number conservation this effect is negligible for antimatter, while it has to be considered for matter. In particular, this mechanism is responsible for the production of a

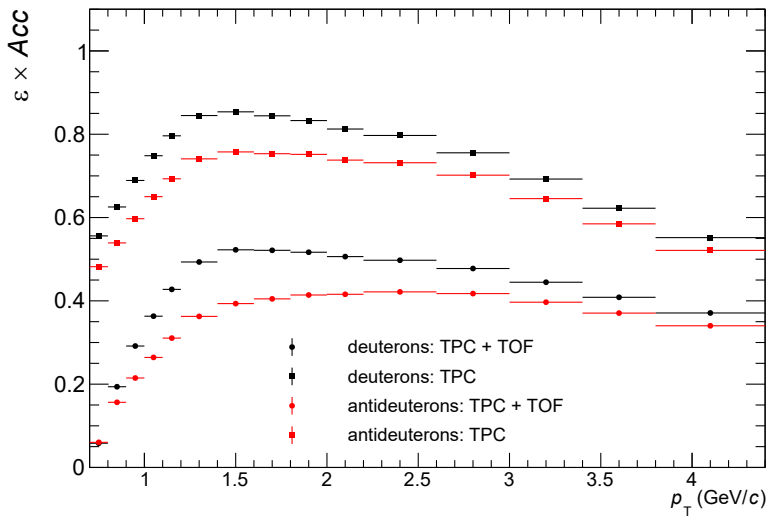

Fig. 4.8 Efficiency $\times$ acceptance correction of deuterons (black) and antideuterons (red) for the INEL > 0 multiplicity class as a function of transverse momentum for the TPC (squares) and the TOF (circles) analyses.

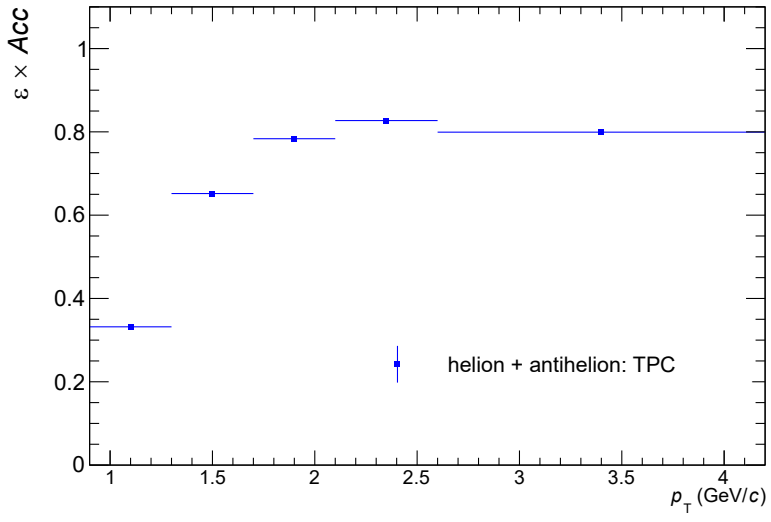

Fig. 4.9 Efficiency $\times$ acceptance correction of the sum of helions and antihelions (blue) for the INEL > 0 multiplicity class as a function of transverse momentum.

significant fraction of low transverse momentum nuclei, since in the knock-out interaction only a small fraction of the initial p_{T} is transferred to the secondary nucleus. Additionally, since many decays, such as the Λ baryon decay $\Lambda \rightarrow \mathrm{p} + \pi^{-}$, can yield to a proton in the final state, a considerable amount of secondary protons and antiprotons also comes from the weak decay of heavier particles. For deuterons and helions, this is a negligible contribution, since the only known possible process is the decay of hypertriton ($^{3}_{\Lambda}\mathrm{H} \rightarrow \mathrm{d} + \mathrm{p} + \pi^{-}$ and $^{3}\mathrm{H} \rightarrow ^{3}\mathrm{He} + \pi$), whose production is known to be severely suppressed in pp collisions [127]. The DCA information is used to estimate the correction for secondary nuclei. Primary particles, which directly come from the interaction point, are expected to have a sharply peaked distribution around $\mathrm{DCA_{xy}} = 0$ cm. On the other hand, secondary nuclei don't have a preferential flying direction, hence a flat $\mathrm{DCA_{xy}}$ distribution is expected. A fit to the $\mathrm{DCA_{xy}}$ distribution of data is performed using histogram templates for primary and secondary nuclei from MC, where the identity of primary and secondary particles is known. It is possible to evaluate the fraction of primary particles as

$$f_{\mathrm{prim}} = \frac{\mathrm{P}}{\mathrm{T}} \tag{4.4}$$

where P and T are respectively the integrals of the primary and total $\mathrm{DCA_{xy}}$ distributions after the template fit.

The template fit is performed using the ROOT TFractionFitter [147] (TFF) class, which is based on an algorithm which allows to fit experimental distributions using MC data samples, considering the statistical uncertainties of the MC histograms in the maximization of the likelihood. In particular, the mean value of the $\mathrm{DCA_{xy}}$ distribution inside each $\mathrm{DCA_{xy}}$ bin of the MC sample is considered as a fit parameter and therefore its value is modified during the fitting process. Examples of the fit procedure are shown in the left panels of Fig. 4.10, Fig. 4.11 and Fig. 4.12 for protons, deuterons and helions, respectively. As anticipated, the template for primary particles (blue) is peaked at $\mathrm{DCA_{xy}} = 0$, while the contribution from secondary nuclei (red) is spread out over the whole $\mathrm{DCA_{xy}}$ region. Nevertheless, a significant peak structure due to the incorrect association of secondary tracks to wrong SPD clusters, already observed in previous measurements [146] is present, in particular for protons and helions. For the proton analysis, the additional contribution from secondary protons from weak decays is reported in orange. The primary fractions as a function of p_{T} are finally fitted with the functional form

$$f_{\mathrm{prim}}\left(p_{\mathrm{T}}\right) = \frac{1}{1 - |a|\, e^{-|b| p_{\mathrm{T}}}} \,. \tag{4.5}$$

For each transverse momentum bin, the function value at the center of the bin is used to correct the raw counts. This is a useful strategy which can cope with non-physical fluctuations

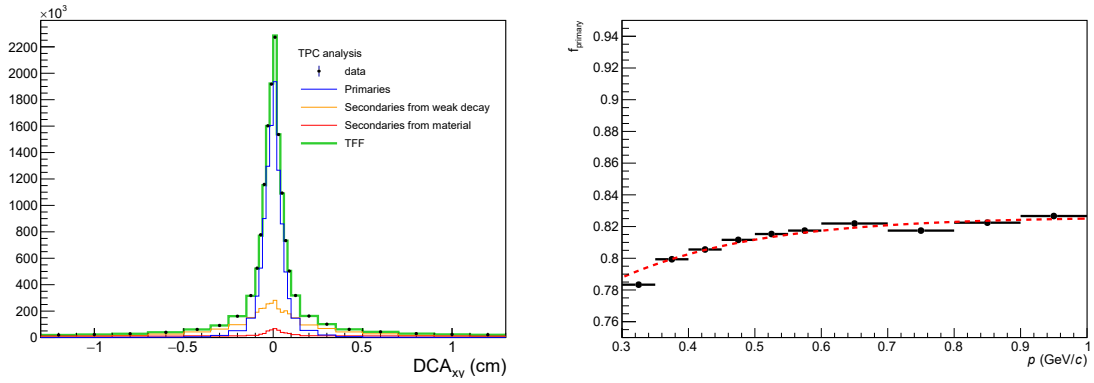

Fig. 4.10 Left: TFF fit result for the proton analysis in the region 0.30 GeV/$c \leq p_{\mathrm{T}} <$ 0.35 GeV/c for the multiplicity class III. The contributions from primaries, secondaries from weak decays and secondaries from material are reported in blue, orange and red, respectively. Right: exponential fit to the primary fractions of protons as a function of p_{T} for the multiplicity class III.

in the $\mathrm{DCA_{xy}}$ template fit and gives also an estimate at very high p_{T}, where the number of nuclei is so limited that it is not possible to perform the fits.
The correction, whose importance decreases with increasing transverse momentum, has larger impact on heavier nuclei. Depending on the analysis, it is evaluated either in the different multiplicity classes or in the integrated multiplicity class only. Where the number of nuclei allows the fit procedure to converge properly, such as in the proton and in the deuteron analyses, the multiplicity-differential strategy has been adopted, while in the case of the helion a integrated multiplicity strategy has been pursued. Moreover the MC production used does not provide secondary helions, so the templates are extracted from the proton sample at one third of the studied p_{T}. This procedure is based on the assumption that the templates of secondary helions are compatible with the ones of protons at a transverse momentum which is scaled with the rigidity p/z of helion, where z is the helion electric charge. The primary fraction correction as a function of the transverse momentum is reported, together with the fit function, in the right panels of Fig. 4.10, Fig. 4.11 and Fig. 4.12 for protons, deuterons and helions, respectively.

Signal and event loss Trigger inefficiencies may also introduce a bias in the evaluation of the nuclei spectral shape. In particular, all events wrongly rejected by the event selections lead to a loss in the count of nuclei produced in those events. For this reason it is necessary to estimate the true number of inelastic events instead of the number of accepted events. The

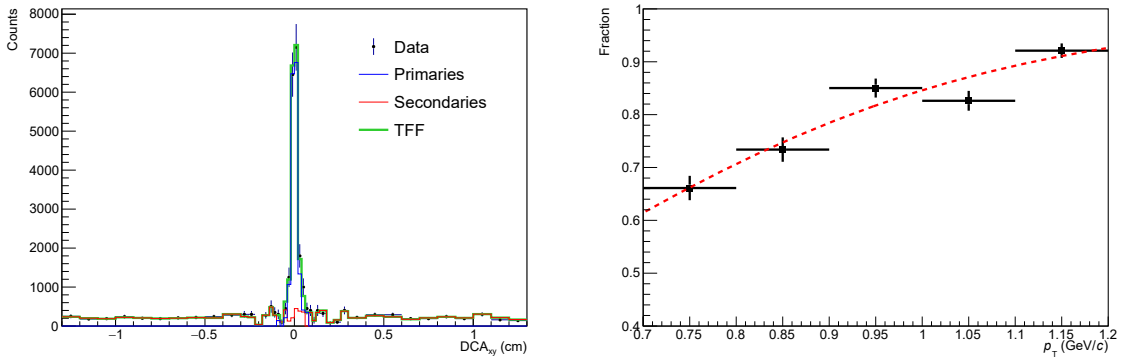

Fig. 4.11 Left: TFF fit result for the deuteron analysis in the region 0.9 GeV/$c \leq p_{\mathrm{T}} <$ 1.0 GeV/c for the multiplicity class I. The contributions from primaries and secondaries from material are reported in blue and red, respectively. Right: exponential fit to the primary fractions of deuterons as a function of p_{T} for the multiplicity class I.

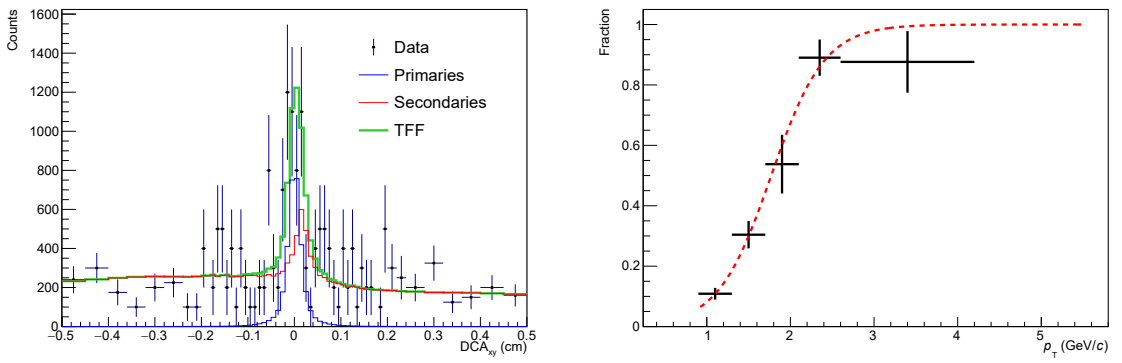

Fig. 4.12 Left: TFF fit result for the helion analysis in the region 1.3 GeV/$c \leq p_{\mathrm{T}} <$ 1.7 GeV/c for the INEL > 0 multiplicity class. The contributions from primaries and secondaries from material are reported in blue and red, respectively. Right: exponential fit to the primary fractions of helions as a function of p_{T} for the INEL > 0 multiplicity class.

number of true events is evaluated as

$$\frac{1}{N_{events}^{\text{true}}} \times \frac{\mathrm{d}^2 N_{\text{part}}^{\text{true}}}{\mathrm{d}p_{\mathrm{T}}\mathrm{d}y} = \frac{\varepsilon_{\text{events}}}{N_{\text{events}}^{\text{acc}}} \times \frac{\mathrm{d}^2 N_{\text{part}}^{\text{acc}}}{\mathrm{d}p_{\mathrm{T}}\mathrm{d}y} \times \frac{1}{\varepsilon_{\text{part}}(p_{\mathrm{T}})} \tag{4.6}$$

where $\varepsilon_{\text{events}} = N_{\text{events}}^{\text{acc}}/N_{\text{events}}$ is the fraction of accepted events after the event selection. N_{events} is the normalization factor accounting for the number of events and $\mathrm{d}^2 N_{\text{part}}^{\text{true}}/(\mathrm{d}p_{\mathrm{T}}\mathrm{d}y)$ is the MC production spectrum for the particle species under study. The fraction of signal loss ε_{part} is then evaluated as

$$\varepsilon_{\text{part}}(p_{\mathrm{T}}) = \frac{\dfrac{\mathrm{d}^2 N_{\text{part}}^{\text{gen}}}{\mathrm{d}p_{\mathrm{T}}\mathrm{d}y}(\text{acc})}{\dfrac{\mathrm{d}^2 N_{\text{part}}^{\text{gen}}}{\mathrm{d}p_{\mathrm{T}}\mathrm{d}y}(\text{true})} \tag{4.7}$$

where the events defined as acc are those events that passed the selections, while the true events are those events which have at least one primary charged particle in the pseudorapidity region $|\eta| < 1$ and the vertex in the region $|z_{\text{true}}| < 10$ cm (INEL > 0).
For protons, this correction is directly calculated from the MC sample used for the efficiency estimation. On the other hand, this study can not be carried out on the same injected production used for deuterons and helions, since the injection alters the signal loss fractions which need to be estimated. For this reason a general purpose MC production, which reproduces properly the charged-particle multiplicity measured in data, must be used. Since such simulation do not contain nuclei, the fraction of signal lost in the event selection is estimated for deuterons and helions as the average of the ones determined for pions, kaons and protons. This is done by exploiting the independence of the lost signal on the particle mass, which was observed in simulations [148]. The signal loss correction as a function of the transverse momentum is reported for the different multiplicity classes in Fig. 4.13, Fig. 4.14 and Fig. 4.15 for protons, deuterons and helions, respectively. A clear dependence on the average multiplicity of the class is observed for this correction: even if at high and mid multiplicity the signal loss fraction is negligible, it becomes more important going towards low multiplicities and for the INEL > 0 class. This effect, which at $p_{\mathrm{T}} \sim 1$ GeV/c accounts for $\approx 12\%$ for the multiplicity class X of protons and deuterons, is expected since at low multiplicity it is more likely that one event is rejected because there are no tracks in the pseudo-rapidity region $|\eta| < 1$.

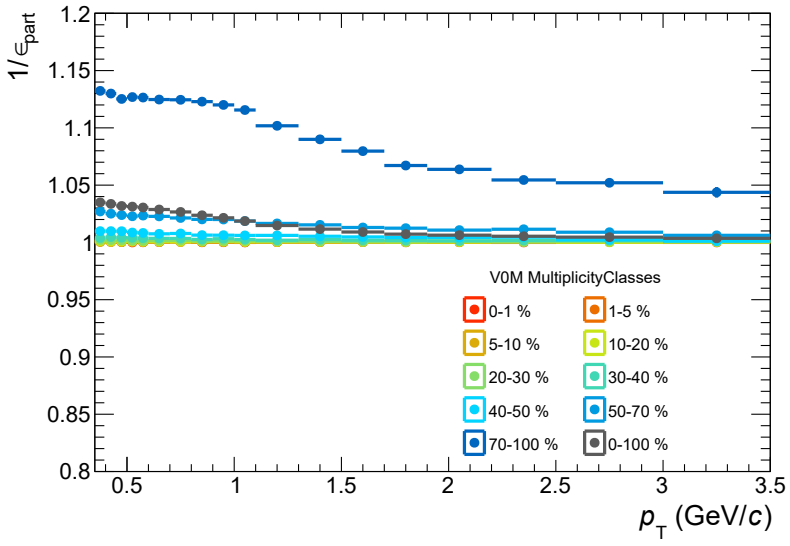

Fig. 4.13 Signal loss correction as a function of transverse momentum for the multiplicity classes used in the proton analysis.

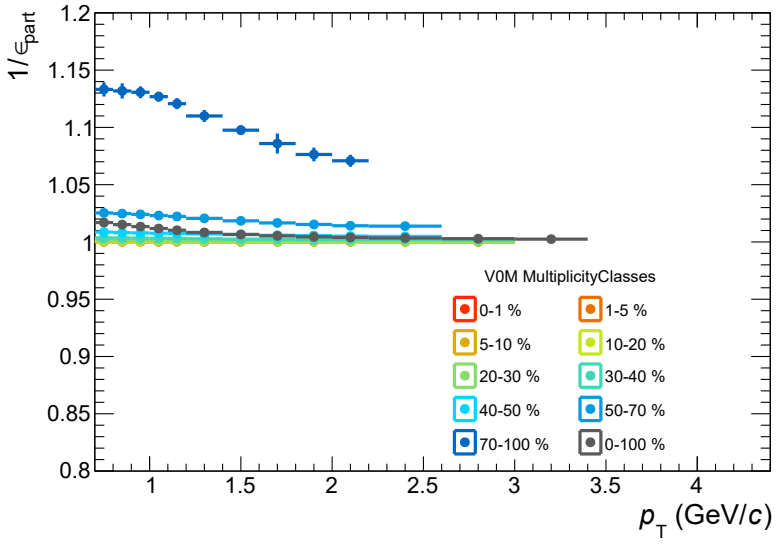

Fig. 4.14 Signal loss correction as a function of transverse momentum for the multiplicity classes used in the deuteron analysis.

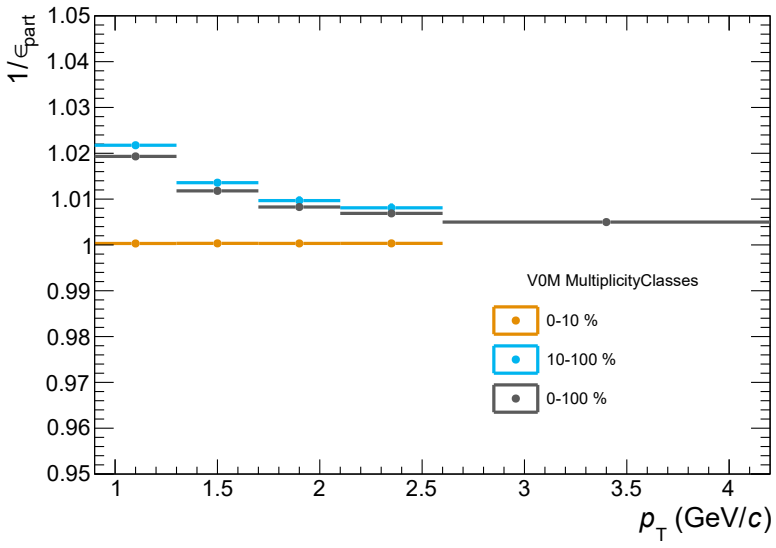

Fig. 4.15 Signal loss correction as a function of transverse momentum for the multiplicity classes used in the helion analysis.

4.7 Systematic uncertainties

In order to make a quantitative comparison between the nuclei yields determined in this work and the theoretical predictions, one has to evaluate the systematic uncertainties due to the analysis procedure described in the previous sections. For this reason, different sources of systematic uncertainties are evaluated by changing the analysis criteria and selections in each step. The sources of systematic uncertainties taken into account are: the track selections, the signal extraction methods, the different corrections to the raw signal and some additional contributions due to the MC description of the studied physical processes and of the ALICE apparatus. To evaluate the total systematic uncertainty, all the contributions are then summed in quadrature. In the following a detailed description of the systematic uncertainties evaluation is reported.

Track selection The results of the analysis can be slightly influenced by the criteria used for the selection of candidates, since the MC does not reproduce the data perfectly. This systematic uncertainty is evaluated performing the same analysis steps on data samples selected with different selection criteria. In particular, in order to test the effect of the track quality on the measurement, the number of required TPC clusters is varied between 60 and 80. Additionally, when the TOF PID is used, the pre-selection on the $n\sigma_{\mathrm{TPC}}$ is released up to $n\sigma_{\mathrm{TPC}} = 3.5$, lowering the purity of the TOF signal. All the selections used for this study are

Variable	Default value	Other values
TPC clusters	70	60, 65, 75, 80
TPC nσ	3	3.25, 3.5

Table 4.6 Summary of the track selection variations. The TPC nσ variation is used only for the TOF analysis, otherwise the default selection is not required.

listed in Table 4.6. The root mean square (RMS) of the raw yields for each specific selection is taken as the corresponding systematic uncertainty.

Signal extraction A variation with respect to the default signal extraction procedure can affect the analysis results as well. This contribution to the total systematic uncertainty is evaluated in two different ways: the bin counting method and a Toy Monte Carlo study.

Bin counting As described before, the signal extraction is performed by fitting the TPC or the TOF signal distributions. A second approach exploited is the bin counting method, which has been previously described and consists in the evaluation of the integral of the distribution in a reference range which contains the signal region. For those bins in which the background is not negligible, a fit in the regions far from the intervals where the bin counting is used is performed to compute background integral to be subtracted from the bin counting result. This approach is used to evaluate a systematic uncertainty for both the TPC and the TOF analyses, by widening and by shifting the default interval in which it is performed, or by comparing the result obtained via bin counting and fit parameters. Unfortunately this method is affected by a not negligible drawback: if the number of counted nuclei is not large enough, even a small variation in the counting process will produce an overestimated systematic uncertainty. For this reason the bin counting method is not applied to the helion analysis.

Toy Monte Carlo study If the number of identified nuclei is too limited to allow for the usage of the bin counting method (namely for the helion analysis), the signal extraction is tested by fitting pseudo-data distributions which are similar to the data ones. This approach is based on the ROOT class RooMCStudy from the RooFit toolkit [149], which has been developed to perform multiple cycles of event generation. Starting from a functional form and a distribution to be described, this class generates a user defined number of events, from the provided function, according to a multinomial distribution. Each event class has the same integral of the initial distribution. The obtained distribution is then fitted with the provided function. In order to perform a study on the systematic uncertainty related to the signal

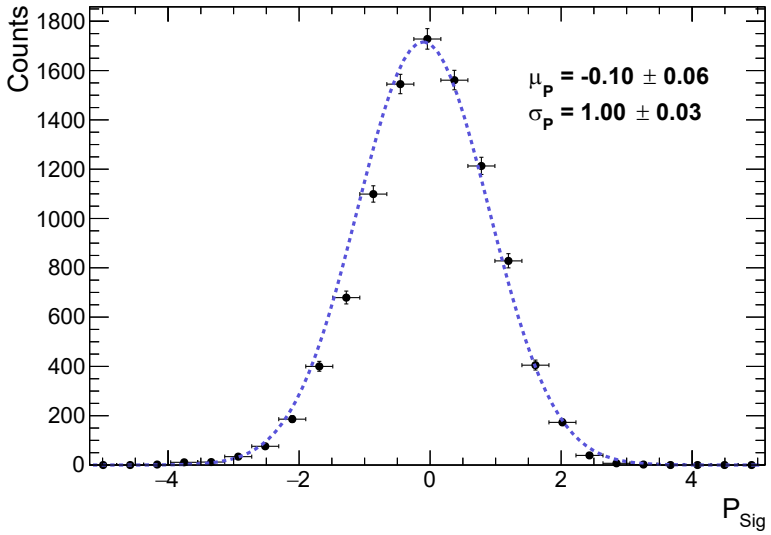

Fig. 4.16 Distribution of the pulls $P_{\rm sig}$ for the events generated by the toy MC for the helion analysis in the transverse momentum region 1.3 GeV/$c \leq p_{\rm T} <$ 1.7 GeV/c for the INEL > 0 multiplicity class.

extraction, the initial function and the distributions which are passed to the class are those used in the default signal extraction approach. For each event, the pull of the extracted signal $P_{\rm sig}$ is defined as

$$P_{\rm sig} = \frac{N_{\rm sig} - N_{\rm sig}^{\rm trial}}{\sigma_{N_{\rm sig}}} \tag{4.8}$$

where $N_{\rm sig}$ and $\sigma_{N_{\rm sig}}$ are the yield and its error determined at the signal extraction step. $N_{\rm sig}^{\rm trial}$ is the yield obtained at each event generation of the Toy MC study. An example pull distribution is reported in Fig. 4.16 for the INEL > 0 multiplicity class of the helion analysis. In principle, if no bias is introduced by the fitting procedure, a standard normal distribution, i.e. with mean value $\mu_{\rm P} = 0$ and standard deviation $\sigma_{\rm P} = 1$, would be expected. This hypothesis is tested by performing a gaussian fit to the pull distribution (dashed blue line), showing a deviation from $\mu_{\rm P} = 0$. In order to consider this effect, the systematic uncertainty is estimated as $\mu_{\rm P}$ times the statistical error.

Rejection of secondary nuclei As was observed in Sec. 4.6, the rejection of secondary nuclei is a fundamental step in the evaluation of the corrected nuclei yields. Among the track selections applied for the analysis, the $\rm DCA_{xy}$ and $\rm DCA_{z}$ selections are widely affecting the number of rejected secondary nuclei: as a term of comparison, the fraction of secondary deuterons measured in data in the transverse momentum region between 0.7 and 0.8 GeV/c for the INEL > 0 multiplicity class corresponds to 49.2 ± 0.4 and 29.9 ± 0.4 for the two extreme

Variable	Default value	Other values
DCA_{xy} (cm)	0.12	0.10, 0.14
DCA_z (cm)	1	0.5, 0.75, 1.5, 2

Table 4.7 Summary of the track selection variation for the evaluation of the systematic uncertainties related to the rejection of secondary deuterons.

selection $DCA_z = 1$ cm and $DCA_z = 2$ cm, respectively. For this reason this uncertainty is evaluated by performing the analysis on data samples with different selection criteria on the DCA which are listed in Table 4.7. Then the RMS of the raw yields for each specific selection is evaluated and the sum in quadrature of the results obtained for the DCA_z and the DCA_{xy} is taken as systematic uncertainty.

Material budget In the MC samples, a non optimal description of the material budget of the experimental apparatus would reflect into an incorrect determination of the efficiency $\times$ acceptance correction. Since the material budget does not depend on the collision system, the efficiency $\times$ acceptance is evaluated by using three MC productions where Pb–Pb collisions at $\sqrt{s_{\rm NN}} = 5.02$ TeV are simulated. One production assumes the standard material budget, taken as reference, and in the remaining two the standard value is increased and decreased by 4.5% respectively. For each transverse momentum value, the variation induced by the different material budget is supposed to follow a uniform distribution inside the maximum possible variation and therefore the corresponding systematic uncertainty $\sigma_{\rm Mat}(p_{\rm T})$ is described as

$$\sigma_{\rm Mat} = \frac{\varepsilon_{\rm max} - \varepsilon_{\rm min}}{\sqrt{12}} \tag{4.9}$$

where $\varepsilon_{\rm max}$ and $\varepsilon_{\rm min}$ are the maximum and the minimum efficiency $\times$ acceptance values, respectively, obtained for each transverse momentum interval.

Hadronic interaction The imperfect knowledge of the hadronic interaction cross section of nuclei with the material of the experiment contributes to the systematic uncertainty as well. The efficiency $\times$ acceptance correction relies on the momentum and mass number dependence of the measured cross sections parameterized in GEANT4 [86, 150] ($\sigma_{\rm G4}$). However the inelastic interaction cross sections of nuclei have been measured by several experiments [151–164] ($\sigma_{\rm exp}$) as a function of momentum on different materials. Since the GEANT4 parameterization does not describe perfectly the experimental measurements, an additional source of systematic uncertainty is considered in order to cope with these

discrepancies and it is evaluated as

$$\sigma_{\text{had}} = \frac{\Delta x}{\lambda_{\text{I}}} \frac{|\sigma_{\text{G4}} - \sigma_{\text{exp}}|}{\sigma_{\text{G4}}} \tag{4.10}$$

where Δx is the detector thickness and $\lambda_{\text{I}} = M/(\rho N_{\text{A}} \sigma_{\text{I}})$ is the hadronic interaction length, which depends on the properties of the detector material, i.e. the molar mass M, the density ρ, the Avogadro constant $N_{\text{A}} = 6.022 \cdot 10^{23}$ mol^{-1} and the true inelastic cross section σ_{I}. In this work, the systematic uncertainty values adopted to take into account the difference between the GEANT4 parameterization and the experimental measurements are those calculated for previous analyses performed in ALICE for the study of the nuclei production [165].

ITS-TPC matching efficiency The procedure of the track propagation from the TPC to the ITS affects the track reconstruction efficiency. It is necessary to account for this contribution as a source of systematic uncertainty. The matching efficiency between TPC and ITS tracks is defined as the fraction of tracks with clusters in both ITS and TPC ($N_{\text{ITS+TPC}}$) over the total number of tracks with clusters in TPC (N_{TPC}) and it is given by the formula

$$\varepsilon_{\text{ITS-TPC}} = \frac{N_{\text{ITS+TPC}}}{N_{\text{TPC}}} \ . \tag{4.11}$$

The systematic uncertainty is evaluated as

$$\sigma_{\text{ITS-TPC}} = \frac{\varepsilon_{\text{ITS-TPC}} - \varepsilon^{(\text{MC})}_{\text{ITS-TPC}}}{\varepsilon_{\text{ITS-TPC}}} \tag{4.12}$$

where $\varepsilon^{(\text{MC})}_{\text{ITS-TPC}}$ is the ITS-TPC matching efficiency computed for the MC simulation. This source of systematic uncertainty was suggested and provided by the ALICE Data Preparation Group which is in charge, within the ALICE Collaboration, for the calculation of this systematic effect for pp collisions at $\sqrt{s} = 5.02$ TeV recorded in the 2017 data taking.

Signal loss The signal loss correction described in Sec. 4.6 is also considered as a source of systematic uncertainty. Since this correction is based on an extrapolation assuming no dependence on the particle mass, a conservative approach is chosen to evaluate the systematic uncertainty: half of the signal loss correction is thus assigned as a contribution to the total systematic uncertainty. Even though a different calculation may be considered in order to reduce this source, it is worth to mention that this is a subdominant effect with respect to

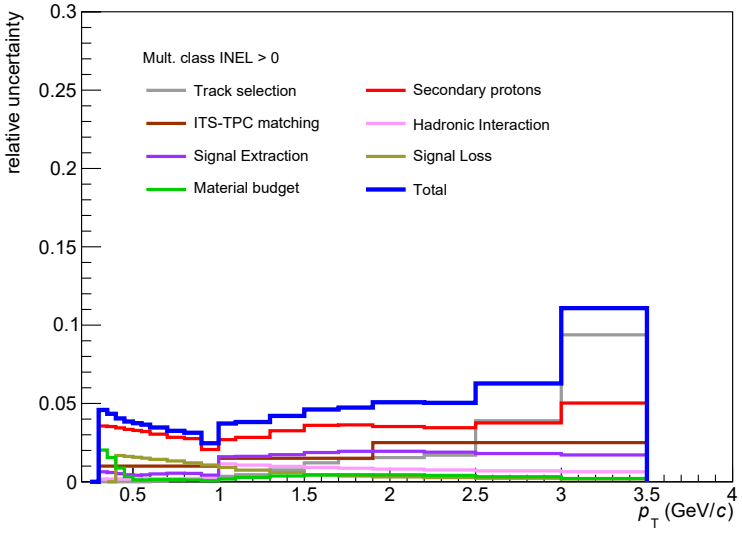

Fig. 4.17 Systematic uncertainty evaluated for the analysis of protons as a function of the transverse momentum for the INEL >0 multiplicity class. The blue thicker line is the total systematic uncertainty, while each single contribution is defined by a different color.

the total systematic uncertainty, except for the lowest multiplicity class of the proton and deuteron analyses, then it does not have a strong effect on the uncertainty on the final results.

4.7.1 Proton

In Fig. 4.17 the total systematic uncertainty as a function of the transverse momentum is reported for the analysis of the proton production for the integrated multiplicity class. For what concerns the contribution of the signal extraction to the total systematic uncertainty, the difference between the bin counting method and the result obtained via the fit parameters is used. As shown in the figure, the most relevant contribution to the systematic uncertainty is due to the rejection of secondary protons in the whole transverse momentum region covered in the analysis. At high p_{T} the track selection variations have a significant effect on the total systematic uncertainties, becoming dominant at very high transverse momentum. The total systematic uncertainty is always limited in the range between 2% and 12%.

4.7.2 Deuteron

Since the deuteron analysis is performed separately for matter and antimatter, it is possible to decouple the contributions for deuterons and antideuterons, whose systematic uncertainty for

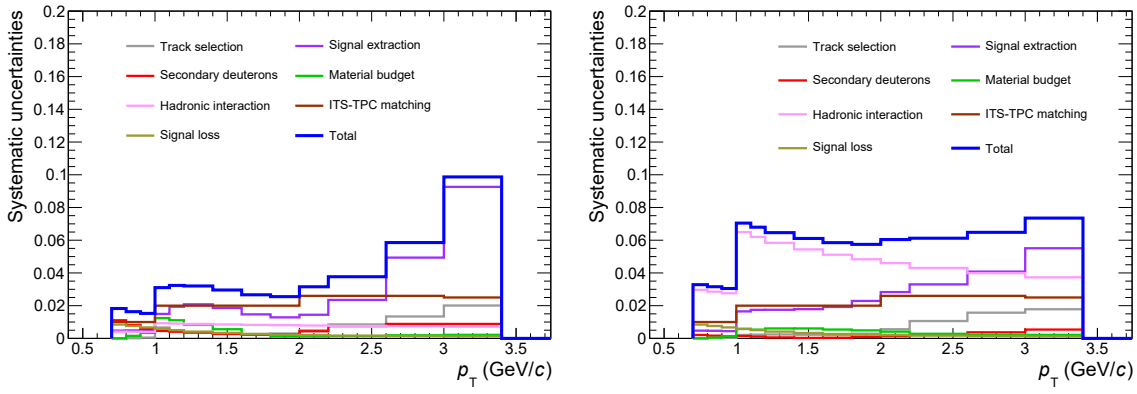

Fig. 4.18 Systematic uncertainty for the analysis of deuterons (left) and antideuterons (right) as a function of the transverse momentum for the INEL > 0 multiplicity class. The blue thicker line is the total systematic uncertainty, while each single contribution is defined by a different color.

the INEL > 0 class is reported in Fig. 4.18. For both matter (left) and antimatter (right) the total systematic uncertainty shows values similar to those evaluated for the proton analysis, even though each component has a different impact on the final value of the uncertainty in each p_{T} interval. In particular, the deuteron analysis does not have a dominant component at low p_{T}. Moreover, while for deuterons the hadronic interaction cross section is well known and constrained in GEANT4, this is not true for antideuterons. In the antimatter case the hadronic interaction is the dominant contribution in the whole transverse momentum range of the analysis, reaching 7% at most. In the case of the deuterons and antideuterons, the contribution of the signal extraction is evaluated by adopting the bin counting method. In particular a default bin counting range have been chosen to be $[\mu - 3\sigma, \mu + 3\sigma]$ for the TPC and $[\mu - 3\sigma, \mu + 5\sigma]$ for the TOF analyses, respectively, where μ and σ are the mean value and the standard deviation of the fit function used for the signal extraction. The selection interval for the TOF analysis is asymmetric to take into account the exponential tail which characterizes the signal shape, as was mentioned before. The default interval is varied by widening and shifting its limits according to the values reported in Table 4.8 for the TPC and the TOF analyses, respectively. The systematic uncertainty for range widening and shifting is computed as the RMS of the results obtained for the different variations of the default range. This two values are then summed in quadrature to obtain the systematic uncertainty related to the signal extraction. In Fig. 4.18 it is clearly visible that this contribution becomes dominant at very high p_{T}, since the number of nuclei is reduced and the bin counting is more sensible to instabilities in the fit of the background shape.

Analysis	Default Range	Variations
TPC	$[\mu-3\sigma, \mu+3\sigma]$	$[\mu-3\sigma-0.2$ a.u., $\mu+3\sigma+0.2$ a.u.$]$ $[\mu-3\sigma+0.2$ a.u., $\mu+3\sigma-0.2$ a.u.$]$ $[\mu-3\sigma-0.4$ a.u., $\mu+3\sigma+0.4$ a.u.$]$ $[\mu-3\sigma+0.4$ a.u., $\mu+3\sigma-0.4$ a.u.$]$
TOF	$[\mu-3\sigma, \mu+5\sigma]$	$[\mu-3\sigma-0.08$ GeV$^2c^{-4}$, $\mu+5\sigma+0.08$ GeV$^2c^{-4}]$ $[\mu-3\sigma+0.08$ GeV$^2c^{-4}$, $\mu+5\sigma-0.08$ GeV$^2c^{-4}]$ $[\mu-3\sigma-0.16$ GeV$^2c^{-4}$, $\mu+5\sigma+0.16$ GeV$^2c^{-4}]$ $[\mu-3\sigma+0.16$ GeV$^2c^{-4}$, $\mu+5\sigma-0.16$ GeV$^2c^{-4}]$

Table 4.8 List of bin counting intervals used to determine the systematic uncertainty related to the range widening, for the TPC and the TOF analyses.

Analysis	Default Range	Variations
TPC	$[\mu-3\sigma, \mu+3\sigma]$	$[\mu-3\sigma+0.2$ a.u., $\mu+3\sigma+0.2$ a.u.$]$ $[\mu-3\sigma-0.2$ a.u., $\mu+3\sigma-0.2$ a.u.$]$ $[\mu-3\sigma+0.4$ a.u., $\mu+3\sigma+0.4$ a.u.$]$ $[\mu-3\sigma-0.4$ a.u., $\mu+3\sigma-0.4$ a.u.$]$
TOF	$[\mu-3\sigma, \mu+5\sigma]$	$[\mu-3\sigma+0.08$ GeV$^2c^{-4}$, $\mu+5\sigma+0.08$ GeV$^2c^{-4}]$ $[\mu-3\sigma-0.08$ GeV$^2c^{-4}$, $\mu+5\sigma-0.08$ GeV$^2c^{-4}]$ $[\mu-3\sigma+0.16$ GeV$^2c^{-4}$, $\mu+5\sigma+0.16$ GeV$^2c^{-4}]$ $[\mu-3\sigma-0.16$ GeV$^2c^{-4}$, $\mu+5\sigma-0.16$ GeV$^2c^{-4}]$

Table 4.9 List of bin counting intervals used to determine the systematic uncertainty related to the range shifting, for the TPC and the TOF analyses.

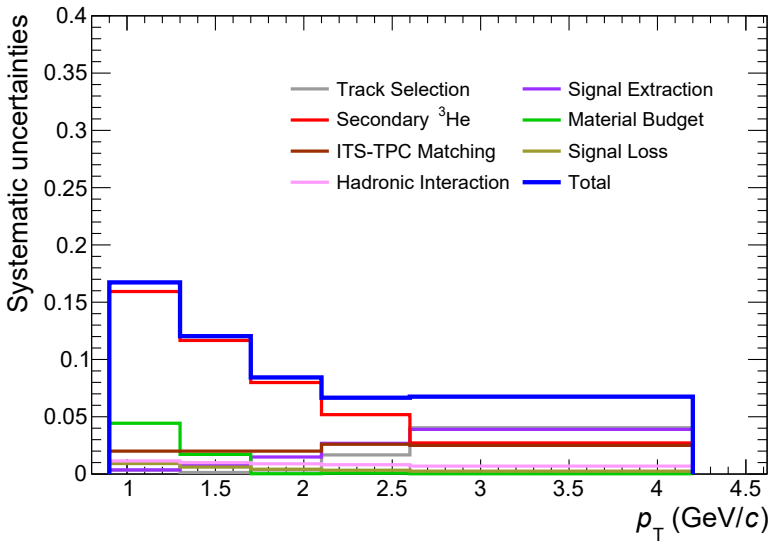

Fig. 4.19 Systematic uncertainty for the analysis of helion as a function of the transverse momentum for the INEL > 0 multiplicity class. The blue thicker line is the total systematic uncertainty, while each single contribution is defined by a different color.

4.7.3 Helion

The systematic uncertainty evaluated for the analysis of the helion is reported for the INEL $>$ 0 multiplicity class in Fig. 4.19. The source of systematic uncertainty coming from the signal extraction has been evaluated via the toy MC method, since the helion sample is too limited to allow for the bin counting approach. As a term of comparison, the raw signal for protons, deuterons and helions in the integrated multiplicity class and around $p_{\mathrm{T}} = 2.4$ GeV/c accounts for $2.4 \cdot 10^6$, $6.3 \cdot 10^3$ and 30 candidates, respectively. This approach led to a contribution which is negligible at low transverse momentum and increases at higher p_{T}. The overall systematic uncertainty is larger than those evaluated for the analyses of protons and deuterons and this is due to the fact that in the helion case the secondary correction is more important. At low transverse momentum this source is dominant and it reaches a value of 16% and decreases with increasing p_{T}. Thus the total systematic uncertainty for helions ranges between 8% and 17%.

4.8 Production spectra

Combining the information of the signal extraction and the corrections described in details in the previous sections, the production spectra of nuclei are evaluated as

$$\frac{1}{N}\frac{\mathrm{d}^2N}{\mathrm{d}p_{\mathrm{T}}\mathrm{d}y} = \frac{1}{N_{\mathrm{ev}}}\frac{\varepsilon_{\mathrm{ev}}}{\varepsilon_{\mathrm{part}}}\frac{f_{\mathrm{prim}}}{\varepsilon \times Acc}\frac{\mathrm{d}^2N_{\mathrm{raw}}}{\mathrm{d}p_{\mathrm{T}}\mathrm{d}y} \tag{4.13}$$

where $\frac{\mathrm{d}^2N_{\mathrm{raw}}}{\mathrm{d}p_{\mathrm{T}}\mathrm{d}y}$ is the raw signal per transverse momentum and rapidity unit, $\varepsilon \times Acc$ is the efficiency $\times$ acceptance correction and f_{prim} is the estimated fraction of primary nuclei. $\varepsilon_{\mathrm{ev}}$ and $\varepsilon_{\mathrm{part}}$ are the event and signal loss fractions, respectively. N_{ev} is the normalization factor on the number of events. In order to use the correct normalization, N_{ev} is defined as

$$N_{\mathrm{ev}} = \frac{N_{\mathrm{sel}} \cdot N_{|z|<10\mathrm{cm}}}{N_{\mathrm{vtx}}} \tag{4.14}$$

where N_{sel} is the number of events fulfilling the event selection criteria described in Sec. 4.3, excluding the vertex related selections. N_{vtx} is the number of accepted events which have a vertex determined either by SPD or by global tracking and $N_{|z|<10\mathrm{cm}}$ is the number of events that pass all the previous selections and have a reconstructed vertex in the region $|z| < 10$ cm. This choice for the normalization allows to consider the loss of inelastic events and therefore to normalize the production spectra by the real number of inelastic events.

Since for deuterons both the signal extraction and the evaluation of the corrections are performed separately for matter and antimatter, the resulting production spectra is computed as the weighted average of the deuteron and antideuteron spectra. The corrected production spectra of nuclei, reported in Fig. 4.20, are evaluated as a function of the transverse momentum and for each of the multiplicity classes listed in the first two columns of Table 4.11. In particular, for protons (left) and deuterons (center) it was possible to exploit nine multiplicity classes in addition to the integrated multiplicity one. Due to its lower production rate, the helion (right) was measured in two multiplicity classes only and in the INEL > 0 one. A fit (dashed and dash-dotted black lines) to the final spectrum was performed for each particle and multiplicity class to evaluate the integrated production yield and average transverse momentum of nuclei, as will be described in the next Section.

The procedure of computing the overall nuclei production spectra, without a separate study for matter and antimatter production, relies on the assumption that nuclei and antinuclei are equally produced at the LHC energies. In both the coalescence and the thermal model frameworks, if a condition of vanishing baryo-chemical potential is fulfilled, the ratio between

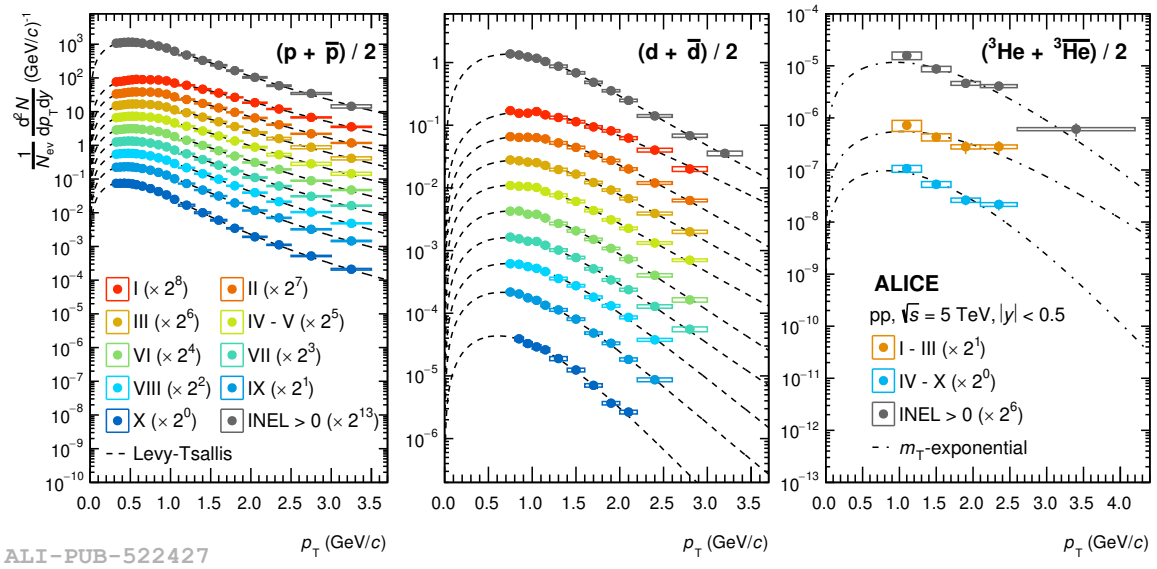

Fig. 4.20 Corrected p_{T} spectra for protons (left), deuterons (center) and helions (right), multiplied by a proper scale factor for better visualization. Each color corresponds to a different multiplicity class. The statistical uncertainties are represented by vertical bars while the systematic uncertainties are represented by boxes. The spectra have been fitted with Levy-Tsallis functions (dashed lines) for protons and deuterons, and with m_{T}-exponential functions (dashed-dotted).

antinuclei and nuclei abundances R is defined as

$$R = \left(\frac{\overline{p}}{p}\right)^{A} \tag{4.15}$$

where A is the number of constituent nucleons of the nucleus under study. p and $\overline{p}$ are the corrected yields for protons and antiprotons, respectively, whose ratio have been measured in pp collisions at different LHC energies [148, 166] and it was found to be compatible with the unity. For this reason this assumption was checked for the deuteron analysis, where the secondary correction is particularly challenging and could lead to some bias in the corrected spectra at low p_{T}, where such a correction is more relevant. The ratio between the antideuteron and deuteron spectra is reported in Fig. 4.21 for all the multiplicity classes of the analysis. In order to test the aforementioned assumption, the ratios are fitted with a constant function and the results are reported in Table 4.10. As expected from the models, the ratios are in agreement with the unity within their uncertainties for each multiplicity class, except for classes III and IX, where they are compatible within 2 sigmas.

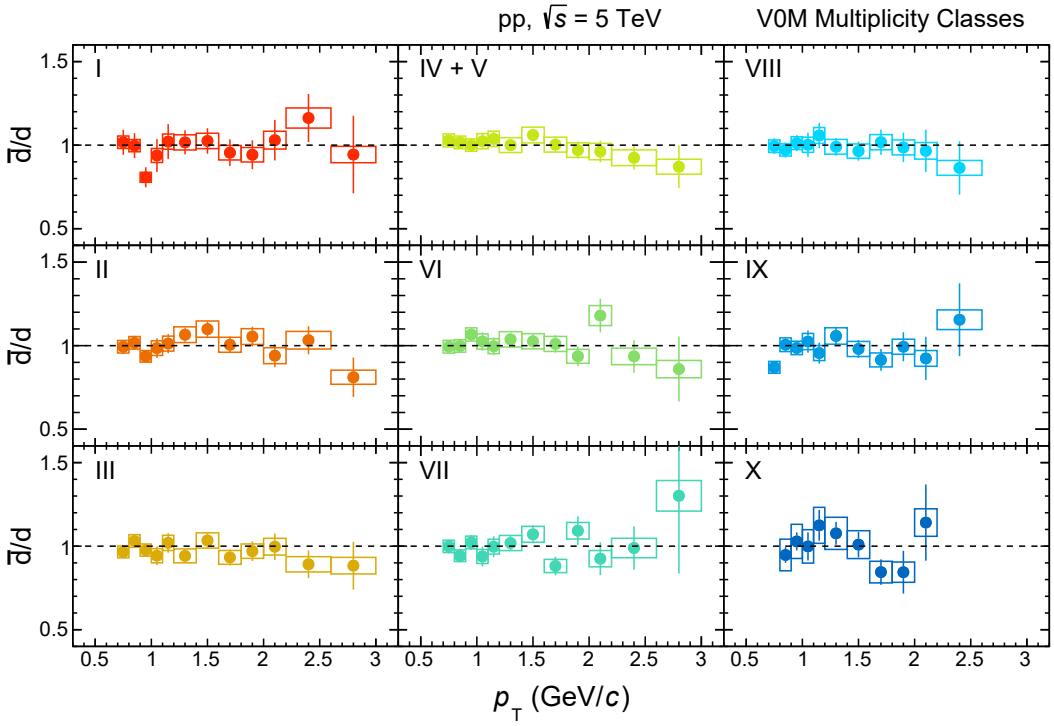

Fig. 4.21 Ratio between the antideuteron and deuteron spectra as a function of p_{T} for all the multiplicity classes of the analysis. The statistical uncertainties are represented by vertical bars while the systematic uncertainties are represented by boxes.

Class	Multiplicity	$\overline{\mathrm{d}}/\mathrm{d}$
I	$0-1\%$	0.97 ± 0.03
II	$1-5\%$	1.00 ± 0.02
III	$5-10\%$	0.97 ± 0.02
IV + V	$10-20\%$	1.01 ± 0.02
VI	$20-30\%$	1.01 ± 0.02
VII	$30-40\%$	0.99 ± 0.02
VIII	$40-50\%$	0.99 ± 0.02
IX	$50-70\%$	0.97 ± 0.02
X	$70-100\%$	0.98 ± 0.04
INEL >0	$0-100\%$	1.00 ± 0.01

Table 4.10 Result of the fit to the $\frac{\overline{\mathrm{d}}}{\mathrm{d}}$ ratio for each multiplicity class. The reported uncertainty is the one obtained from the fit procedure, which takes into account both the statistical and systematic uncertainties of each ratio.

4.9 Production yields and average transverse momenta

The production of nuclei in hadronic collisions can be studied via two key observables: the integrated production yields per rapidity unit $\frac{\mathrm{d}N}{\mathrm{d}y}$ and the average transverse momenta $\langle p_{\mathrm{T}} \rangle$. The aforementioned quantities are obtained by fitting the corrected spectra of nuclei. In pp collision, a good description of the production spectra is observed when using the Levy-Tsallis function

$$f(p_{\mathrm{T}}) = p_{\mathrm{T}} \frac{\mathrm{d}N}{\mathrm{d}y} \frac{(n-1)(n-2)}{nC[nC + m_0(n-2)]} \left[1 + \frac{(p_{\mathrm{T}}^2 + m_0^2)^{\frac{1}{2}} - m_0}{nC} \right]^{-n} \tag{4.16}$$

where m_0 is fixed to be the nucleus PDG mass. n, C and $\frac{\mathrm{d}N}{\mathrm{d}y}$ are free parameters and are evaluated in the fitting procedure. This parameterization is useful to extrapolate the p_{T} spectra in the unmeasured region, leading to the measurement of the integrated production yield and of the average transverse momentum $\langle p_{\mathrm{T}} \rangle$ of the produced nuclei. The contribution from the extrapolated region strongly depends on the considered particle species, since the p_{T}-coverage is generally different, and for the highest (lowest) multiplicity class it accounts for 10% (20%), 25% (55%) and 35% (40%) of the total yield for protons, deuterons and helions, respectively.
In order to consider the extrapolation procedure in the systematic uncertainties, the spectrum is fitted using two alternative functions:

1. a Boltzmann distribution
$$\frac{\mathrm{d}^2N}{\mathrm{d}p_{\mathrm{T}}\mathrm{d}y} = A p_{\mathrm{T}} m_{\mathrm{T}} e^{-\frac{m_{\mathrm{T}}}{T}} \tag{4.17}$$
2. an m_{T}-exponential function
$$\frac{\mathrm{d}^2N}{\mathrm{d}p_{\mathrm{T}}\mathrm{d}y} = A e^{-\frac{m_{\mathrm{T}}}{T}} \tag{4.18}$$

where A and T are fit parameters and $m_{\mathrm{T}} = (p_{\mathrm{T}}^2 + m_0^2)^{\frac{1}{2}}$ is the transverse mass of the particle of interest with PDG mass m_0. Half of the difference between the maximum and the minimum values of $\frac{\mathrm{d}N}{\mathrm{d}y}$ and $\langle p_{\mathrm{T}} \rangle$ computed with the fit functions described in Eq. 4.16, Eq. 4.17 and Eq. 4.18 is added in quadrature to the systematic uncertainty. For the helion spectra, the m_{T}-exponential function have been chosen as default function to grant more stability to the fit procedure, due to the limited number of transverse momentum bins. The production yields of nuclei in the multiplicity classes of the analysis are reported in Table 4.11. The largest part of the uncertainty on this measurement is due to systematic contribution, which accounts

for 6%, 7% and 13% for the highest multiplicity class of protons, deuterons and helions, respectively, while the statistical uncertainty is negligible for protons and limited to 2% for deuterons and 6% helions.

As was observed in the p–Pb analysis at $\sqrt{s_{\rm NN}} = 5.02$ TeV [128], the production yields follow an exponentially decreasing trend as a function of A. In order to perform the same study on the data sample used for this analysis, the multiplicity classes for both protons and deuterons were merged to match the helion ones, resulting in two wide multiplicity classes I – III and IV – X: the yields in these new multiplicity classes have been calculated as the average of the yields in the finer ones, weighted for the number of events in each parent multiplicity class. The integrated yields normalized for the spin degeneracy factor of nuclei $2J+1$ are shown in Fig. 4.22 for the I – III (left) and IV – X (right) multiplicity classes. The predictions for the proton yields from the Thermal-FIST package [113] are also reported (dashed green line): even though they are based on a default parameterization and not directly to a fit to the pp at $\sqrt{s} = 5.02$ TeV data, they can at least qualitatively describe the proton results. From the exponential fit (dashed black line) it is then possible to extract the penalty factor S, i.e. the suppression factor in the nuclei production when adding a nucleon to the nucleus. The values obtained in this work are $S = 805 \pm 58$ and $S = 1044 \pm 102$ for the I - III and IV - X multiplicity classes, hinting to an increasing suppression factor for decreasing multiplicity.

The average transverse momenta for the particle species analyzed in this work have been computed as a function of the charged particle multiplicity and they are shown in Fig. 4.23, together with a comparison to the measurements performed by the ALICE Collaboration in pp and p–Pb collisions at different collision energies. The results obtained in this work are in good agreement with those previously published for nuclei [165, 167, 168, 165, 34, 169, 170, 137, 171, 128]. As expected, the mean transverse momentum shows an increasing trend with the charged particle multiplicity which appears to be consistent across energies and collision systems. Moreover, as was previously observed for many light-flavored particle species [137, 172], a clear mass ordering is present.

4.10 Coalescence parameter $B_{\rm A}$

One of the possible mechanisms that brings to the production of light nuclei is the coalescence of protons and neutrons which are close in phase space, explained by the coalescence model described in Sec. 3.1.1. The key parameter of the model, the coalescence parameter $B_{\rm A}$, was measured in this work as a function of transverse momentum and multiplicity. The

Class	Multiplicity	dN/dy		
		p ($\times 10^{-1}$)	d ($\times 10^{-4}$)	^{3}He ($\times 10^{-7}$)
I	0 – 1%	$5.0 \pm 0.0 \pm 0.3$	$10.7 \pm 0.2 \pm 0.7$	
II	1 – 5%	$4.0 \pm 0.0 \pm 0.2$	$8.10 \pm 0.07 \pm 0.39$	
III	5 – 10%	$3.4 \pm 0.0 \pm 0.2$	$6.36 \pm 0.05 \pm 0.32$	
IV + V	10 – 20%	$2.8 \pm 0.0 \pm 0.2$	$4.92 \pm 0.03 \pm 0.24$	
VI	20 – 30%	$2.2 \pm 0.0 \pm 0.1$	$3.60 \pm 0.03 \pm 0.18$	
VII	30 – 40%	$1.8 \pm 0.0 \pm 0.1$	$2.65 \pm 0.03 \pm 0.14$	
VIII	40 – 50%	$1.5 \pm 0.0 \pm 0.1$	$1.98 \pm 0.02 \pm 0.09$	
IX	50 – 70%	$1.1 \pm 0.0 \pm 0.1$	$1.28 \pm 0.01 \pm 0.06$	
X	70 – 100%	$0.6 \pm 0.0 \pm 0.1$	$0.48 \pm 0.01 \pm 0.06$	
I – III	0 – 10%			$5.4 \pm 0.3 \pm 0.7$
IV – X	10 – 100%			$1.5 \pm 0.1 \pm 0.4$
INEL > 0	0 – 100%	$1.5 \pm 0.0 \pm 0.1$	$2.29 \pm 0.01 \pm 0.12$	$1.7 \pm 0.1 \pm 0.4$

Table 4.11 p_T integrated yields for the different species for each multiplicity class of the analysis. For protons, statistical uncertainties are negligible with respect to systematic uncertainties.

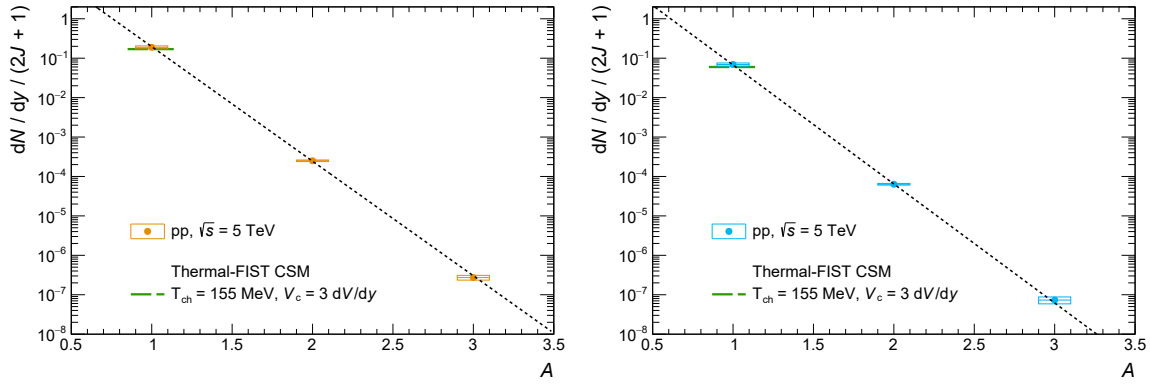

Fig. 4.22 Integrated yields of nuclei as a function of the mass number A evaluated in the I – III (left) and IV – X (right) multiplicity classes, together with the predictions from the Thermal-FIST CSM package (dashed green line). The results are fitted with an exponential function (dashed black line). The statistical uncertainties are represented by vertical bars while the systematic uncertainties are represented by boxes.

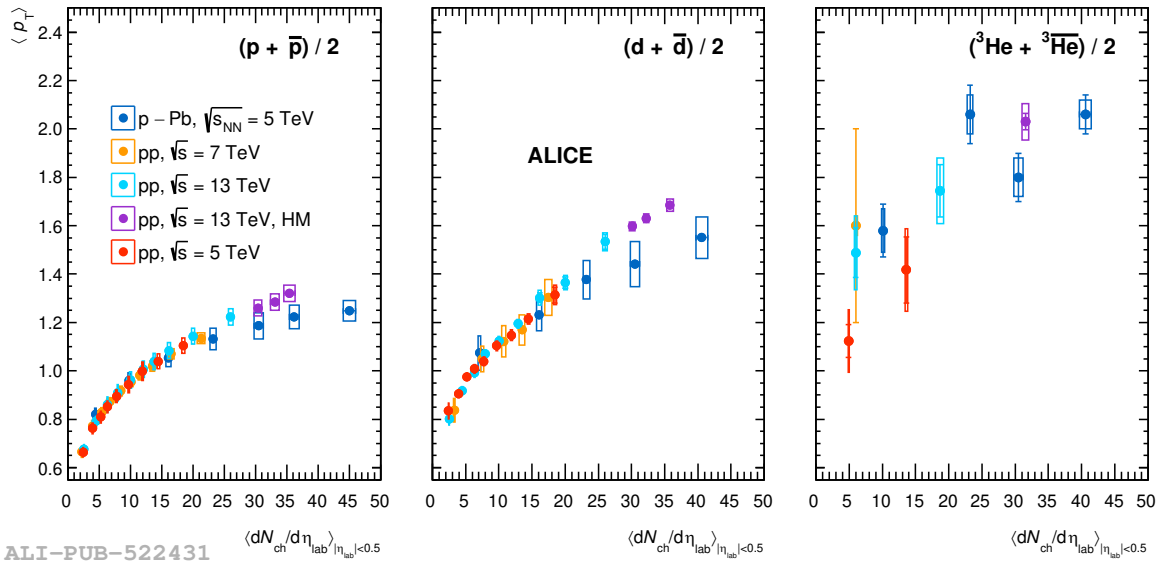

Fig. 4.23 Average transverse momenta for protons (left), deuterons (center) and helions (right). The values obtained in this work are reported in red. The results obtained in high-multiplicity pp collisions at $\sqrt{s} = 13$ TeV [165], in pp collisions at $\sqrt{s} = 13$ TeV [167, 168, 165] and at $\sqrt{s} = 7$ TeV [34, 169, 170], and in p–Pb collisions at $\sqrt{s_{\mathrm{NN}}} = 5.02$ TeV [137, 171, 128] are also shown for comparison. The statistical and systematic uncertainties are represented by vertical bars and by boxes, respectively.

coalescence parameter relates the production of light nuclei to that of its constituents and it is defined as

$$B_{\mathrm{A}} = \frac{\frac{1}{2\pi p_{\mathrm{T}}^{\mathrm{A}}} \frac{\mathrm{d}^2 N^{\mathrm{A}}}{\mathrm{d}y \mathrm{d}p_{\mathrm{T}}^{\mathrm{A}}}}{\left(\frac{1}{2\pi p_{\mathrm{T}}^{\mathrm{p}}} \frac{\mathrm{d}^2 N^{\mathrm{p}}}{\mathrm{d}y \mathrm{d}p_{\mathrm{T}}^{\mathrm{p}}}\right)^A} \tag{4.19}$$

with $p_{\mathrm{T}}^{\mathrm{p}} = p_{\mathrm{T}}^{\mathrm{A}}/A$, where p^{p} is the transverse momentum of the nucleons involved in the coalescence process and p^{A} is the transverse momentum of the resulting nucleus with mass number A. This formula is obtained by assuming equal transverse momentum spectra for neutrons and protons, since the former cannot be measured. The corrected spectra of protons, deuterons and helions, measured in this work and reported in Fig. 4.20, have been used to calculate the coalescence parameters B_2 and B_3.

The B_{A} is computed for deuterons and helions as a function of transverse momentum per nucleon p_{T}/A and it is reported in Fig. 4.24. The most simple coalescence models, which do not consider the spacial extension of nuclei, predict a flat coalescence parameter in all the multiplicity classes. A constant fit to the B_{A} has been tested: the flat hypothesis can not be rejected with a χ^2 test at a confidence level of 95%, even though a mild increasing trend may be present. Even if in multiplicity classes the coalescence parameter is compatible with a constant, in the integrated sample the increase of B_{A} with transverse momentum is significant. This behavior has already been observed in pp collisions at $\sqrt{s} = 13$ TeV [168] and it is caused by the hardening of the proton spectrum with increasing multiplicity, since this effect plays a role in the mathematical definition of B_{A}. Advanced implementations of the coalescence models [111] in which also the space-time distributions of nucleons is taken into account, could explain a mild raise in p_{T}.

In order to compare results obtained at different energies and in different collision systems it is useful to study the coalescence parameter as a function of charged particle multiplicity for a fixed value of p_{T}/A. The results of the present analysis are reported in red as a function of charged particle multiplicity in Fig. 4.25. The coalescence parameters B_2 and B_3 are shown for $p_{\mathrm{T}}/A = 0.75$ GeV/c and $p_{\mathrm{T}}/A = 0.78$ GeV/c for deuterons and helions, respectively. The values of p_{T}/A are the same used in previous ALICE analyses and this allows a direct and meaningful comparison with the existing measurements. The large number of multiplicity classes exploited in this work, especially for deuterons, allows to describe with unprecedented precision the low multiplicity region. Moreover a significant reduction of uncertainties is achieved with respect to the previous results due to the new techniques used to parameterize the hadronic cross sections of nuclei, described in Sec. 4.7. From the comparison between the pp and p–Pb collision systems one can conclude that the measurements are in agreement and a smooth trend from low up to high multiplicity is observed, without any dependence on

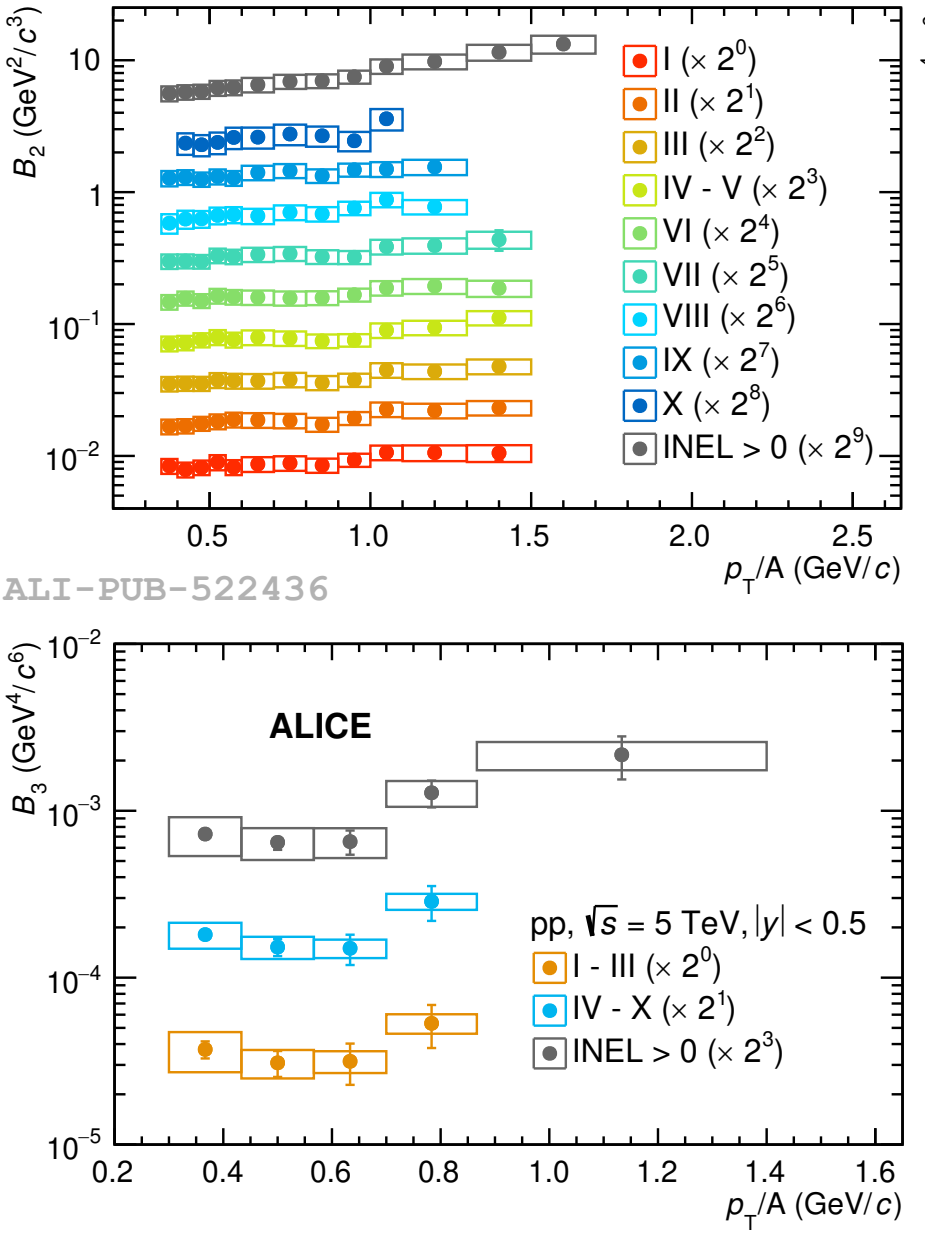

Fig. 4.24 Coalescence parameter B_2 (top) and B_3 (bottom) as a function of transverse momentum per nucleon for each multiplicity class. The statistical uncertainties are represented by vertical bars while the systematic uncertainties are represented by boxes.

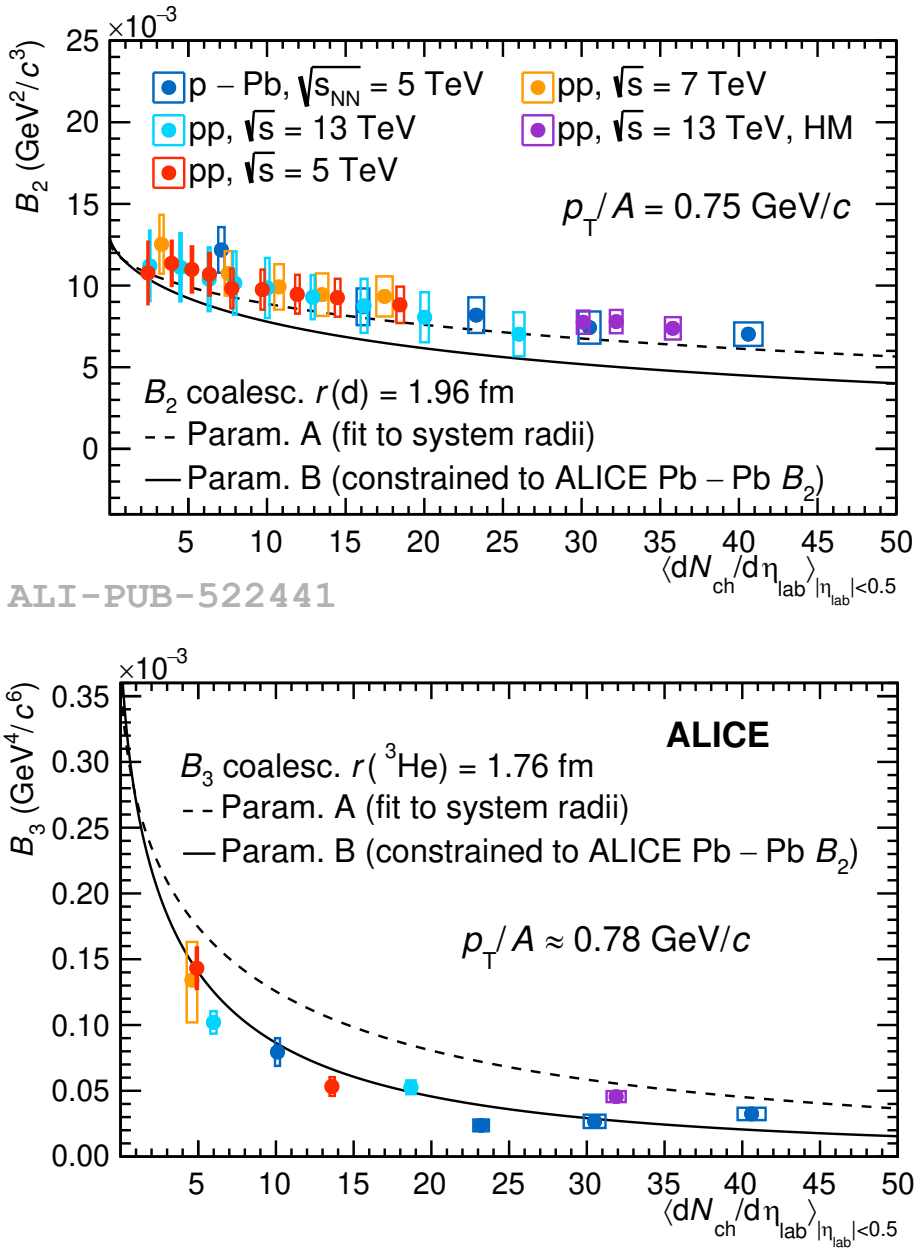

Fig. 4.25 B_2 (top) and B_3 (bottom) as a function of the multiplicity in this work (red), in high-multiplicity pp collisions at $\sqrt{s} = 13$ TeV [165], in pp collisions at $\sqrt{s} = 13$ TeV [168] and at $\sqrt{s} = 7$ TeV [169], and in p–Pb collisions at $\sqrt{s_{\rm NN}} = 5.02$ TeV [171]. The statistical uncertainties are represented by vertical bars while the systematic uncertainties are represented by boxes. The two lines are theoretical predictions of the coalescence model based on two different parameterization of the system radius as a function of multiplicity.

the collision system or energy.
Since it was observed [110] that the charged particle multiplicity can be directly related to the system radius through the relation

$$R = a\langle\frac{\mathrm{d}N_{\mathrm{ch}}}{\mathrm{d}\eta_{\mathrm{lab}}}\rangle^{1/3} + b \tag{4.20}$$

this behavior can be interpreted as a hint of a common production mechanism that depends only on the system size. This relation yields to slightly different predictions depending on the values of the a and b parameters. Two alternative parameterizations have been proposed [110]. As shown in Fig. 4.25, B_2 is better described with a first parameterization (dashed black line) obtained via fits to the system radii from two particle correlation measurements [129, 173, 174], while B_3 is in agreement with another parameterization (continuous black line) constrained to the ALICE B_2 result in Pb–Pb analysis [125, 124]. In general, none of the two parameterizations can simultaneously describe quantitatively both the B_2 and the B_3 results. Despite of the values used for the a and b parameters, at low charged-particle multiplicity the system size is comparable with the size of the nucleus, which is of the order of few fm, and a slow decrease with multiplicity is observed. On the contrary, if multiplicity increases, the system size becomes larger than the nucleus size, making the coalescence process less and less probable. In conclusion, the trend of B_{A} as a function of multiplicity can be qualitatively explained by a coalescence model that takes into account the finite size of nuclei, but new measurements of the nuclei radii as a function of multiplicity are needed in the attempt to have a comprehensive and quantitative description of the coalescence parameters of different nuclear species at the same time.

4.11 Ratio to proton yields

Another relevant observable to test the theoretical models is the ratio between the integrated yields of nuclei and protons. The deuteron over proton (d/p) and the helion over proton (^{3}He/p) yield ratios as a function of multiplicity are reported in Fig. 4.26 for all the measurements performed by the ALICE experiment in pp and p–Pb collisions, together with the predictions from both the coalescence and the SHM models. In particular, the two black lines are the theoretical predictions of the Thermal-FIST statistical model [122] for two different sizes of the correlation volume, $V_{\mathrm{c}} = 3\ \mathrm{d}V/\mathrm{d}y$ (dashed) and $V_{\mathrm{c}} = 1\ \mathrm{d}V/\mathrm{d}y$ (continuous). For deuterons, the green band represents the expectation from a coalescence model [111]. For helion, the green and blue lines represent the expectations from two-body and three-body

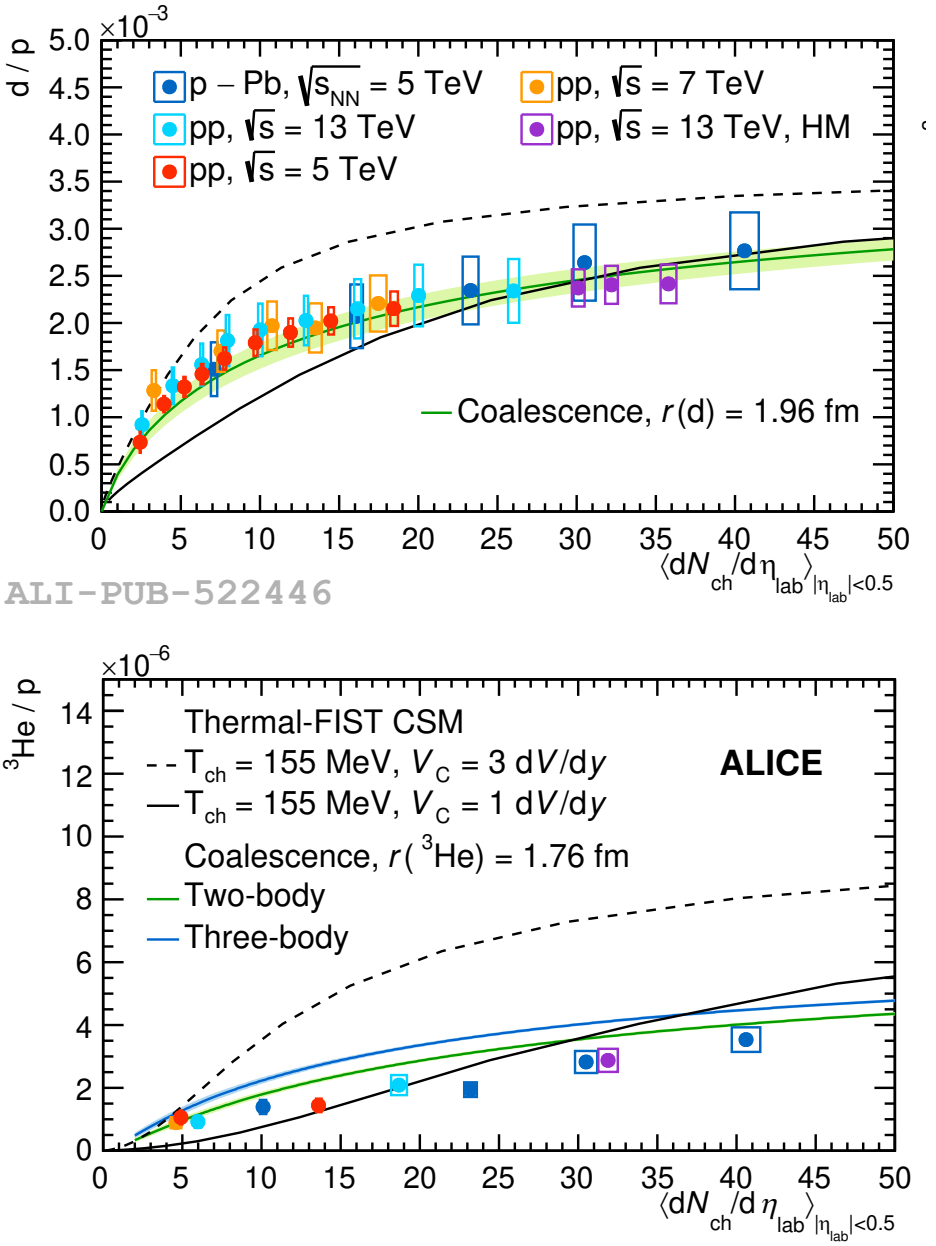

Fig. 4.26 Ratio between the p_{T}-integrated yields of nuclei and protons as a function of multiplicity for deuterons (top) and helions (bottom). Measurements obtained in this work (red) are compared to high-multiplicity pp collisions at $\sqrt{s} = 13$ TeV [165], pp collisions at $\sqrt{s} = 13$ TeV [168, 165] and at $\sqrt{s} = 7$ TeV [170], and p–Pb collisions at $\sqrt{s_{\mathrm{NN}}} = 5.02$ TeV [171, 128]. The statistical uncertainties are represented by vertical bars while the systematic uncertainties are represented by boxes. The two black lines are the theoretical predictions of the Thermal-FIST statistical model [122] for two sizes of the correlation volume V_{c}. For deuterons, the green band represents the expectation from a coalescence model [111]. For helion, the green and blue lines represent the expectations from a two-body and three-body coalescence models [111].

coalescence models [111].

As observed for the $B_{\rm A}$ measurement, a reduction of uncertainties up to a factor 2 is achieved in this work if compared to previous analyses. For the d/p ratio this leads to a clear agreement with the predictions from a coalescence models, while no parameterization of the SHM can describe the data over the whole multiplicity region of the analysis. The new measurement shows an excellent agreement with the data collected both in pp collisions at $\sqrt{s} = 7$ TeV and $\sqrt{s} = 13$ TeV and in p–Pb collisions at $\sqrt{s_{\rm NN}} = 5.02$ TeV. The same consideration holds for the ^{3}He/p ratio, even if neither a coalescence, nor a SHM model can describe quantitatively the reported results. Similarly to the coalescence parameter measurement, the yield ratios of nuclei as a function of multiplicity show a smooth trend going from low multiplicity pp collisions to the p–Pb multiplicity values. This is an additional observation which favors the idea of a single production mechanism for nuclei depending only on the system size.

Chapter 5

Multi-strange hadrons production in Pb–Pb collisions at 5 TeV

The second part of the thesis work is devoted to the measurement of the production rate of multi-strange particles. In particular, the measurement of Ξ and Ω baryons, together with their antiparticles, will be discussed and a description of the data samples and techniques exploited and of the results obtained within this thesis project will be given. In the following, these particles will be referred to as cascades, due to the peculiar decay topology which will be described in Sec. 5.4.

5.1 Analysis strategy

The analysis of multi-strange particles is conceptually similar to the nuclei measurement described in Chapter 4, with some relevant differences due to the physical processes involved. After a preliminary rejection of bad quality events, Ξ and Ω baryons must undergo a reconstruction process: since these particles are weakly decaying objects, they must be reconstructed backwards starting from the measured properties of their decay products, which are detected by the experimental apparatus. After this stage, the signal can be extracted and corrected for the efficiency and acceptance of the detector. The production yields are obtained from the corrected spectra and compared to the published ALICE measurements. Finally, the ratio between cascade and pion yields is evaluated in order to test the strangeness enhancement effect described in Sec. 1.4.1 as a function of charged particle multiplicity.

Purpose	n. of Events	Event Generator	Transport Code	Injection
Anchor period: 2018				
Eff x Acc	$9.53 \cdot 10^6$	HIJING	GEANT3	-
Eff x Acc	$1.86 \cdot 10^7$	HIJING	GEANT3	(A)
Eff x Acc	$1.01 \cdot 10^7$	HIJING	GEANT4	(B)
Anchor period: 2015				
Eff x Acc	$9.55 \cdot 10^6$	HIJING	GEANT3	-
Eff x Acc	$1.41 \cdot 10^7$	HIJING	GEANT3	(C)
Material Budget	$1.13 \cdot 10^7$	HIJING	GEANT3	(D)
Material Budget	$6.50 \cdot 10^6$	HIJING	GEANT3	(E)

Table 5.1 Overview of the MC samples used in the analysis of multi-strange baryon production. The different injection schemes, if present, are labeled with letter and explained in details in Table 5.2

5.2 Data and Monte Carlo samples

This analysis exploits the whole Pb–Pb data sample collected by the ALICE experiment during Run2. In particular two separate data taking periods were devoted to Pb–Pb collisions at $\sqrt{s_{\rm NN}} = 5.02$ TeV in 2015 and 2018. The 2015 data sample consists of nearly $1.2{\cdot}10^8$ events collected with a minimum bias (MB) trigger, while in 2018 two additional triggers, called Central and SemiCentral, have been exploited on top of the usual minimum bias one. Such additional triggers were developed by tuning the thresholds of the V0 detector signal amplitude in order to collect additional events in the 0–10% and 30–50% centrality intervals. The overall sample of events collected in 2018 consists of the sum of $1.2{\cdot}10^8$ MB collisions, $8.6{\cdot}10^7$ Central events and $5.9{\cdot}10^7$ SemiCentral ones. The thesis work exploits both of the two data taking periods by analyzing the whole data samples, in order to collect the largest number of Pb–Pb events ever studied in an analysis of multi-strange baryons production.
The MC simulations used in this analysis are reported in Table 5.1. Two different general purpose simulations were produced in order to map in statistics the data taking conditions of the two periods under investigation. These MC productions are exploited to evaluate the efficiency times acceptance correction. Since the production yields of cascades are too small to have a large enough sample to evaluate efficiencies with small statistical uncertainties, additional injected MC productions characterized by a flat $p_{\rm T}$ injection were requested. The injection scheme was chosen depending on centrality and transverse momentum range, and is reported in Table 5.2. Finally, two MC productions with augmented and decreased detector material budget were exploited to study its effect on the final results.

Species	Injection	p_{T} Range (GeV/c)	Centrality (%)	n. of Injected Particles
Ξ	(A)	[0.5; 12.0]	0 – 10	60
			10 – 30	20
			30 – 50	6
			50 – 90	2
	(B)	[0.5; 5.0]	0 – 10	50
			10 – 30	32
			30 – 50	8
			50 – 90	1
	(C)	[0.0; 24.0]	0 – 10	40
			10 – 50	16
			50 – 90	2
	(D)	[0.0; 12.0]	50 – 90	1
	(E)	[0.0; 3.0]	50 – 90	10
Ω	(A)	[0.5; 10.0]	0 – 10	60
			10 – 30	20
			30 – 50	6
			50 – 90	2
	(B)	[0.5; 4.5]	0 – 10	50
			10 – 30	24
			30 – 50	8
			50 – 90	1
	(C)	[0.0; 10.0]	0 – 10	17
			10 – 50	4
			50 – 90	1
	(D)	[0.0; 10.0]	50 – 90	1
	(E)	[0.0; 3.0]	50 – 90	10

Table 5.2 Injection scheme of the injected MC samples used for the cascade analysis. The number of injected particles refers to the sum of matter and antimatter particles per event.

Event Selections
Trigger selection
$\lvert v_z \rvert \leq 10$ cm
$\left\lvert v_z^{(\mathrm{SPD})} - v_z^{(\mathrm{TRK})} \right\rvert \leq 0.2$ cm
Pile-up rejection

Table 5.3 List of event selection criteria.

5.3 Event selection

Conceptually similarly to what discussed for the nuclei analysis, offline event selections are implemented for the strangeness analysis in order to filter out bad quality events. The full list of offline event selections is summarized in Table 5.3. By default, all the events characterized by an incomplete data acquisition, i.e. missing relevant information about the detectors exploited in this analysis, are rejected. Then, all the events which are not associated to the triggers used for this analysis, namely MB, Central and SemiCentral, are rejected. The primary vertex reconstruction is also tested: events are accepted if the vertex position is reconstructed in the fiducial z-region ± 10 cm around the collision point and if the estimates provided by the SPD detector ($v_z^{(\mathrm{SPD})}$) and by the full tracking procedure ($v_z^{(\mathrm{TRK})}$) are compatible within 0.2 cm. Finally, the aim of an additional selection based on the correlation between the number of ITS and TPC clusters is to reject out-of-bunch pile-up events: in particular, an event is rejected if the number of clusters registered by SDD and SSD is larger than a standard parameterization of the number of TPC clusters based on a second degree polynomial, provided by the ALICE Data Preparation Group. The effect of the various event selection stages is reported in Fig. 5.1 for the 2015 and 2018 data samples on the left and right panels, respectively. It is worth to notice that the most penalizing selection is the one developed for pile-up, which acts differently on the different periods, removing approximately 23% and 30% of the events for 2015 and 2018, respectively. In particular, this difference does not depend on the different triggers available for the two periods, since a similar rejection factor is obtained for each trigger, but on the running conditions which characterized the data taking period.

The remaining events are finally divided into centrality classes according to their multiplicity, defining each class as a given percentile of the overall multiplicity distribution. For this analysis, 10% wide centrality classes were chosen and are reported in Table 5.4.

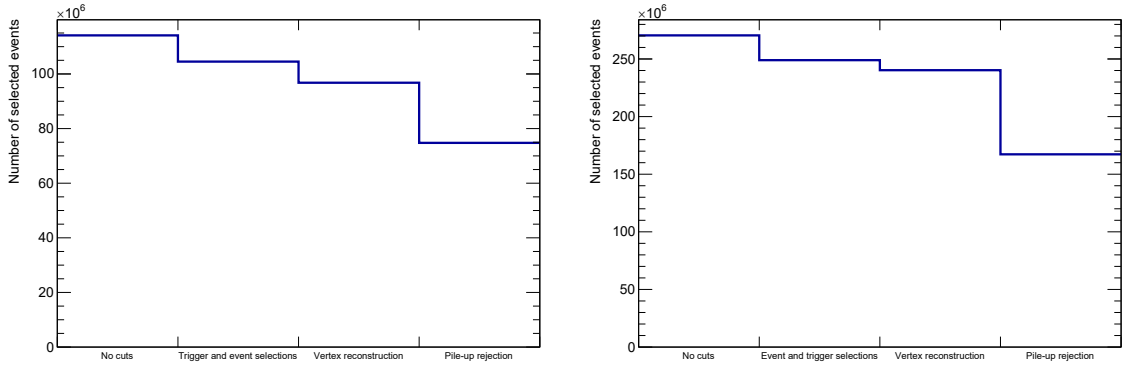

Fig. 5.1 Number of accepted events at each step of the event selection for the 2015 dataset (left) and the 2018 one (right).

Class	Centrality (%)	$\left\langle \frac{dN_{ch}}{d\eta_{lab}} \right\rangle$
I	0 - 10	1765 ± 52
II	10 - 20	1180 ± 31
III	20 - 30	786 ± 20
IV	30 - 40	512 ± 15
V	40 - 50	318 ± 12
VI	50 - 60	183 ± 8
VII	60 - 70	96.3 ± 5.8
VIII	70 - 80	44.9 ± 3.4
IX (Ξ only)	80 - 90	17.52 ± 1.89
INEL > 0	0 - 90	545 ± 17

Table 5.4 Summary of the multiplicity classes and the related mean charged particle multiplicity $\left\langle \frac{dN_{ch}}{d\eta_{lab}} \right\rangle$ for cascades. The $\left\langle \frac{dN_{ch}}{d\eta_{lab}} \right\rangle$ values were measured for $|\eta_{lab}| < 0.5$ and provided by the ALICE Data Preparation Group.

5.4 Topological reconstruction

The secondary vertex finding process described in Sec. 2.6.2 is exploited for the reconstruction of cascades and is centrally carried out by the ALICE experiment at the level of data reconstruction. This procedure relies on the peculiar decay topology which is a clear signature of the presence of a multi-strange baryon and is reported for a Ξ^- particle in Fig. 5.2. After being produced at the primary vertex (PV), the Ξ^- ($\overline{\Xi}^+$) particle undergoes a first weak decay into a pair of Λ ($\overline{\Lambda}$) and π^- (π^+). In the following the charged pion produced at this stage will be referred to as bachelor particle, while the Λ baryon as V0. As well as for the cascade, the Λ ($\overline{\Lambda}$) particle is not stable and decays weakly into a p–π^- ($\overline{\text{p}}$–π^+) pair. The decay topology of an Ω baryon differs from the one just described for the bachelor particle only, since the pion is replaced by a kaon. Being Λ baryons charge neutral, they do not interact electromagnetically with the detectors and, hence, they cannot be directly detected. Therefore, the initial Ξ cascade is reconstructed backwards starting from the three charged daughter particles.

The reconstruction process relies on very loose selections depending on the topology of the cascade decay, which must be tightened at the analysis level to reject the huge combinatorial background. The detailed set of topological selections implemented for this work is reported in Table 5.5. The most effective topology selection when dealing with weak decays is related to the pointing angle: the pointing angle is defined as the angle between the reconstructed mother particle momentum and a straight line connecting the vertex where the particle was generated and its decay vertex. A tight enough selection on the cosine of the pointing angle for both the Ξ and the V0 decays guarantees a good pointing of the decay products to the initial production vertex. In this way only cascades (V0s) really coming from the primary vertex (secondary vertex) are taken into account for the analysis. The cosine of the pointing angle is also used in this analysis to exclude wrongly reconstructed cascades for which the bachelor particle has been combined to the baryon V0 daughter p or $\overline{\text{p}}$. A diversified selection on the maximum bachelor-to-baryon pointing angle has been developed in order to remove candidates which could be reconstructed with this wrong topology, whose presence is more important for central events and low p_{T} and is reported in Table 5.6. Since the effect of this selection is quite penalizing in terms of signal rejection and that the wrong topology association becomes less important moving from central to peripheral events, the selection is applied in the centrality range 0–50% only. An additional minimum decay radius, defined in the two-dimensional x-y plane, is set for both the cascade and the V0, in order to reject decays which are not displaced enough, to guarantee a good secondary vertex determination. Moreover, the V0 is also required to decay before the inner wall of

the TPC detector placed at ≈ 85 cm, in order to grant a complete TPC tracking for the V0 daughters. Geometrical selections on the DCA between the daughter particles and the PV are also implemented: since the bachelor and the V0 daughters are not directly coming from the interaction point, a minimum value of the DCA between each particle and the PV is required. Finally, the DCA between particles coming from the same decay vertex is also computed, requiring a small enough value between bachelor and V0, and between the V0 daughters. In addition to the selections related to the decay topology, a set of kinematic and track quality selections are also implemented. A first selection on the cascade rapidity and on its daughters' pseudorapidity is introduced to consider only particles detected in the central barrel region, in order to have a full operational tracking. Good quality TPC tracks, leading to a good momentum resolution, are also required in terms of minimum number of TPC clusters and good TPC track fit quality, in analogy with what was done for the nuclei analysis. In addition to those, a specific selection is dedicated to the removal of those tracks falling for a large fraction of their path in a dead sector of the TPC. These tracks are not correctly modeled in the MC, so that their removal allows to avoid biases, as per the ALICE DPG prescription. In particular the so called geometrical cut is implemented for the centrality classes up to 40%, while the usage of at least 50 TPC clusters for the PID is required for the other centrality classes. Finally, a very loose PID selection is performed with the TPC detector, requiring that daughter particles are correctly identified within a given range of n_σ in the TPC. Table 5.7 summarizes the described track and kinematic selections.
After the application of all selections, the invariant mass m_{inv} of the cascade candidate is calculated as

$$m_{inv} = \sqrt{\left(\sqrt{m_\Lambda^2 + \vec{p}_\Lambda^2} + \sqrt{m_{\text{bach}}^2 + \vec{p}_{\text{bach}}^2}\right)^2 - (\vec{p}_\Lambda + \vec{p}_{\text{bach}})^2} \tag{5.1}$$

where $\vec{p}_\Lambda = \vec{p}_{\text{pos}} + \vec{p}_{\text{neg}}$ is the three-momentum of the Λ candidate reconstructed from its positive and negative daughters, whose three-momenta are labeled as $\vec{p}_{\text{pos}}$ and $\vec{p}_{\text{neg}}$, respectively. These momenta are, together with the three-momentum vector of the bachelor particle $\vec{p}_{\text{bach}}$, the only three quantities needed to reconstruct the invariant mass of the cascade particle. m_Λ and m_{bach} are the nominal masses of the Λ and of the bachelor particles, taken from the PDG.

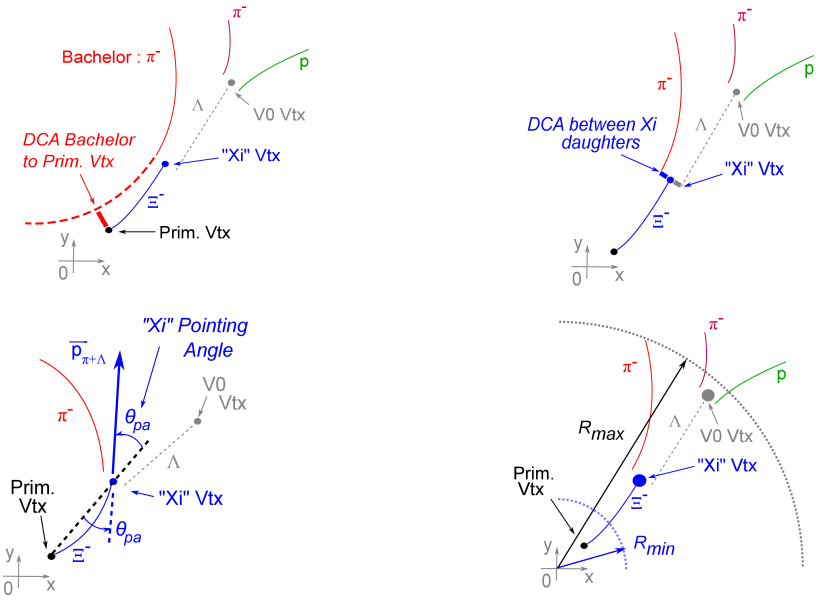

Fig. 5.2 Topology of the cascade decay for a Ξ baryon. Some of the key quantities used to describe the decay are also reported.

Variable	Selection
$\cos(\theta_{\mathrm{pa}})$	> 0.99
V0 $\cos(\theta_{\mathrm{pa}})$	> 0.99
bachelor–baryon $\cos(\theta_{\mathrm{pa}})$	parametric, see Table 5.6
R	> 1 cm
V0 R	> 3 cm, < 85 cm
DCA V0–PV	> 0.1 cm
DCA bachelor–PV	> 0.1 cm
DCA V0 daughters–PV	> 0.2 cm
DCA bachelor–V0	< 1 cm
DCA V0 daughters	$< 1\sigma$

Table 5.5 Topology selections applied in this work to the cascade decay.

p_{T} region (GeV/c)	bachelor–baryon $\cos(\theta_{\mathrm{pa}})$
$[0.8; 1.0]$	< 0.999
$[1.0; 2.0]$	< 0.9995
$[2.0; 2.6]$	< 0.9997
$[2.6; 3.2]$	< 0.9999
$[3.2; 10.0]$	< 0.999999

Table 5.6 Parametric selection on the bachelor–baryon cosine of pointing angle for the centrality classes in the region 0–50%.

Variable	Selection
$\|y\|$	< 0.5
daughters' $\|\eta\|$	< 0.8
V0 mass	$\|m_{\Lambda}^{(\mathrm{rec})} - m_{\Lambda}^{(\mathrm{PDG})}\| < 5$ MeV/c^2
Proper lifetime	$< 3c\tau$
TPC clusters	≥ 80
TPC clusters over findable	≥ 0.8
χ^2 per TPC cluster	≤ 2.5
TPC n_σ	≤ 5
TPC refit	true
Track quality for Pb–Pb	true

Table 5.7 Kinematic and track selections applied in this work.

5.5 Centrality flattening

Due to how it is estimated, the centrality distribution of the events considered for this analysis features some small deviation from flatness. Moreover the data sample from 2018 is not centrality-flat by definition, since the two Central and SemiCentral triggers were adopted to enhance the number of collected events in the centrality ranges 0–10% and 30–50%, respectively. These two features can bias the final results, since in wide centrality classes such as those used for this analysis the integration of the signal results from a non-physical weighted sum of events with a wrong centrality distribution. The non-flatness is clearly shown in Fig. 5.3, where the centrality distribution of collected events is reported for the 2015 and 2018 data taking periods on the left and on the right, respectively. In particular, a significant discrepancy with respect to a flat behavior is observed in the former for peripheral events, and in the latter for the very central ones. Moreover, the huge difference in terms of number of collected events where the additional triggers were used would also have a strong biasing effect on the evaluation of the integrated centrality result: due to the larger number of central and semi-central events, the corrected spectrum would be wrongly driven by those.
In order to avoid these drawbacks, the centrality distribution of data is re-scaled to make it flat. In principle, this could be the case also for MC, since different number of events were produced depending on the centrality class. This procedure is indeed applied to each MC sub-sample used for the centrality differential analysis.
However, for the integrated centrality class the MC flattening is more complex due to the very heavy injection scheme implemented for the strangeness injected samples, which is not constant over the whole centrality region. The number of Ξ^- candidates is reported in Fig. 5.4 for the sum of all MC samples anchored to the 2015 and 2018 data samples on the

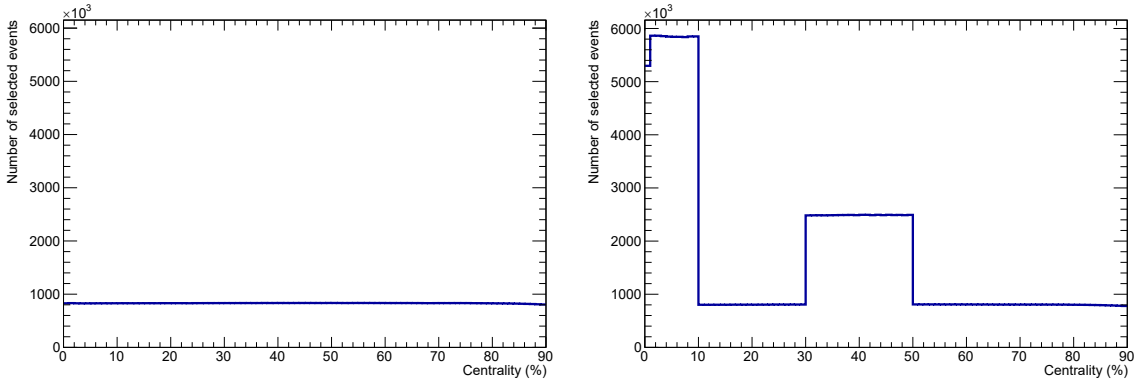

Fig. 5.3 Centrality distribution of the selected events for the 2015 (left) and 2018 (right) data taking periods.

left and on the right, respectively. The number of generated Ξ^- is far from being distributed in a physical way with centrality. Thus an additional re-weighting procedure is required. In order to obtain a matching between the real production yields of Ξ particles and the MC shape, each centrality interval i of the MC distribution is multiplied by custom weights defined as

$$w_{\mathrm{i}} = \frac{\langle N_{\mathrm{gen}}^{(\mathrm{I})} \rangle}{N_{\mathrm{gen,i}}} \frac{\frac{\mathrm{d}N}{\mathrm{d}y}_{\mathrm{meas,i}}}{\frac{\mathrm{d}N}{\mathrm{d}y}_{\mathrm{meas}}^{(\mathrm{I})}} \tag{5.2}$$

where $N_{\mathrm{gen,i}}$ is the number of generated Ξ^- in the centrality bin i, while $\langle N_{\mathrm{gen}}^{(\mathrm{I})} \rangle$ is the average number of generated Ξ^- in the centrality class 0–10%. The latter is a constant value over the whole procedure and its choice does not affect the final results, and it was chosen to keep, at least for the most central class, the same order of magnitude of produced particles before and after the re-weighting procedure. The goal of the second part of the equation is twofold: first of all, in each 10%-wide centrality class of the analysis the number of generated Ξ^- must be centrality flat. Then, the Ξ^- distribution in the centrality intervals of the analysis must mimic the centrality distribution of real Ξ^- baryons: for this reason, the integrated production yields of the Ξ^- baryon $\frac{\mathrm{d}N}{\mathrm{d}y}_{\mathrm{meas,i}}$, for each centrality class, are taken from the centrality differential result of this work reported in Table 5.11. The distribution of generated Ξ^- as a function of centrality after the re-weighting procedure is reported in Fig. 5.5. The same procedure described above is used for the other particles studied in this analysis.

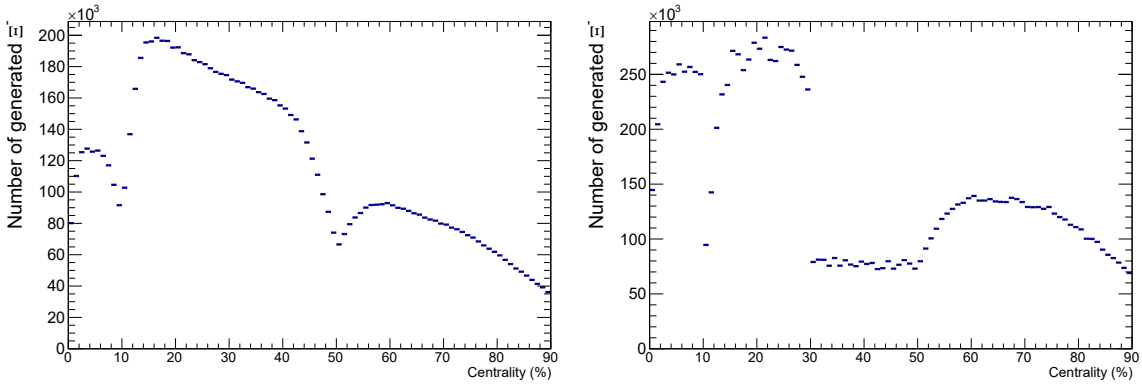

Fig. 5.4 Original centrality distribution of the number of generated Ξ for the 2015 (left) and 2018 (right) MC samples.

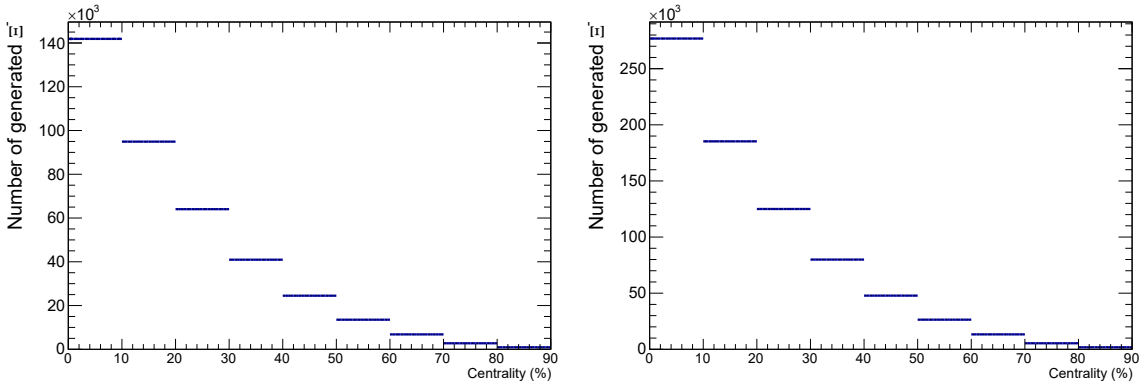

Fig. 5.5 Centrality distribution of the number of generated Ξ for the 2015 (left) and 2018 (right) MC samples after the reweighting procedure.

5.6 Signal extraction

The cascade reconstruction algorithm provides an estimate of the mass of the cascade candidates starting from the measured four-momenta of their daughters, as described by Eq. 5.1. The raw signal is extracted by fitting the invariant mass histograms obtained dividing the candidates according to their p_{T} and considering the centrality of the event where they were registered. An example for this procedure is reported in Fig. 5.6 and in Fig. 5.7 for Ξ and Ω particles, respectively; different transverse momentum and centrality intervals are reported, on the left for the 2015 data sample, on the right for the 2018 one. The invariant mass distribution is described as the sum of a signal and a background functions. Due to the non-Gaussian tails of the signal, this is described with a double-sided Crystal-Ball defined as

$$sig(x) = N_{\mathrm{raw}} \begin{cases} \left(\frac{n_{\mathrm{L}}}{|\alpha_{\mathrm{L}}|}\right)^{n_{\mathrm{L}}} e^{-\frac{\alpha_{\mathrm{L}}^2}{2}\left(\frac{n_{\mathrm{L}}}{|\alpha_{\mathrm{L}}|}-|\alpha_{\mathrm{L}}|-\frac{x-\mu}{\sigma}\right)^{-n_{\mathrm{L}}}} & \text{for } \frac{x-\mu}{\sigma} \leq \alpha_{\mathrm{L}} \\ e^{-\frac{(x-\mu)^2}{2\sigma^2}} & \text{for } -\alpha_{\mathrm{L}} < \frac{x-\mu}{\sigma} < \alpha_{\mathrm{R}} \\ \left(\frac{n_{\mathrm{R}}}{|\alpha_{\mathrm{R}}|}\right)^{n_{\mathrm{R}}} e^{-\frac{\alpha_{\mathrm{R}}^2}{2}\left(\frac{n_{\mathrm{R}}}{|\alpha_{\mathrm{R}}|}-|\alpha_{\mathrm{R}}|-\frac{x-\mu}{\sigma}\right)^{-n_{\mathrm{R}}}} & \text{for } \frac{x-\mu}{\sigma} \geq \alpha_{\mathrm{R}} \end{cases} \tag{5.3}$$

where, apart from the mean μ and standard deviation σ which describe the gaussian core, the α_{R}, α_{L}, n_{R} and n_{L} parameters are responsible for the non-Gaussian tails on the left (L) and on the right (R) of the peak. In particular, the α parameters define, in terms of number of standard deviations from the central value, the point where the tail starts, while the n parameters describe the steepness of the tail.

Since the large number of free parameters can lead to instabilities in the fitting procedure, a preliminary fit to the MC MB sample in the same p_{T} region is performed in order to fix the four tail parameters in a clean situation where the background is not present. This procedure is reported in Fig. 5.8 for two different transverse momentum ranges in the MC samples anchored to the 2018 data taking period, for Ξ and Ω particles on the left and on the right, respectively. This is a clear evidence on how important are the deviations from a simple Gaussian picture and on the fact that the addition of non-Gaussian tails is indeed necessary to properly describe the cascade signal.

The background varies significantly depending on the centrality and transverse momentum region: for central events and low p_{T} the background shows a steeply falling behavior depending on the invariant mass window, while it becomes flatter for peripheral events and high p_{T}. For this reason, the background is fit with a second degree polynomial, which evolves into a first degree polynomial depending on the centrality and transverse momentum

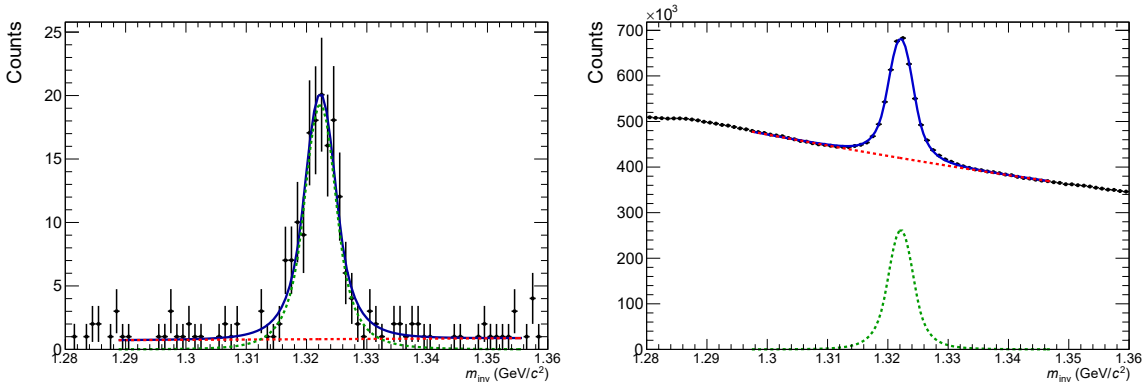

Fig. 5.6 Invariant mass distribution for the Ξ particle for the centrality class VIII in the region 6.0 GeV/$c \leq p_T <$ 7.0 GeV/c (left) and for the centrality class I in the region 2.2 GeV/$c \leq p_T <$ 2.4 GeV/c (right). The green and red dashed lines represent signal and background, respectively. The blue line is the sum of the signal and background components.

region. As an example, for the Ξ baryon, in the centrality classes I, II and for the integrated sample the second degree polynomial is used up to $p_T = 4.6$ GeV/c, while in the other centrality classes a first degree polynomial is suitable to fit the background shape over the whole p_T region.

For each centrality and transverse momentum interval, the raw number of cascades is extracted via bin counting: in the reference region between $\mu - 5\sigma$ and $\mu + 5\sigma$ the integral of the background function is subtracted from the one of the invariant mass distribution. The statistical uncertainty on the raw signal is finally calculated by adding in quadrature the error on the integral from the invariant mass distribution and the one from the background function integration, evaluated taking into account the covariance matrix resulting from the fit.

5.7 Efficiency x acceptance correction

The only relevant correction to be applied to the raw cascade signal is the efficiency x acceptance one. As well as for nuclei, it is evaluated starting from the MC and it is supposed to reproduce the signal loss due to the geometrical acceptance, the efficiency of the detector and the selections applied at the analysis level and described in Sec. 5.4. The number of generated and reconstructed cascades N_{gen} and N_{rec} is exploited to evaluate the acceptance x efficiency correction as

$$\varepsilon \times Acc\,(p_T) = \frac{N_{rec}\,(p_T)\,(|\eta| < 0.8, |y| < 0.5, |m - \mu| < 5\sigma)}{N_{gen}\,(p_T)\,(|y| < 0.5)} \tag{5.4}$$

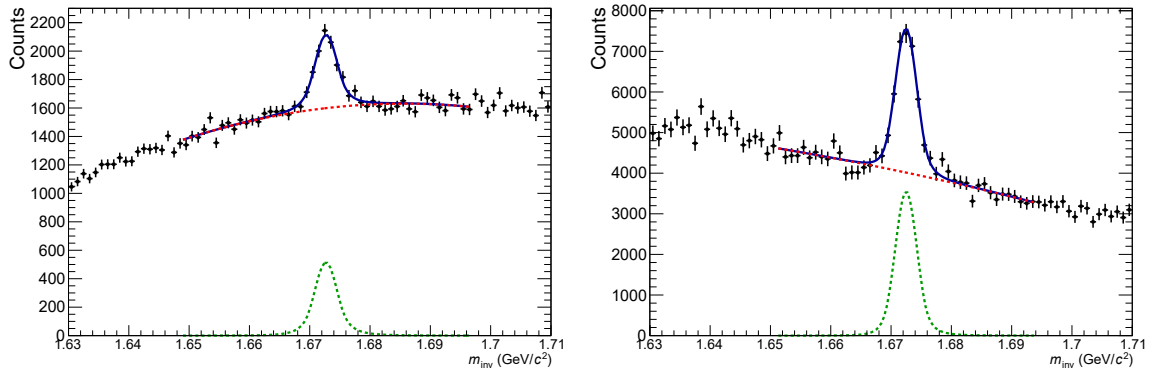

Fig. 5.7 Invariant mass distribution for the Ω particle for the centrality class II in the region 4.0 GeV/$c \leq p_T <$ 4.4 GeV/c (left) and for the centrality class V in the region 1.6 GeV/$c \leq p_T <$ 2.0 GeV/c (right). The green and red dashed lines represent signal and background, respectively. The blue line is the sum of the signal and background components.

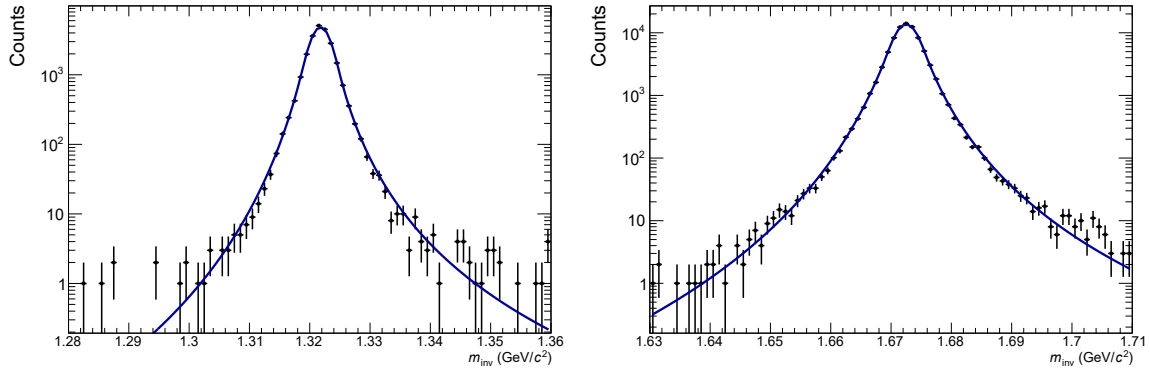

Fig. 5.8 Invariant mass distribution in the 2018 MC sample for the Ξ particle for the MB centrality class in the region 1.4 GeV/$c \leq p_T <$ 1.6 GeV/c (left) and for the Ω particle for the MB centrality class in the region 5.0 GeV/$c \leq p_T <$ 6.0 GeV/c (right). The blue line represent the double-sided Crystal-Ball function used to describe the MC signal.

where p_{T} is the transverse momentum of the reconstructed cascade. The number of reconstructed particles is counted in the same invariant mass region where the signal extraction is performed on data, which varies depending on the centrality and transverse momentum region as described in the previous section. The correction as a function of p_{T} is reported for each centrality class in Fig. 5.9 and Fig. 5.10 for Ξ^- and Ω^-, respectively. The left and right panels show the efficiency corrections for the 2015 and 2018 samples, respectively. First of all, although the analysis described in this chapter is based on two different data taking periods, the efficiencies are compatible between the two samples. This is not a guaranteed a-priori feature when combining the measurements of different data taking periods. A large discontinuity in the behavior as a function of centrality is observed around 40%. This effect is introduced by the requirement of the geometrical cut in the centrality region 0–40%, which is responsible for an additional rejection of about 50% of the candidates which pass all the other selections. The p_{T} behavior of the correction is similar to the nuclei one, with a steep rise at low transverse momentum until a plateau region is reached. At high p_{T} a decreasing trend is observed. This is due to the track selections applied, since at high p_{T} the daughter particles from the cascade decay have small curvature and point straight to the primary vertex. Thus, the DCA selections requiring a minimum distance between the daughter particle tracks and the primary vertex, implemented to require the daughter tracks to come from a secondary vertex, are affecting differently the efficiency depending on p_{T}.
Two main differences are observed with respect to the nuclei analysis: first of all the plateau value is lower in this analysis, since the weak decay finder algorithm is not fully efficient in reconstructing cascades. Moreover a strong centrality dependence is present: in Pb–Pb collisions, a lower reconstruction efficiency is expected for central events, where the number of produced particles is higher and the tracking algorithm becomes less efficient. This effect becomes milder for peripheral events. For this reason the correction is evaluated separately for each centrality class and applied to the corresponding raw spectrum.

5.8 Systematic uncertainties

Similarly to what has been done for the nuclei analysis, a potential source of systematic error is evaluated by changing a specific selection or procedure both in data and MC and evaluating the impact on the final corrected spectrum.
In order to decouple the effect of statistical fluctuations on the systematic uncertainty evaluation, each source of systematic uncertainty is requested to undergo an exclusion test called Barlow check [175]. Since the uncertainties are evaluated as a variation with respect to the

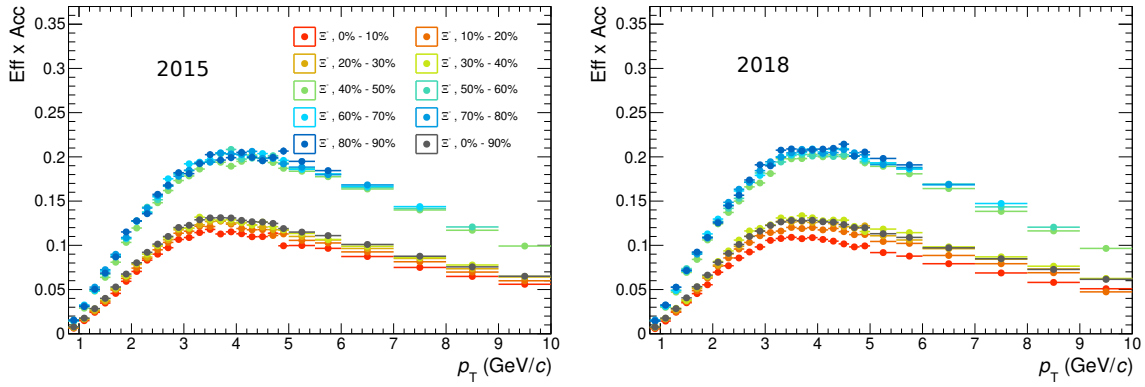

Fig. 5.9 Efficiency x acceptance for the 2015 (left) and 2018 (right) MC samples for the Ξ^- particle as a function of the transverse momentum. Each color corresponds to a different centrality class.

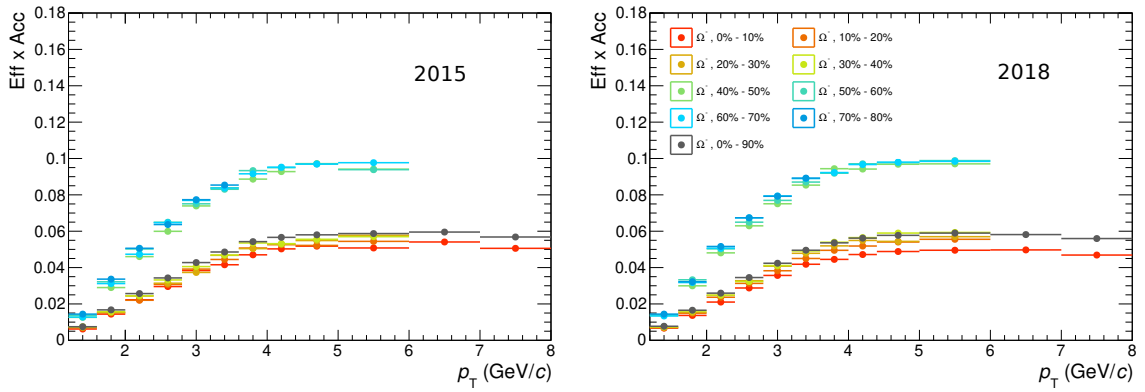

Fig. 5.10 Efficiency x acceptance for the 2015 (left) and 2018 (right) MC samples for the Ω^- particle as a function of the transverse momentum. Each color corresponds to a different centrality class.

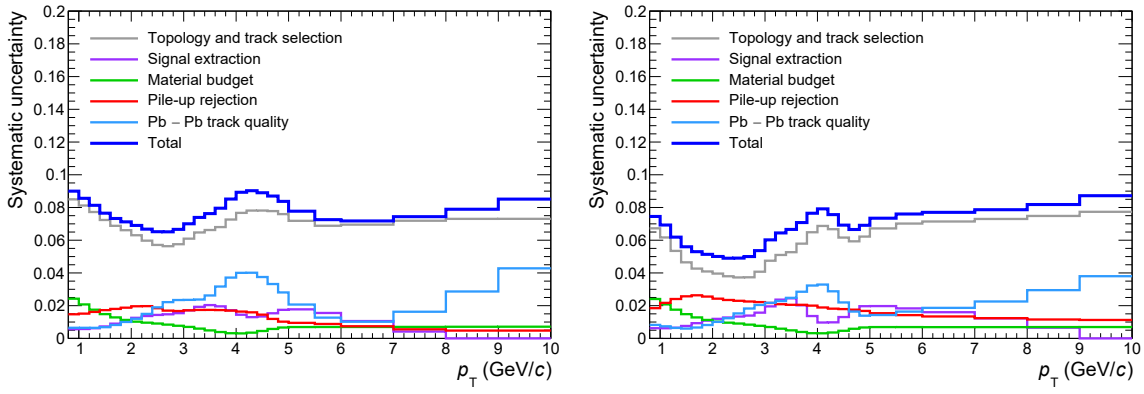

Fig. 5.11 Systematic uncertainty of Ξ baryons as a function of the transverse momentum for the MB multiplicity class of the 2015 (left) and the 2018 (right) data sample. The blue thicker line is the total systematic uncertainty, while each single contribution is defined by a different color.

default flow of the analysis, a Barlow-sigma σ_{B} is defined as

$$\sigma_{\mathrm{B}} = \sqrt{\left|\sigma_{\mathrm{def}}^2 - \sigma_{\mathrm{var}}^2\right|} \tag{5.5}$$

where σ_{def} and σ_{var} are the statistical uncertainties of the default and varied analyses, respectively. If the systematic uncertainty obtained from the variation is smaller than two times σ_{B}, it is considered as not significant and, hence, dropped. All the contributions passing the Barlow check are finally summed in quadrature to obtain the total systematic uncertainty. The total systematic uncertainty for the Ξ and Ω particles is reported in Fig. 5.11 and Fig. 5.12, respectively. Since the final production spectra will be shown for the sum of particles and antiparticles, the total uncertainty is evaluated as the weighted average of the matter and antimatter systematic uncertainties, where the statistical error on the production spectra is used as a weight. For both the Ξ and Ω particles, the major source of uncertainty is due to the effect of the topological selections, which accounts up to 10% for the former and 15% for the latter. Minor effects are due, for the Ξ baryon, to the pile-up rejection and Pb–Pb track quality selection at low and intermediate p_{T}. On the other hand, these latter two contributions are more important for Ω at high transverse momentum, where signal extraction is also contributing relevantly. A detailed description of each source of systematic uncertainty is given in the next paragraphs.

Topology and track selection All the selections used in the cascade reconstruction contribute to the major part of the systematic uncertainty in this kind of analyses. This is due to the complex decay topology which implies the usage of a large number of selections and to

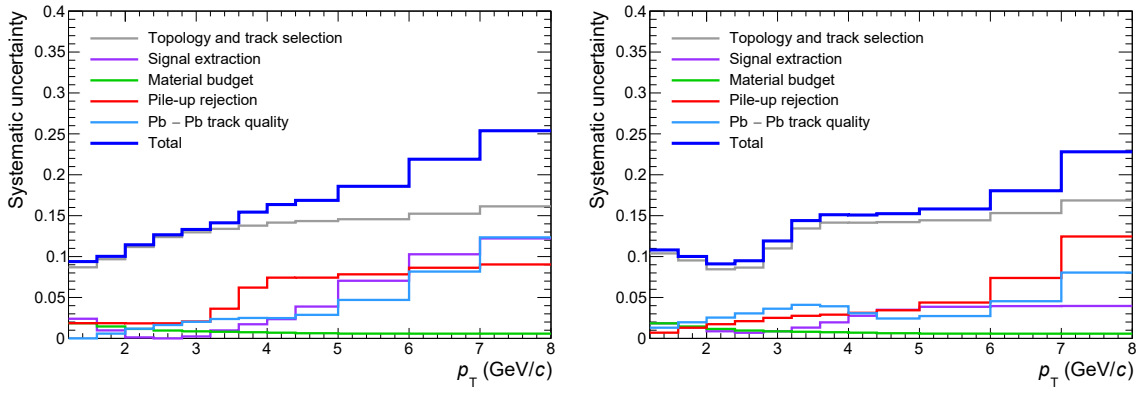

Fig. 5.12 Systematic uncertainty of Ω baryons as a function of the transverse momentum for the MB multiplicity class of the 2015 (left) and the 2018 (right) data sample. The blue thicker line is the total systematic uncertainty, while each single contribution is defined by a different color.

the the fact that the MC does not reproduce perfectly the effect of the selections performed on data.

In order to test this effect on the analysis a specific procedure is developed in this thesis work. First of all, the signal extraction is re-performed by varying the selections one by one while keeping fixed the other ones, with an evenly-spaced scan between an upper and lower limit. The limits and number of variations for each selection criterion are reported in Table 5.8. Moreover, also the MC signal is extracted applying the same variation and within the same region used for the bin counting method in data. Systematic uncertainties are evaluated applying variations which lead to a increase or decrease of around 10% of the raw signal. For each transverse momentum region, centrality class and selection criterion, the contribution to the systematic uncertainty is evaluated though the double ratio $R^{(\pm)}$ as

$$R^{(\pm)} = \left| 1 - \frac{\frac{\mathrm{raw}_{\mathrm{Data}}^{(\pm)}}{\mathrm{raw}_{\mathrm{Data}}^{(\mathrm{def})}}}{\frac{\mathrm{raw}_{\mathrm{MC}}^{(\pm)}}{\mathrm{raw}_{\mathrm{MC}}^{(\mathrm{def})}}} \right| \tag{5.6}$$

where $\mathrm{raw}_{\mathrm{Data}}$ and $\mathrm{raw}_{\mathrm{MC}}$ are the raw signal extracted for data and MC, respectively. The raw signal is extracted in the three configurations defined by the superscripts reported within parentheses: (def), $(+)$ and $(-)$ represent the default case and the variations which lead to a modification of the raw signal in data not exceeding $+10\%$ and -10%, respectively. Thus the $R^{(\pm)}$ quantity defines how well the effect obtained by varying a selection on data is reproduced in the MC. In order to give a conservative estimate of the systematic uncertainty due to the selection criteria, the maximum value between $R^{(+)}$ and $R^{(-)}$ is considered. For

Variable	Limits	n. of variations
$\cos(\theta_{\mathrm{pa}})$	[0.950 – 0.999]	21
V0 $\cos(\theta_{\mathrm{pa}})$	[0.950 – 0.999]	21
bachelor–baryon $\cos(\theta_{\mathrm{pa}})$	[0.99900 – 0.99999]	10
R	[0.5 – 1.5] cm	11
V0 R_{min}	[1 – 5] cm	11
V0 R_{max}	[45 – 125] cm	5
DCA V0–PV	[0.05 – 0.15] cm	11
DCA bachelor–PV	[0.05 – 0.15] cm	11
DCA V0 daughters–PV	[0.1 – 0.3] cm	11
DCA bachelor–V0	[0.5 – 1.4] cm	10
DCA V0 daughters	[0.5 – 1.4] σ	10
V0 mass window	[2 – 6] MeV/c^2	5
Proper lifetime	[2 – 5] $c\tau$	7
TPC clusters	[70 – 90]	11
TPC clusters over findable	[0.75 – 0.90]	11
TPC n_σ	[2 – 7]	6

Table 5.8 Lower and higher limits of the variations used for the evaluation of the systematic uncertainty from the topology and track selections. The number of variations is also reported.

each transverse momentum and centrality region, the systematic uncertainty is evaluated as the sum in quadrature of the R values obtained for each single selection criterion.
In principle, this study should be carried out separately for each centrality class of the analysis. Unfortunately, due to the limited number of cascade candidates, in particular for peripheral events, this in not possible and would lead to overestimated systematic uncertainties. For this reason, a weighted average on the values obtained for each centrality is used and is evaluated as

$$\sigma_{\mathrm{sel}}(p_{\mathrm{T}}) = \frac{\sum_{\mathrm{i=I}}^{\mathrm{IX}} w_{\mathrm{i}}(p_{\mathrm{T}})\sigma_{\mathrm{sel,i}}(p_{\mathrm{T}})}{\sum_{\mathrm{i=I}}^{\mathrm{IX}} w_{\mathrm{i}}(p_{\mathrm{T}})} \tag{5.7}$$

where $\sigma_{\mathrm{sel,i}}$ is the total systematic uncertainty due to the selection criteria evaluated in the centrality class i and w_{i} is the raw signal for that centrality class. In this way, the systematic uncertainty is defined across the whole centrality region by a common value.

Signal extraction The signal extraction method is also tested in order to asses how a different approach could lead to a slightly different final result. First of all, the fitting procedure is varied by enlarging and restricting the fitting window by 1σ, where σ is the standard deviation of the final fit in the default case. With this approach, the shape of the background changes, leading to an estimate of the impact that a different background fitting

	Variations
Fit region	def, def$\pm 1\sigma$
Counting region	def, def$+1\sigma$, def$+2\sigma$
Method	bin counting, signal integration

Table 5.9 List of the variations applied to the signal extraction, used to determine the systematic uncertainty.

function has on the signal extraction. Moreover, the bin counting region is enlarged to 6 and 7σ to check if a fraction of the signal is lost due to the default $\mu \pm 5\sigma$ choice. Finally, the bin counting technique is also replaced by the integration of the signal function. The summary of the changes applied to the signal extraction technique for systematic uncertainty evaluation is reported in Table 5.9. For each of the three cases, the difference between the variation which yields to the maximum discrepancy with respect to the default and the default raw signal itself is considered as the systematic uncertainty. The total systematic uncertainty is given by the sum in quadrature of these three components. In order to reduce statistical fluctuations, this source of systematic uncertainties is evaluated for the integrated centrality class and the relative error is kept fixed across centrality.

Material budget A potential mismatch in the MC description of the ALICE material budget could be a source of systematic uncertainty and is evaluated with the same procedure described in Sec. 4.7 for the nuclei analysis. The main difference is due to the fact that two separate MC productions with different material budget variation are available depending on the transverse momentum region. For $p_{\mathrm{T}} > 3.0$ GeV/c a first simulation with a $\pm 4.5\%$ variation in the material amount is used. Since the number of cascade candidates is not large enough to evaluate a reliable efficiency for $p_{\mathrm{T}} < 3$ GeV/c, an additional production with a $\pm 10\%$ material budget variation and heavier cascade injection scheme is used. In order to compare the two simulations, the results obtained from the latter are scaled down by a factor 0.45.

Pile-up rejection The removal of out-of-bunch pile-up events is described in Sec. 5.3 and is applied at the event selection level. Nevertheless, alternative pile-up rejection methods can be used. A possible rejection can be performed at particle level, requiring that at least one out of the three daughter tracks has been successfully refitted using the ITS information or has a TOF cluster. The first condition implies that at least one track is well reconstructed in the SPD layers of the ITS, which are fast detectors able to distinguish between particles coming from different bunch crossings. Unfortunately, this method decreases the detection

Variable	Variations
Sector width (n. of pads)	2, 3, 4
Track length (cm)	120, 130, 140
TPC clusters for PID	40, 50, 60

Table 5.10 List of the variations applied to the selection for Pb–Pb track quality, used to determine the systematic uncertainty.

efficiency at high transverse momentum, where refitting gets more complicated. To cope with this issue, this selection is complemented by the second condition exploiting TOF, a fast detector which has higher efficiency at high p_{T}. The requirement of either the refitting in ITS or the TOF cluster ensures pile-up removal without too large efficiency reductions over the whole transverse momentum region probed by the analysis. The double ratio between data and MC defined by Eq. 5.6 is evaluated for this additional requirement with respect to the standard analysis and an R value as a function of the transverse momentum is evaluated for each centrality class. As it was described in Sec. 5.8 and in particular in Eq. 5.7, a common systematic uncertainty across centrality is evaluated as the weighted average over the number of candidates of each centrality class.

Track quality The track quality selection suggested by the ALICE DPG and implemented in this analysis is also slightly changed in order to search for systematics. The geometrical cut applied in the centrality classes between 0% and 40% is tested varying the width of the TPC dead sectors and the minimum requirement on the track length. In the centrality region 40–90% also the selection on the minimum number of TPC clusters used for the PID is varied. The default settings and variations are reported in Table 5.10. Half the difference between the maximum and minimum variations is assumed as a systematic uncertainty. The variation on the number of TPC clusters used for the PID is observed to be negligible and largely suppressed by the Barlow test. Since the effect of this selection is expected to be centrality dependent, the final contribution is computed as the sum in quadrature of the two variations of the geometrical cut configuration, separately for each centrality class.

5.9 Production spectra

The production spectra of cascades are obtained by dividing the raw signal $\frac{\mathrm{d}^2N_{\mathrm{raw}}}{\mathrm{d}p_{\mathrm{T}}\mathrm{d}y}$ per transverse momentum and rapidity unit by the efficiency $\times$ acceptance correction $\varepsilon \times Acc$:

$$\frac{1}{N}\frac{\mathrm{d}^2N}{\mathrm{d}p_{\mathrm{T}}\mathrm{d}y} = \frac{1}{N}\frac{1}{\varepsilon \times Acc}\frac{\mathrm{d}^2N_{\mathrm{raw}}}{\mathrm{d}p_{\mathrm{T}}\mathrm{d}y} \,. \tag{5.8}$$

The number of events per centrality class N enters the calculation as a normalization factor. Each step of the analysis has been performed separately for matter and antimatter, and for the two data taking periods 2015 and 2018. The production spectra of particles and antiparticles were compared and a good agreement between them was observed, supporting the assumption that matter and antimatter are equally produced at LHC energies, as was also shown in Sec. 4.8 for the nuclei analysis. The ratio between the $\bar{\Xi}^+$ and Ξ^- ($\bar{\Omega}^+$ and Ω^-) transverse momentum spectra is reported in Fig. 5.13 (Fig. 5.14) for the 2015 and for the 2018 data samples, on the top and on the bottom panels, respectively. Since matter and matter production is compatible within uncertainties, the corrected spectra are evaluated as the weighted average between them. Under the reasonable assumption of fully correlated systematic effects, also the total systematic uncertainty is evaluated as the weighted average between those of matter and antimatter.

In order to obtain the final production spectra of cascades in Pb–Pb collisions at $\sqrt{s_{\mathrm{NN}}} =$ 5.02 TeV, the two data samples collected in 2015 and 2018 should be considered together. Before merging them together, their consistency has to be tested via the evaluation of the ratio of the corrected spectra from the two data samples, which is reported in Fig. 5.15 and in Fig. 5.16 for the Ξ and the Ω particles, respectively. For each multiplicity class, the ratio between the corrected spectra of the 2015 and 2018 data samples is reported as a function of transverse momentum with their statistical uncertainty. The shaded band centered at 1 represents the systematic uncertainty on the final production spectra when the two data samples are considered together and is evaluated as the weighted average between the systematic uncertainties of the two separate periods. The overall agreement is very good, with the only significant difference being observed in central collisions in the intermediate p_{T} region and amounting to $\approx 8\%$ maximum, thus sitting at the edge of the systematic uncertainty on the spectrum. For the most peripheral centrality class some deviations are also present, even though they are not significant due to the large statistical uncertainties on the measurement. For the other centrality classes no systematic difference is observed, while residual fluctuations are reasonably accounted for by the systematic uncertainties. For the Ω particle the trend is alike, even though larger statistical and systematic uncertainties are

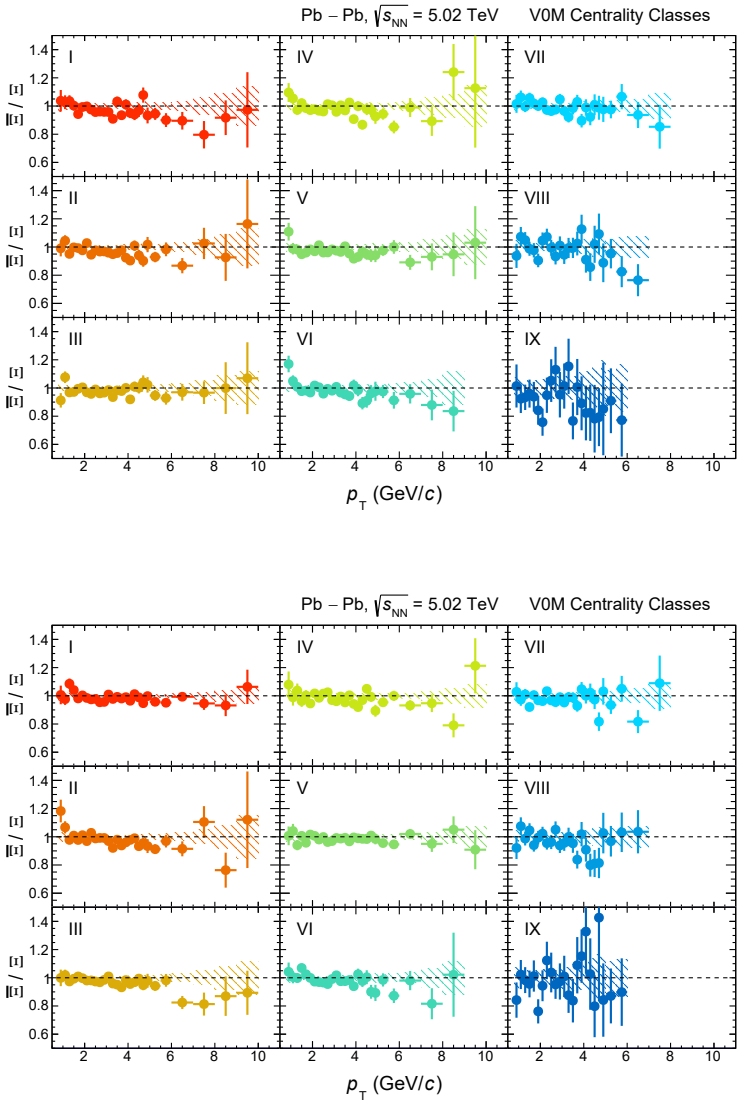

Fig. 5.13 Ratio between the corrected spectra of the $\bar{\Xi}^{+}$ and Ξ^{-} particles evaluated from the 2015 (top) and 2018 (bottom) data samples. The shaded band represents the total systematic uncertainty computed as the weighted average of the systematic uncertainties of matter and antimatter, as described in the text.

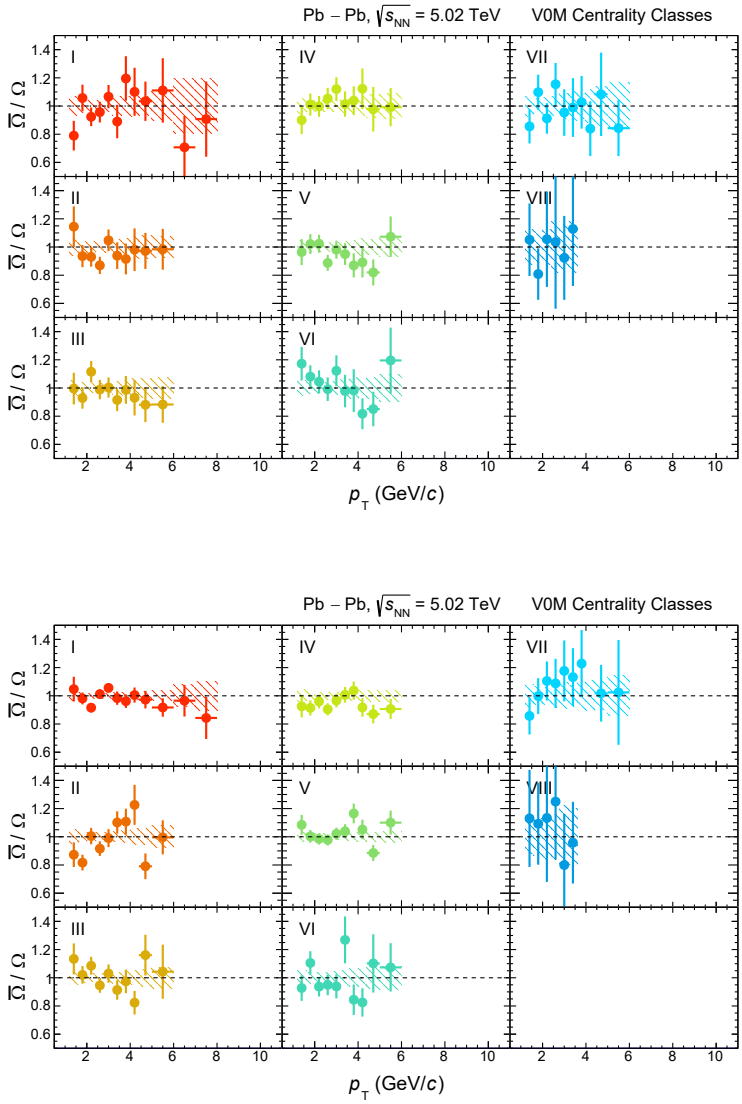

Fig. 5.14 Ratio between the corrected spectra of the $\bar{\Omega}^{+}$ and Ω^{-} particles evaluated from the 2015 (top) and 2018 (bottom) data samples. The shaded band represents the total systematic uncertainty computed as the weighted average of the systematic uncertainties of matter and antimatter, as described in the text.

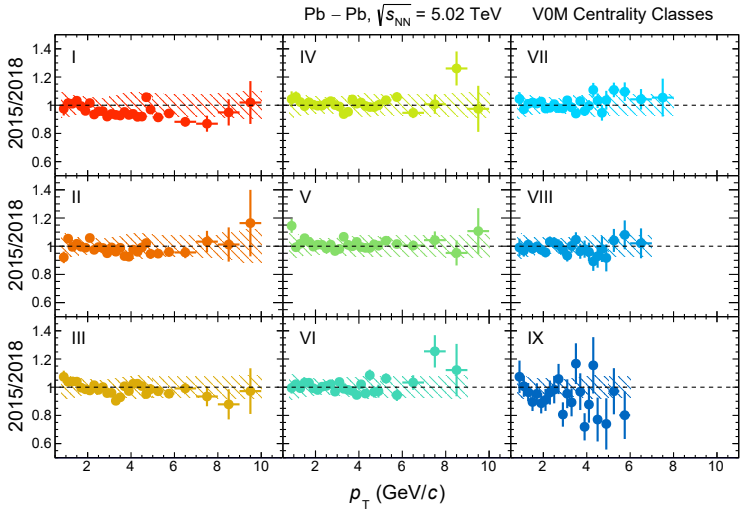

Fig. 5.15 Ratio between the corrected spectra of the Ξ particle evaluated from the 2015 and 2018 data samples. The shaded band represents the total systematic uncertainty computed as the weighted average of the systematic uncertainties of the two separate periods.

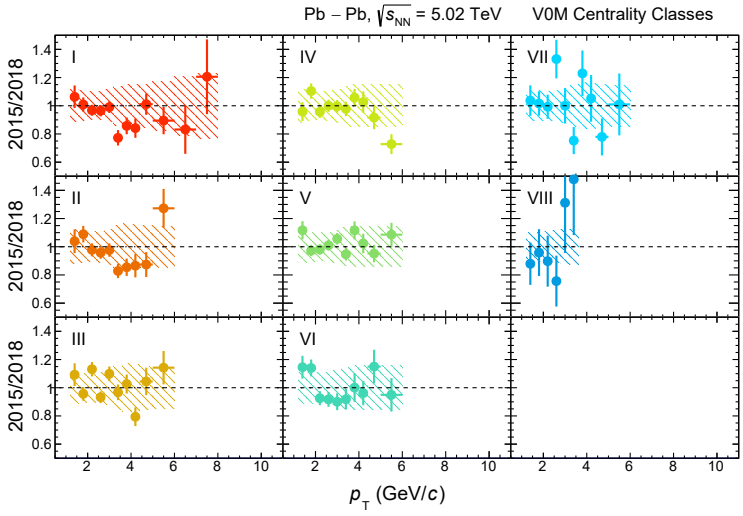

Fig. 5.16 Ratio between the corrected spectra of the Ω particle evaluated from the 2015 and 2018 data samples. The shaded band represents the total systematic uncertainty computed as the weighted average of the systematic uncertainties of the two separate periods.

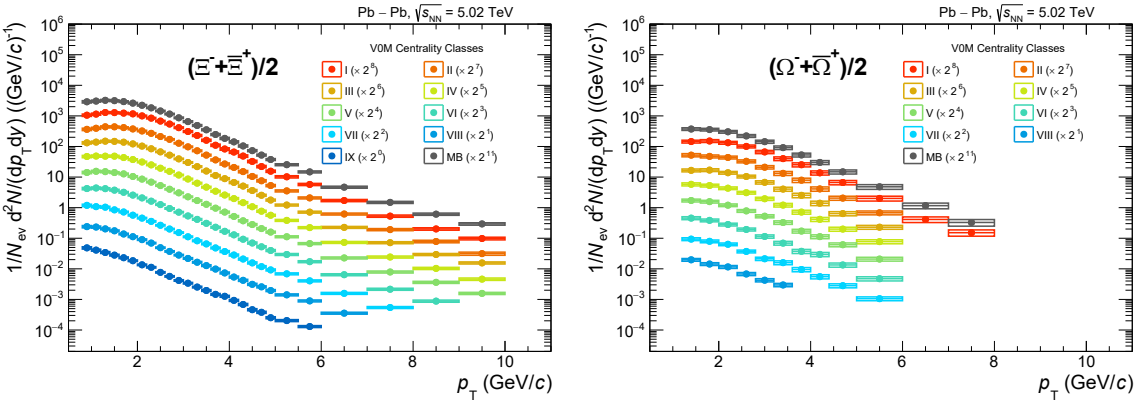

Fig. 5.17 Corrected p_{T} spectra for Ξ (left) and Ω (right) particles. Each color corresponds to a different centrality class. The statistical uncertainties are represented by vertical bars while the systematic uncertainties are represented by boxes.

present. For this reason, an additional contribution to the systematic uncertainty is added in quadrature to the total systematic uncertainty described in the previous section to take into account any possible discrepancy between the two datasets for the most central events only: a constant fit to the 2015/2018 spectra ratio is performed starting from a minimum transverse momentum of 2.0 GeV/c and half of the fit parameter is assigned as relative systematic uncertainty. This additional source of systematic uncertainty accounts for 4% in the most central class for both the Ξ and Ω particles.

The production spectra for the Ξ and Ω particles in Pb–Pb collisions at 5.02 TeV are reported in the left and right panels of Fig. 5.17 respectively, and have been computed as the weighted average between the data samples collected in 2015 and 2018. Moving from peripheral (blue points) to central events (red points), the cascade spectrum becomes harder and harder, being shifted to larger transverse momentum values. This effect can be interpreted as coming from the presence of a radial flow in central Pb–Pb collisions and is qualitatively explained as a hydrodynamic expansion of the medium produced in the collision.

Predictions coming from different theoretical models described in Sec. 3.3 are available and are compared to the final production spectra in Fig. 5.18. Out of all the centrality classes analyzed, results from central (class I, red), semicentral (class IV, green) and peripheral (class VIII, blue) classes are considered in the comparison so to study the capability of models to describe data as a function of centrality. The first phenomenological model considered is the hybrid model iEBE–VISHNU [141] with TRENTo [176] initial conditions (dashed lines), characterized by the implementation of both an hydrodynamical approach and a microscopic description of particle interactions after the hadronization. The predictions from this model, as well as in general for hydrodynamical models, are limited to the low to mid transverse

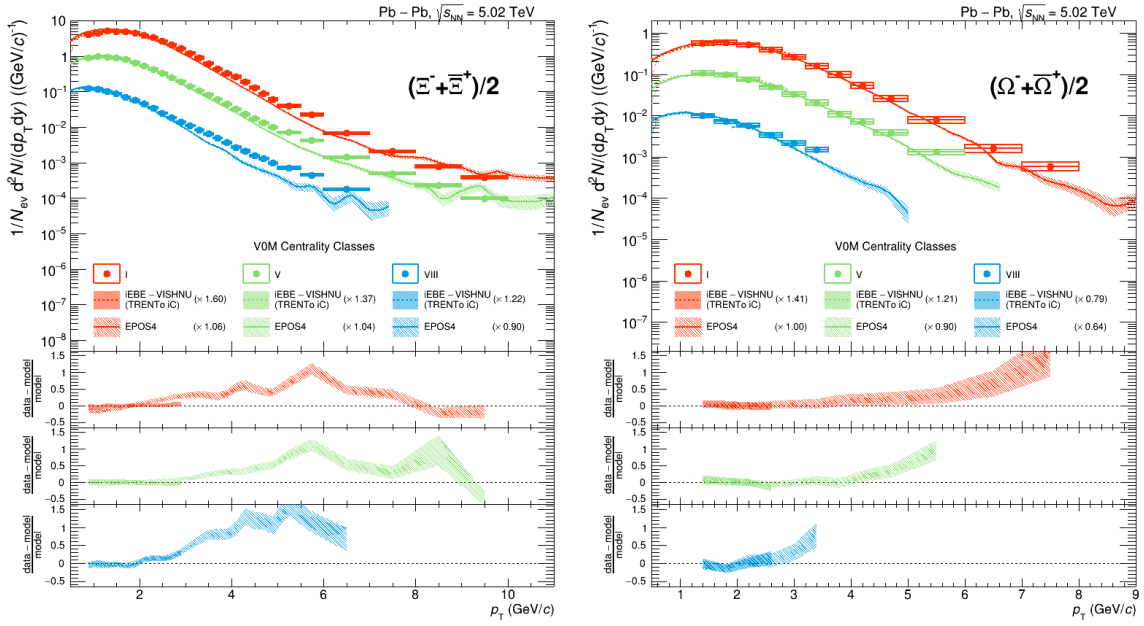

Fig. 5.18 Top: corrected p_T spectra for Ξ (left) and Ω (right) particles in the centrality classes I (red), IV (green) and VIII (blue). For each centrality classes, the predictions from the hybrid model iEBE–VISHNU with TRENTo initial conditions (dashed line) and the event generator EPOS4 (continuous line) are also reported. Bottom: normalized difference between data and model predictions are reported for the three centrality classes I, IV and VIII in different pads. The bands correspond to the uncertainty propagated from the ones of data and model predictions.

momentum regions, where quark or gluon fragmentation and parton coalescence are not the dominant source of particle production. The lower panels of Fig. 5.18 show that such a model is capable of describing properly the shape of the spectra of cascades. In terms of centrality, the agreement is better for central events than for the peripheral ones as it is conceivable for models based on a collective description of large systems featuring hydrodynamical behavior. Additional predictions are provided by the recently available event generator EPOS4 [177] (continuous lines). This is a general-purpose event generator which aims at describing the whole evolution of the collision system, starting from initial conditions, hard scattering (core) and underlying event (corona), statistical hadronization and post-freeze-out hadronic interactions. This model extends its predictions over a wide transverse momentum range: in the low p_{T} region the results are similar to the iEBE–VISHNU predictions, while at higher p_{T} the polynomial tail of the distribution models the perturbative part of the production cross-section. In the intermediate to high-p_{T} regions the agreement of the model to the data worsens progressively, though qualitatively the features in the measured spectra are correctly described. In particular, the model systematically underestimates the spectra, meaning that the predicted cascade spectra are softer than the measured ones. Due to the larger uncertainties for the Ω particle, the agreement between the EPOS4 calculation and the measured spectra is better than for the Ξ particle, even though the magnitude of their difference is similar for both of the particles. In general, the models under investigation show a rather good agreement with the measured spectral shape, taking into account the wide ranges in centrality and transverse momentum which are covered by the predictions.

5.10 Production yields and ratio to pions

The measured transverse momentum spectra are used to compute the integrated production yields per rapidity unit $\frac{\mathrm{d}N}{\mathrm{d}y}$ via a fit procedure which is similar to the one used for nuclei. The main difference with respect to what was discussed in Sec. 4.9 lies in the fitting function, since a Levy-Tsallis functional form is not suitable to describe the production spectra in Pb–Pb collisions. In large collision systems, particle spectra are usually described assuming a thermal production from an expanding source by using a Blast-Wave [178] approach. In this work, a good description of the production spectra up to a maximum transverse momentum of 5 GeV/c is obtained with a Blast-Wave function, whose functional form is defined by

$$\frac{1}{p_{\mathrm{T}}}\frac{\mathrm{d}N}{\mathrm{d}p_{\mathrm{T}}} = \int_0^R r m_{\mathrm{T}} I_0\left(\frac{p_{\mathrm{T}}\sinh\rho}{T_{\mathrm{k}}}\right) K_1\left(\frac{m_{\mathrm{T}}\cosh\rho}{T_{\mathrm{k}}}\right)\mathrm{d}r \tag{5.9}$$

Class	Centrality	dN/dy	
		Ξ	Ω ($\times 10^{-1}$)
I	0 – 10	$10.38 \pm 0.04 \pm 1.22$	$13.43 \pm 0.15 \pm 2.27$
II	10 – 20	$6.93 \pm 0.03 \pm 0.74$	$9.52 \pm 0.22 \pm 2.11$
III	20 – 30	$4.75 \pm 0.02 \pm 0.50$	$5.96 \pm 0.10 \pm 0.99$
IV	30 – 40	$3.16 \pm 0.02 \pm 0.35$	$4.06 \pm 0.07 \pm 0.70$
V	40 – 50	$1.91 \pm 0.01 \pm 0.21$	$2.51 \pm 0.04 \pm 0.40$
VI	50 – 60	$1.06 \pm 0.00 \pm 0.12$	$1.30 \pm 0.03 \pm 0.22$
VII	60 – 70	$0.51 \pm 0.00 \pm 0.05$	$0.54 \pm 0.01 \pm 0.08$
VIII	70 – 80	$0.22 \pm 0.00 \pm 0.02$	$0.22 \pm 0.01 \pm 0.04$
IX	80 – 90	$0.08 \pm 0.00 \pm 0.01$	
INEL > 0	0 – 90	$3.20 \pm 0.01 \pm 0.34$	$4.15 \pm 0.03 \pm 0.65$

Table 5.11 p_{T} integrated yields for the different species for each centrality class of the analysis. The statistical uncertainties are always negligible with respect to systematic uncertainties.

where I_0 and K_1 are modified Bessel functions, r is the distance between the particle and the center of the expanding system, R is the limiting radius of the system expansion, T_{k} is the temperature of the kinetic freeze-out and ρ is the velocity profile. The velocity profile is expressed as a function of the transverse expansion velocity of the system β_{T} as

$$\rho = \tanh^{-1}\left[\left(\frac{r}{R}\right)^{n}\beta_{\mathrm{T}}\right] . \tag{5.10}$$

$m_{\mathrm{T}} = (p_{\mathrm{T}}^2 + m_0^2)^{\frac{1}{2}}$ is the transverse mass of the particle of interest with PDG mass m_0. This parameterization is used to extrapolate the p_{T} spectra in the unmeasured region at low transverse momentum, leading to the measurement of the integrated production yield of cascades.

The systematic uncertainty associated to the extrapolation of the spectrum in the unmeasured regions is carried out with the same technique used for the nuclei analysis and described in 4.9. The production yields of both the Ξ and Ω particles in the centrality classes explored in this analysis are reported in Table 5.11. The values reported show clearly how the systematic uncertainties are largely dominant over the statistical ones for this analysis. As an example, for the INEL > 0 multiplicity class, the statistical uncertainty is lower than 1% for both the particle species, while systematic uncertainty accounts for 10% and 16% for Ξ and Ω baryons, respectively.

The ratio between the aforementioned yields and the yields of pions is an observable suitable to be compared with model predictions. In particular, the ratio between cascade and pion integrated yields for this work is reported in Fig. 5.19 as a function of the charged particle in the collision. This work (red markers) managed to extend the multiplicity coverage of the

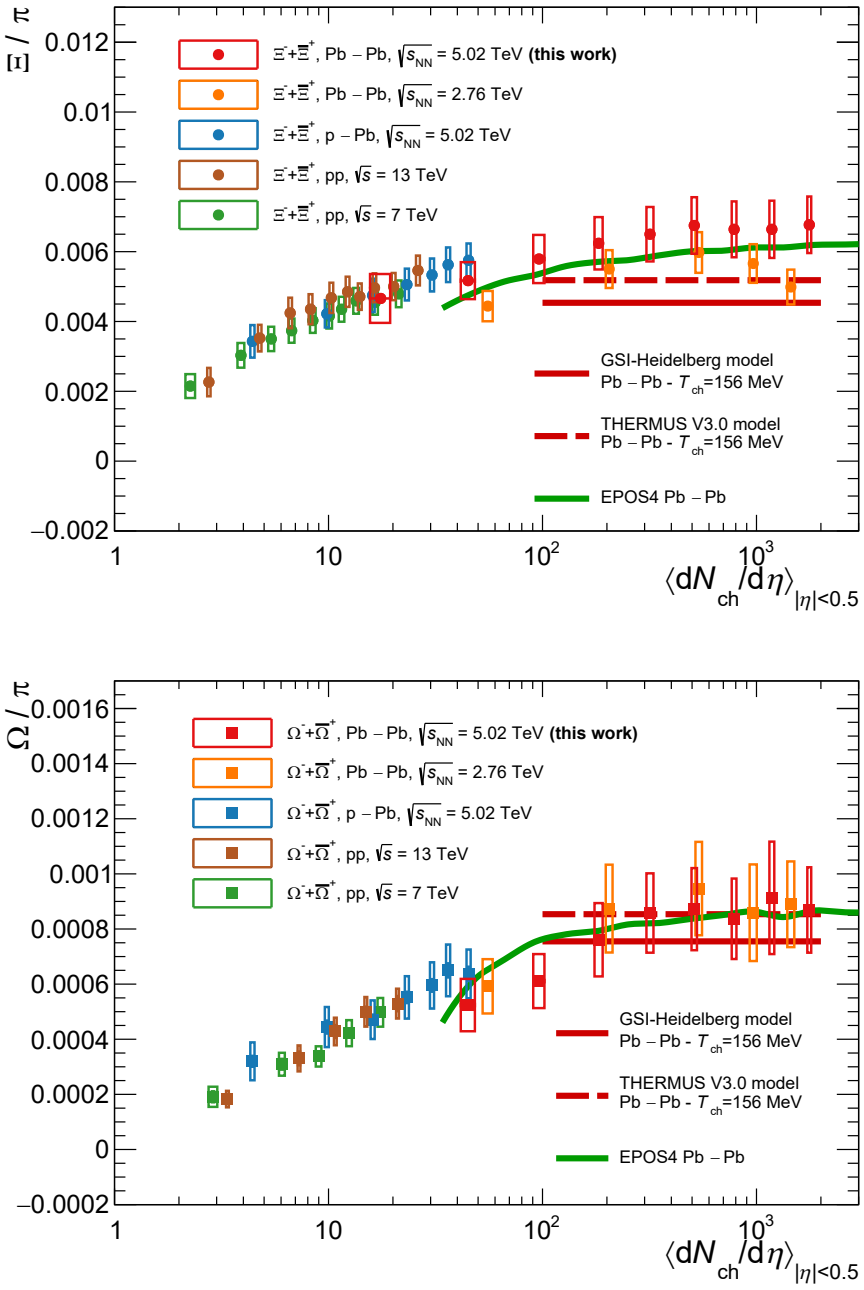

Fig. 5.19 Ratio between the p_{T} integrated yields of cascades and pions for Ξ (top) and Ω (bottom) particles in this work (red), in Pb–Pb collisions at 2.76 TeV [32, 37] (orange), in p–Pb collisions at 5.02 TeV [35, 36] (blue), in pp collisions at 13 TeV [172, 167] (brown) and in pp collisions at 7 TeV [33, 34] (green). The statistical uncertainties are represented by vertical bars while the systematic uncertainties are represented by boxes. The two red lines represent theoretical predictions of two different implementations of the SHM, while the green one is the prediction from the EPOS4 model.

previous ALICE measurement performed in Pb–Pb collisions at $\sqrt{s_{\rm NN}} = 2.76$ TeV: the Ξ result at low multiplicity corresponds to $\langle \frac{{\rm d}N_{\rm ch}}{{\rm d}\eta_{\rm lab}} \rangle$ values typically associated to high multiplicity pp and p–Pb collisions. At low Pb–Pb multiplicities, a good agreement between this result and the measurements performed in pp and p–Pb collisions is obtained, in particular for the Ξ baryon. At higher multiplicity, a saturation region is observed for semicentral and central Pb–Pb collisions. This high multiplicity saturation regime is also predicted by the SHM using a grand-canonical ensemble approach, such as GSI-Heidelberg [112] (continuous red line) and THERMUS [134] (dotted red line) models. From a quantitative point of view, the models show similar predictions and are able to describe properly the Ω saturation value, while underestimate the Ξ results. An additional prediction is provided by the EPOS4 model (green) described in Sec. 3.3, which implements a hydrodynamic core-corona approach followed by a UrQMD evolution of the system, after hadronization. This model is able to describe both the saturation region at high multiplicity and the mild decrease going towards peripheral Pb–Pb collisions, for both the Ξ and Ω baryons.

In general, a significant increase in the strange to non-strange hadron production is observed going from low multiplicity pp collisions to central Pb–Pb collisions. As well as for the nuclei to proton yield ratios discussed in Sec. 4.11, a smooth behavior as a function of the average charged particle multiplicity of the system $\langle \frac{{\rm d}N_{\rm ch}}{{\rm d}\eta_{\rm lab}} \rangle$ is present, without any dependence on the collision system or on the collision energy. This is an additional observation that particle ratios in hadronic collisions are not driven by the collision system but only by the density of charged particles produced in the final state.

Chapter 6

Conclusions

In this work the measurement of light nuclei and multi-strange baryon production in pp and Pb–Pb collisions using the ALICE apparatus have been presented.
The first part of this project was devoted to the study of the production of protons, deuterons, helions and their antimatter counterparts in pp collisions at $\sqrt{s} = 5.02$ TeV. Following the procedure described in Chapter 4, the transverse momentum spectra have been measured differentially in nine multiplicity classes for protons and deuterons, and in two for helions, in addition to the integrated multiplicity class spectrum (Fig. 4.20). Starting from the p_{T}-differential results, the integrated production yields $\frac{\mathrm{d}N}{\mathrm{d}y}$ and the average transverse momentum $\langle p_{\mathrm{T}} \rangle$ have been evaluated. An increasing suppression in the production yields of nuclei as a function of their mass number is observed (Fig. 4.22): this suppression also depends on the event multiplicity, being stronger as the multiplicity decreases. The $\langle p_{\mathrm{T}} \rangle$ values estimated in this work (Fig. 4.23) are in agreement with the measurements performed by ALICE in pp collisions at different center of mass energy and in p–Pb collisions, showing the expected mass ordering going from lighter nuclei (protons) to heavier ones (helions). The theoretical models attempting to explain the formation of light nuclei in high energy hadronic collisions, the statistical hadronization and the coalescence models, attempt to describe the production of nuclei as a function of the event multiplicity in terms of the ratio between the integrated yields of nuclei and those of protons, d/p, ^{3}He/p. The nuclei-to-proton ratios (Fig. 4.26) presented in this work constitute the most precise measurement performed in the low multiplicity region by the ALICE collaboration and are in very good agreement with the measurements previously performed by the experiment. Both the statistical hadronization model and the coalescence model predictions can describe the smooth increase of the nuclei-to-proton ratios as a function of multiplicity, starting from very different phenomenological model assumptions. Nevertheless, only the coalescence model is able to describe quantitatively the d/p over

the whole multiplicity coverage of the measurements. The ^{3}He/p is currently not reproduced by neither the statistical hadronization model, nor the coalescence model. Additionally, the coalescence parameters B_2 for deuterons and B_3 for helions were measured as a function of the multiplicity (Fig. 4.25) and compared to other ALICE measurements in small collision systems. As well as for the nuclei-to-proton ratio, the evolution with multiplicity is smooth, as predicted by the coalescence model. Anyway, a single parameterization of the coalescence model is not able to reproduce quantitatively the B_2 and the B_3 at the same time.

The second part of this work was focused on the analysis of the production of the multi-strange baryons Ξ and Ω, also called cascades, in Pb–Pb collisions at $\sqrt{s_{\rm NN}} = 5.02$ TeV. This dataset integrates the largest number of Pb–Pb events ever recorded by the ALICE experiment at the top Run2 energy for Pb–Pb collisions. In Chapter 5, the analysis strategy developed to evaluate the corrected $p_{\rm T}$ spectra of cascades (Fig. 5.17) was described. With such a large dataset, it was possible to exploit nine centrality classes, granting a dense scan in terms of the event multiplicity. Theoretical models based on hydrodynamic calculations, such as iEBE-VISHNU and EPOS4, are able to describe the bulk of cascade production at low $p_{\rm T}$ (Fig. 5.18), even though the results get worse at higher transverse momentum: the EPOS4 model, generally successful in describing the overall spectrum over few orders of magnitude, predicts softer spectra than the measured ones for $p_{\rm T} > 3$ GeV/c. Finally, the ratio between the production yields of cascades and pions, Ξ/π and Ω/π, have been measured as a function of multiplicity (Fig. 5.19). Thanks to the large number of centrality classes considered, the results from this work represents a key measurement in order to compare small and large collision systems, especially in the low Pb–Pb multiplicity region. This result extends the multiplicity coverage of the Pb–Pb measurement performed at $\sqrt{s_{\rm NN}} = 2.76$ TeV down to intermediate multiplicities usually measured in pp and p–Pb collisions. At high multiplicity, the saturation expected from the statistical hadronization model is observed, even though the models describe quantitatively only the Ω-to-π ratio, while they underestimate the Ξ-to-π one.

In general, the particle ratios for both the nuclei and cascade analyses and the coalescence parameter measurements showed a smooth evolution with the final state multiplicity, regardless of the collision system and energy. Even though there is no single model able to reproduce all these observables at the same time, this behavior suggests the presence of a common production mechanism for light-flavor particles in high energy physics which depends only on the multiplicity, thus on the size of the hadronizing system.

Currently ALICE is taking data in the LHC Run3 campaign with an upgraded detector which can better exploit the large luminosity provided by the accelerator facility and has a more flexible triggering system which allows to select events characterized by features which are

connected to specific physics observables. Nonetheless, given the precision and granularity of the results presented in this thesis, no groundbreaking improvement can be foreseen for these observables. The only measurement which will substantially benefit from the new data taking campaign will be the helion one, whereby a larger number of multiplicity classes would be achievable and a more constraining comparison with the theoretical models could be done. More importantly, a major improvement to the topics discussed in this work has to come from the theoretical side: within the current picture, in particular for the nuclei measurement, no model is capable of reproducing quantitatively at the same time different observables.

On the other hand, new measurements involving heavier nuclei, such as 4-helion, could complement the present results and challenge even more the theoretical predictions. At the same time, thanks to the upgraded Inner Tracking System, short-living charged strange particles could be efficiently detected in the new apparatus, opening the possibility to measure for the first time charged Σ baryons, thus completing the strangeness enhancement picture for light flavour hadrons.

Another valuable contribution may come from other experiments: in particular, the Beam Energy Scan (BES) program from the STAR experiment is aimed to explore the QCD phase diagram in a range characterized by non-vanishing baryo-chemical potential. In this region, which can not be accessed at the LHC energies, one can collect new insights on the properties of the phase transition between ordinary and QGP matter and the potential existence of a critical point can be explored.

In conclusion, this thesis work provided final results from the ALICE Run2 phase for light nuclei production in small collision systems and for multi-strange baryon production in heavy ion collisions. These results will constitute the new reference for future analysis efforts in the field of light flavour particle production studies, both in ALICE and in other experiments. At the same time, the legacy of these results will consists in a precise benchmark for the development and tuning of the phenomenological models.

References

[1] Shreyasi Acharya et al. Production of light (anti)nuclei in pp collisions at $\sqrt{s} =$ 5.02 TeV. *Eur. Phys. J. C*, 82(4):289, 2022.

[2] W. J. Stirling. QCD theory. *Int. J. Mod. Phys. A*, 20:5234–5243, 2005.

[3] Murray Gell-Mann. A Schematic Model of Baryons and Mesons. *Phys. Lett.*, 8:214–215, 1964.

[4] Michael E. Peskin and Daniel V. Schroeder. *An Introduction to quantum field theory*. Addison-Wesley, Reading, USA, 1995.

[5] Siegfried Bethke. Experimental tests of asymptotic freedom. *Prog. Part. Nucl. Phys.*, 58:351–386, 2007.

[6] Kenneth G. Wilson. Confinement of Quarks. *Phys. Rev. D*, 10:2445–2459, 1974.

[7] S. Durr et al. Ab-Initio Determination of Light Hadron Masses. *Science*, 322:1224–1227, 2008.

[8] P. A. Zyla et al. Review of Particle Physics. *PTEP*, 2020(8):083C01, 2020.

[9] K. Johnson. Hadron States in the MIT Bag Model. *Stud. Nat. Sci.*, 11:101–112, 1976.

[10] Mark G. Alford. Color superconducting quark matter. *Ann. Rev. Nucl. Part. Sci.*, 51:131–160, 2001.

[11] Takehiro Tanimoto, Wolfgang Bentz, and Ian C. Cloët. Massive Neutron Stars with a Color Superconducting Quark Matter Core. *Phys. Rev. C*, 101(5):055204, 2020.

[12] Tillmann Boeckel and Jurgen Schaffner-Bielich. A little inflation at the cosmological QCD phase transition. *Phys. Rev. D*, 85:103506, 2012.

[13] Eemeli Annala, Tyler Gorda, Aleksi Kurkela, Joonas Nättilä, and Aleksi Vuorinen. Evidence for quark-matter cores in massive neutron stars. *Nature Phys.*, 16(9):907–910, 2020.

[14] A. Li, Z. Y. Zhu, E. P. Zhou, J. M. Dong, J. N. Hu, and C. J. Xia. Neutron star equation of state: Quark mean-field (QMF) modeling and applications. *JHEAp*, 28:19–46, 2020.

[15] G. Gatoff and C. Y. Wong. Origin of the soft p(T) spectra. *Phys. Rev. D*, 46:997–1006, 1992.

[16] J. Adams et al. Identified hadron spectra at large transverse momentum in p+p and d+Au collisions at s(NN)**(1/2) = 200-GeV. *Phys. Lett. B*, 637:161–169, 2006.

[17] Betty Abelev et al. Pion, Kaon, and Proton Production in Central Pb–Pb Collisions at $\sqrt{s_{NN}} = 2.76$ TeV. *Phys. Rev. Lett.*, 109:252301, 2012.

[18] Shreyasi Acharya et al. Production of charged pions, kaons, and (anti-)protons in Pb-Pb and inelastic pp collisions at $\sqrt{s_{NN}}$ = 5.02 TeV. *Phys. Rev. C*, 101(4):044907, 2020.

[19] Burak Han Alver, Clement Gombeaud, Matthew Luzum, and Jean-Yves Ollitrault. Triangular flow in hydrodynamics and transport theory. *Phys. Rev. C*, 82:034913, 2010.

[20] Derek Teaney and Li Yan. Non linearities in the harmonic spectrum of heavy ion collisions with ideal and viscous hydrodynamics. *Phys. Rev. C*, 86:044908, 2012.

[21] K Aamodt et al. Elliptic flow of charged particles in Pb-Pb collisions at 2.76 TeV. *Phys. Rev. Lett.*, 105:252302, 2010.

[22] R. Stock, editor. *Relativistic Heavy Ion Physics*, volume 23 of *Landolt-Boernstein - Group I Elementary Particles, Nuclei and Atoms*. Springer, 2010.

[23] A. Andronic et al. Excitation function of elliptic flow in Au+Au collisions and the nuclear matter equation of state. *Phys. Lett. B*, 612:173–180, 2005.

[24] A Andronic et al. Transition from in-plane to out-of-plane azimuthal enhancement in Au + Au collisions. *Nucl. Phys. A*, 679:765–792, 2001.

[25] Scott McDonald, Chun Shen, Francois Fillion-Gourdeau, Sangyong Jeon, and Charles Gale. Hydrodynamic predictions for Pb+Pb collisions at 5.02 TeV. *Phys. Rev. C*, 95(6):064913, 2017.

[26] Wenbin Zhao, Hao-jie Xu, and Huichao Song. Collective flow in 2.76 A TeV and 5.02 A TeV Pb+Pb collisions. *Eur. Phys. J. C*, 77(9):645, 2017.

[27] Raimond Snellings. Elliptic Flow: A Brief Review. *New J. Phys.*, 13:055008, 2011.

[28] Johann Rafelski and Berndt Muller. Strangeness Production in the Quark - Gluon Plasma. *Phys. Rev. Lett.*, 48:1066, 1982. [Erratum: Phys.Rev.Lett. 56, 2334 (1986)].

[29] Olaf Kaczmarek and Felix Zantow. Static quark anti-quark interactions in zero and finite temperature QCD. I. Heavy quark free energies, running coupling and quarkonium binding. *Phys. Rev. D*, 71:114510, 2005.

[30] F. Antinori et al. Enhancement of hyperon production at central rapidity in 158-A-GeV/c Pb-Pb collisions. *J. Phys. G*, 32:427–442, 2006.

[31] B. I. Abelev et al. Enhanced strange baryon production in Au + Au collisions compared to p + p at s(NN)**(1/2) = 200-GeV. *Phys. Rev. C*, 77:044908, 2008.

[32] Betty Bezverkhny Abelev et al. Multi-strange baryon production at mid-rapidity in Pb-Pb collisions at $\sqrt{s_{NN}}$ = 2.76 TeV. *Phys. Lett. B*, 728:216–227, 2014. [Erratum: Phys.Lett.B 734, 409–410 (2014)].

[33] Jaroslav Adam et al. Enhanced production of multi-strange hadrons in high-multiplicity proton-proton collisions. *Nature Phys.*, 13:535–539, 2017.

[34] Shreyasi Acharya et al. Multiplicity dependence of light-flavor hadron production in pp collisions at $\sqrt{s}$ = 7 TeV. *Phys. Rev. C*, 99(2):024906, 2019.

[35] Jaroslav Adam et al. Multi-strange baryon production in p-Pb collisions at $\sqrt{s_{\mathrm{NN}}}$ = 5.02 TeV. *Phys. Lett. B*, 758:389–401, 2016.

[36] S. Acharya et al. Transverse momentum spectra and nuclear modification factors of charged particles in pp, p-Pb and Pb-Pb collisions at the LHC. *JHEP*, 11:013, 2018.

[37] Jaroslav Adam et al. Centrality dependence of the nuclear modification factor of charged pions, kaons, and protons in Pb-Pb collisions at $\sqrt{s_{\mathrm{NN}}} = 2.76$ TeV. *Phys. Rev. C*, 93(3):034913, 2016.

[38] T. Pierog, Iu. Karpenko, J. M. Katzy, E. Yatsenko, and K. Werner. EPOS LHC: Test of collective hadronization with data measured at the CERN Large Hadron Collider. *Phys. Rev. C*, 92(3):034906, 2015.

[39] Christian Bierlich and Jesper Roy Christiansen. Effects of color reconnection on hadron flavor observables. *Phys. Rev. D*, 92(9):094010, 2015.

[40] Torbjorn Sjostrand, Stephen Mrenna, and Peter Z. Skands. A Brief Introduction to PYTHIA 8.1. *Comput. Phys. Commun.*, 178:852–867, 2008.

[41] J. W. Cronin, Henry J. Frisch, M. J. Shochet, J. P. Boymond, R. Mermod, P. A. Piroue, and Richard L. Sumner. Production of hadrons with large transverse momentum at 200, 300, and 400 GeV. *Phys. Rev. D*, 11:3105–3123, 1975.

[42] Nestor Armesto. Nuclear shadowing. *J. Phys. G*, 32:R367–R394, 2006.

[43] S. Acharya et al. Measurement of D^0, D^+, D^{*+} and D_s^+ production in Pb-Pb collisions at $\sqrt{s_{\mathrm{NN}}} = 5.02$ TeV. *JHEP*, 10:174, 2018.

[44] Yuri L. Dokshitzer, Valery A. Khoze, and S. I. Troian. On specific QCD properties of heavy quark fragmentation ('dead cone'). *J. Phys. G*, 17:1602–1604, 1991.

[45] S. Acharya et al. Direct observation of the dead-cone effect in quantum chromodynamics. *Nature*, 605(7910):440–446, 2022. [Erratum: Nature 607, E22 (2022)].

[46] Shreyasi Acharya et al. Measurement of prompt D^0, D^+, D^{*+}, and $\mathrm{D}_{\mathrm{S}}^+$ production in p–Pb collisions at $\sqrt{s_{\mathrm{NN}}}$ = 5.02 TeV. *JHEP*, 12:092, 2019.

[47] Shreyasi Acharya et al. Prompt D^0, D^+, and D^{*+} production in Pb–Pb collisions at $\sqrt{s_{\mathrm{NN}}}$ = 5.02 TeV. *JHEP*, 01:174, 2022.

[48] T. Matsui and H. Satz. J/ψ Suppression by Quark-Gluon Plasma Formation. *Phys. Lett. B*, 178:416–422, 1986.

[49] Agnes Mocsy and Peter Petreczky. Can quarkonia survive deconfinement? *Phys. Rev. D*, 77:014501, 2008.

[50] E. Hückel. *Zur Theorie der Elektrolyte*, pages 199–276. Springer Berlin Heidelberg, Berlin, Heidelberg, 1924.

[51] Xiaojian Du and Ralf Rapp. Sequential Regeneration of Charmonia in Heavy-Ion Collisions. *Nucl. Phys. A*, 943:147–158, 2015.

[52] Vardan Khachatryan et al. Suppression and azimuthal anisotropy of prompt and nonprompt J/ψ production in PbPb collisions at $\sqrt{s_{\mathrm{NN}}} = 2.76$ TeV. *Eur. Phys. J. C*, 77(4):252, 2017.

[53] Jaroslav Adam et al. Differential studies of inclusive J/ψ and ψ(2S) production at forward rapidity in Pb-Pb collisions at $\sqrt{s_{\mathrm{NN}}} = 2.76$ TeV. *JHEP*, 05:179, 2016.

[54] Jaroslav Adam et al. Centrality dependence of ψ(2S) suppression in p-Pb collisions at $\sqrt{s_{\mathrm{NN}}}$ = 5.02 TeV. *JHEP*, 06:050, 2016.

[55] Betty Bezverkhny Abelev et al. Suppression of ψ(2S) production in p-Pb collisions at $\sqrt{s_{\mathrm{NN}}}$ = 5.02 TeV. *JHEP*, 12:073, 2014.

[56] Shreyasi Acharya et al. Υ production and nuclear modification at forward rapidity in Pb-Pb collisions at sNN=5.02TeV. *Phys. Lett. B*, 822:136579, 2021.

[57] Shreyasi Acharya et al. Υ production in p-Pb collisions at $\sqrt{s_{NN}}$=8.16 TeV. *Phys. Lett. B*, 806:135486, 2020.

[58] A. Adare et al. J/ψ suppression at forward rapidity in Au+Au collisions at $\sqrt{s_{NN}} =$ 200 GeV. *Phys. Rev. C*, 84:054912, 2011.

[59] Jaroslav Adam et al. Measurement of jet quenching with semi-inclusive hadron-jet distributions in central Pb-Pb collisions at $\sqrt{s_{\mathrm{NN}}} = 2.76$ TeV. *JHEP*, 09:170, 2015.

[60] Shreyasi Acharya et al. Measurements of inclusive jet spectra in pp and central Pb-Pb collisions at $\sqrt{s_{\mathrm{NN}}}$ = 5.02 TeV. *Phys. Rev. C*, 101(3):034911, 2020.

[61] Peter Zeiler Skands. Tuning Monte Carlo Generators: The Perugia Tunes. *Phys. Rev. D*, 82:074018, 2010.

[62] S. Acharya et al. Measurement of Z^0-boson production at large rapidities in Pb-Pb collisions at $\sqrt{s_{\mathrm{NN}}} = 5.02$ TeV. *Phys. Lett. B*, 780:372–383, 2018.

[63] Shreyasi Acharya et al. Z-boson production in p-Pb collisions at $\sqrt{s_{\mathrm{NN}}} = 8.16$ TeV and Pb-Pb collisions at $\sqrt{s_{\mathrm{NN}}} = 5.02$ TeV. *JHEP*, 09:076, 2020.

[64] Jaroslav Adam et al. Direct photon production in Pb-Pb collisions at $\sqrt{s_{NN}} = 2.76$ TeV. *Phys. Lett. B*, 754:235–248, 2016.

[65] Jean-François Paquet, Chun Shen, Gabriel S. Denicol, Matthew Luzum, Björn Schenke, Sangyong Jeon, and Charles Gale. Production of photons in relativistic heavy-ion collisions. *Phys. Rev. C*, 93(4):044906, 2016.

[66] Hendrik van Hees, Min He, and Ralf Rapp. Pseudo-critical enhancement of thermal photons in relativistic heavy-ion collisions? *Nucl. Phys. A*, 933:256–271, 2015.

[67] Rupa Chatterjee, Hannu Holopainen, Thorsten Renk, and Kari J. Eskola. Collision centrality and τ_0 dependence of the emission of thermal photons from fluctuating initial state in ideal hydrodynamic calculation. *Phys. Rev. C*, 85:064910, 2012.

[68] O. Linnyk, V. Konchakovski, T. Steinert, W. Cassing, and E. L. Bratkovskaya. Hadronic and partonic sources of direct photons in relativistic heavy-ion collisions. *Phys. Rev. C*, 92(5):054914, 2015.

[69] Lyndon Evans and Philip Bryant. LHC Machine. *JINST*, 3:S08001, 2008.

[70] K. Aamodt et al. The ALICE experiment at the CERN LHC. *JINST*, 3:S08002, 2008.

[71] Julie Haffner. The CERN accelerator complex. Complexe des accélérateurs du CERN. 2013. General Photo.

[72] B. Adeva et al. The Construction of the L3 Experiment. *Nucl. Instrum. Meth. A*, 289:35–102, 1990.

[73] G. Dellacasa et al. *ALICE Inner Tracking System (ITS): Technical Design Report*. Technical design report. ALICE. CERN, Geneva, 1999.

[74] K Aamodt et al. Alignment of the ALICE Inner Tracking System with cosmic-ray tracks. *JINST*, 5:P03003, 2010.

[75] J. Alme et al. The ALICE TPC, a large 3-dimensional tracking device with fast readout for ultra-high multiplicity events. *Nucl. Instrum. Meth. A*, 622:316–367, 2010.

[76] J. Alme, Y. Andres, H. Appelshäuser, S. Bablok, N. Bialas, R. Bolgen, U. Bonnes, R. Bramm, P. Braun-Munzinger, R. Campagnolo, P. Christiansen, A. Dobrin, C. Engster, D. Fehlker, Y. Foka, U. Frankenfeld, J.J. Gaardhøje, C. Garabatos, P. Glässel, C. Gonzalez Gutierrez, P. Gros, H.-A. Gustafsson, H. Helstrup, M. Hoch, M. Ivanov, R. Janik, A. Junique, A. Kalweit, R. Keidel, S. Kniege, M. Kowalski, D.T. Larsen, Y. Lesenechal, P. Lenoir, N. Lindegaard, C. Lippmann, M. Mager, M. Mast, A. Matyja, M. Munkejord, L. Musa, B.S. Nielsen, V. Nikolic, H. Oeschler, E.K. Olsen, A. Oskarsson, L. Osterman, M. Pikna, A. Rehman, G. Renault, R. Renfordt, S. Rossegger, D. Röhrich, K. Røed, M. Richter, G. Rueshmann, A. Rybicki, H. Sann, H.-R. Schmidt, M. Siska, B. Sitár, C. Soegaard, H.-K. Soltveit, D. Soyk, J. Stachel, H. Stelzer, E. Stenlund, R. Stock, P. Strmeň, I. Szarka, K. Ullaland, D. Vranic, R. Veenhof, J. Westergaard, J. Wiechula, and B. Windelband. The ALICE TPC, a large 3-dimensional tracking device with fast readout for ultra-high multiplicity events. *Nuclear Instruments and Methods in Physics Research Section A: Accelerators, Spectrometers, Detectors and Associated Equipment*, 622(1):316–367, oct 2010.

[77] Francesca Carnesecchi. Performance of the ALICE Time-Of-Flight detector at the LHC. *JINST*, 14(06):C06023, 2019.

[78] Jaroslav Adam et al. Determination of the event collision time with the ALICE detector at the LHC. *Eur. Phys. J. Plus*, 132(2):99, 2017.

[79] E. Abbas et al. Performance of the ALICE VZERO system. *JINST*, 8:P10016, 2013.

[80] Christian Wolfgang Fabjan, L Jirdén, V Lindestruth, Lodovico Riccati, D Rorich, Pierre Van de Vyvre, O Villalobos Baillie, and Hans de Groot. *ALICE trigger data-acquisition high-level trigger and control system: Technical Design Report*. Technical design report. ALICE. CERN, Geneva, 2004.

[81] Mikolaj Krzewicki, David Rohr, Sergey Gorbunov, Timo Breitner, Johannes Lehrbach, Volker Lindenstruth, Dario Berzano, and for the ALICE Collaboration. The alice high level trigger: status and plans. *Journal of Physics: Conference Series*, 664(8):082023, dec 2015.

[82] Jamie Shiers. The Worldwide LHC Computing Grid (worldwide LCG). *Comput. Phys. Commun.*, 177:219–223, 2007.

[83] Miklos Gyulassy and Xin-Nian Wang. HIJING 1.0: A Monte Carlo program for parton and particle production in high-energy hadronic and nuclear collisions. *Comput. Phys. Commun.*, 83:307, 1994.

[84] Torbjorn Sjostrand, Stephen Mrenna, and Peter Z. Skands. PYTHIA 6.4 Physics and Manual. *JHEP*, 05:026, 2006.

[85] René Brun, F Bruyant, Federico Carminati, Simone Giani, M Maire, A McPherson, and L Patrick, Gand Urban. *GEANT: Detector Description and Simulation Tool; Oct 1994*. CERN Program Library. CERN, Geneva, 1993. Long Writeup W5013.

[86] S. Agostinelli et al. GEANT4–a simulation toolkit. *Nucl. Instrum. Meth. A*, 506:250–303, 2003.

[87] A Ferrari, Paola R Sala, A Fassò, and Johannes Ranft. *FLUKA: A multi-particle transport code (program version 2005)*. CERN Yellow Reports: Monographs. CERN, Geneva, 2005.

[88] Shreyasi Acharya et al. Pseudorapidity distributions of charged particles as a function of mid- and forward rapidity multiplicities in pp collisions at $\sqrt{s}$ = 5.02, 7 and 13 TeV. *Eur. Phys. J. C*, 81(7):630, 2021.

[89] Prashant Shukla. The Glauber model and the heavy ion reaction cross-section. *Phys. Rev. C*, 67:054607, 2003.

[90] Betty Abelev et al. Centrality determination of Pb-Pb collisions at $\sqrt{s_{NN}}$ = 2.76 TeV with ALICE. *Phys. Rev. C*, 88(4):044909, 2013.

[91] M. Martinez Pedreira, C. Grigoras, and V. Yurchenko. JAliEn: the new ALICE high-performance and high-scalability Grid framework. *EPJ Web Conf.*, 214:03037, 2019.

[92] R. Brun, P. Buncic, F. Carminati, A. Morsch, F. Rademakers, and K. Safarik. Computing in alice. *Nuclear Instruments and Methods in Physics Research Section A: Accelerators, Spectrometers, Detectors and Associated Equipment*, 502(2):339–346, 2003. Proceedings of the VIII International Workshop on Advanced Computing and Analysis Techniques in Physics Research.

[93] R. Brun and F. Rademakers. ROOT: An object oriented data analysis framework. *Nucl. Instrum. Meth. A*, 389:81–86, 1997.

[94] R. Fruhwirth. Application of Kalman filtering to track and vertex fitting. *Nucl. Instrum. Meth. A*, 262:444–450, 1987.

[95] Betty Bezverkhny Abelev et al. Performance of the ALICE Experiment at the CERN LHC. *Int. J. Mod. Phys. A*, 29:1430044, 2014.

[96] Walter Blum, Luigi Rolandi, and Werner Riegler. *Particle detection with drift chambers*. Particle Acceleration and Detection. Springer, 2008.

[97] Joseph I. Kapusta. Mechanisms for deuteron production in relativistic nuclear collisions. *Phys. Rev. C*, 21:1301–1310, 1980.

[98] F. Becattini. An Introduction to the Statistical Hadronization Model. In *International School on Quark-Gluon Plasma and Heavy Ion Collisions: past, present, future*, 1 2009.

[99] S. Z. Belenkij and L. D. Landau. Hydrodynamic theory of multiple production of particles. *Usp. Fiz. Nauk*, 56:309, 1955.

[100] S. A. Bass et al. Microscopic models for ultrarelativistic heavy ion collisions. *Prog. Part. Nucl. Phys.*, 41:255–369, 1998.

[101] M. Bleicher et al. Relativistic hadron hadron collisions in the ultrarelativistic quantum molecular dynamics model. *J. Phys. G*, 25:1859–1896, 1999.

[102] Klaus Werner. On a deep connection between factorization and saturation: new insight into modeling high-energy proton-proton and nucleus-nucleus scattering in the EPOS4 framework. 1 2023.

[103] H. H. Gutbrod, A. Sandoval, P. J. Johansen, Arthur M. Poskanzer, J. Gosset, W. G. Meyer, G. D. Westfall, and R. Stock. Final State Interactions in the Production of Hydrogen and Helium Isotopes by Relativistic Heavy Ions on Uranium. *Phys. Rev. Lett.*, 37:667–670, 1976.

[104] K Aamodt et al. Two-pion Bose-Einstein correlations in pp collisions at $\sqrt{s} = 900$ GeV. *Phys. Rev. D*, 82:052001, 2010.

[105] C. Van Der Leun and C. Alderliesten. The deuteron binding energy. *Nucl. Phys. A*, 380:261–269, 1982.

[106] Peter J. Mohr, David B. Newell, and Barry N. Taylor. CODATA Recommended Values of the Fundamental Physical Constants: 2014. *Rev. Mod. Phys.*, 88(3):035009, 2016.

[107] J. E. Purcell and C. G. Sheu. Nuclear Data Sheets for A = 3. *Nucl. Data Sheets*, 130:1–20, 2015.

[108] K. Aamodt et al. Two-pion Bose-Einstein correlations in central Pb-Pb collisions at $\sqrt{s_{NN}} = 2.76$ TeV. *Phys. Lett. B*, 696:328–337, 2011.

[109] Measurement of two-particle Bose-Einstein momentum correlations and their Levy parameters at $\sqrt{s_{\rm NN}} = 5.02$ TeV PbPb collisions. Technical report, CERN, Geneva, 2022.

[110] Francesca Bellini and Alexander Philipp Kalweit. Testing production scenarios for (anti-)(hyper-)nuclei and exotica at energies available at the CERN Large Hadron Collider. *Phys. Rev. C*, 99(5):054905, 2019.

[111] Kai-Jia Sun, Che Ming Ko, and Benjamin Dönigus. Suppression of light nuclei production in collisions of small systems at the Large Hadron Collider. *Phys. Lett. B*, 792:132–137, 2019.

[112] Anton Andronic, Peter Braun-Munzinger, Krzysztof Redlich, and Johanna Stachel. Decoding the phase structure of QCD via particle production at high energy. *Nature*, 561(7723):321–330, 2018.

[113] Volodymyr Vovchenko, Benjamin Dönigus, and Horst Stoecker. Canonical statistical model analysis of p-p , p -Pb, and Pb-Pb collisions at energies available at the CERN Large Hadron Collider. *Phys. Rev. C*, 100(5):054906, 2019.

[114] Fred Cooper and Graham Frye. Comment on the Single Particle Distribution in the Hydrodynamic and Statistical Thermodynamic Models of Multiparticle Production. *Phys. Rev. D*, 10:186, 1974.

[115] Huichao Song and Ulrich W. Heinz. Causal viscous hydrodynamics in 2+1 dimensions for relativistic heavy-ion collisions. *Phys. Rev. C*, 77:064901, 2008.

[116] B. I. Abelev et al. Centrality dependence of charged hadron and strange hadron elliptic flow from s(NN)**(1/2) = 200-GeV Au + Au collisions. *Phys. Rev. C*, 77:054901, 2008.

[117] T. Skyrme. The effective nuclear potential. *Nucl. Phys.*, 9:615–634, 1959.

[118] P. Desgrolard, M. Giffon, E. Martynov, and E. Predazzi. The additive quark model revisited: Hadron and photon induced cross-sections. *Eur. Phys. J. C*, 9:623–631, 1999.

[119] K. Werner, Iu. Karpenko, M. Bleicher, T. Pierog, and S. Porteboeuf-Houssais. Jets, Bulk Matter, and their Interaction in Heavy Ion Collisions at Several TeV. *Phys. Rev. C*, 85:064907, 2012.

[120] K. Werner. Lambda-to-Kaon Ratio Enhancement in Heavy Ion Collisions at Several TeV. *Phys. Rev. Lett.*, 109:102301, 2012.

[121] A. G. Knospe, C. Markert, K. Werner, J. Steinheimer, and M. Bleicher. Hadronic resonance production and interaction in partonic and hadronic matter in the EPOS3 model with and without the hadronic afterburner UrQMD. *Phys. Rev. C*, 93(1):014911, 2016.

[122] Volodymyr Vovchenko, Benjamin Dönigus, and Horst Stoecker. Multiplicity dependence of light nuclei production at LHC energies in the canonical statistical model. *Phys. Lett.*, B785:171–174, 2018.

[123] Michal Petrán, Jean Letessier, Vojtěch Petráček, and Johann Rafelski. Hadron production and quark-gluon plasma hadronization in Pb-Pb collisions at $\sqrt{s_{NN}} = 2.76$ TeV. *Phys. Rev. C*, 88(3):034907, 2013.

[124] Jaroslav Adam et al. Production of light nuclei and anti-nuclei in pp and Pb-Pb collisions at energies available at the CERN Large Hadron Collider. *Phys. Rev. C*, 93(2):024917, 2016.

[125] Jaroslav Adam et al. ${}^{3}_{\Lambda}\mathrm{H}$ and ${}^{3}_{\bar{\Lambda}}\overline{\mathrm{H}}$ production in Pb-Pb collisions at $\sqrt{s_{\mathrm{NN}}} = 2.76$ TeV. *Phys. Lett. B*, 754:360–372, 2016.

[126] Shreyasi Acharya et al. Production of ${}^{4}\mathrm{He}$ and ${}^{4}\overline{\mathrm{He}}$ in Pb-Pb collisions at $\sqrt{s_{\mathrm{NN}}} =$ 2.76 TeV at the LHC. *Nucl. Phys. A*, 971:1–20, 2018.

[127] Shreyasi Acharya et al. Production of deuterons, tritons, ${}^{3}\mathrm{He}$ nuclei and their antinuclei in pp collisions at $\sqrt{s} = 0.9$, 2.76 and 7 TeV. *Phys. Rev. C*, 97(2):024615, 2018.

[128] Shreyasi Acharya et al. Production of (anti-)${}^{3}\mathrm{He}$ and (anti-)${}^{3}\mathrm{H}$ in p-Pb collisions at $\sqrt{s_{\mathrm{NN}}} = 5.02$ TeV. *Phys. Rev. C*, 101(4):044906, 2020.

[129] Jaroslav Adam et al. Centrality dependence of pion freeze-out radii in Pb-Pb collisions at $\sqrt{s_{NN}} = 2.76$ TeV. *Phys. Rev. C*, 93(2):024905, 2016.

[130] Betty Abelev et al. Centrality dependence of π, K, p production in Pb-Pb collisions at $\sqrt{s_{NN}} = 2.76$ TeV. *Phys. Rev. C*, 88:044910, 2013.

[131] Jaroslav Adam et al. Measurement of pion, kaon and proton production in proton–proton collisions at $\sqrt{s} = 7$ TeV. *Eur. Phys. J. C*, 75(5):226, 2015.

[132] Betty Bezverkhny Abelev et al. K^0_S and Λ production in Pb-Pb collisions at $\sqrt{s_{NN}} =$ 2.76 TeV. *Phys. Rev. Lett.*, 111:222301, 2013.

[133] Betty Bezverkhny Abelev et al. $\mathrm{K}^{*}(892)^{0}$ and $\phi(1020)$ production in Pb-Pb collisions at $\sqrt{sNN} = 2.76$ TeV. *Phys. Rev. C*, 91:024609, 2015.

[134] S. Wheaton and J. Cleymans. THERMUS: A Thermal model package for ROOT. *Comput. Phys. Commun.*, 180:84–106, 2009.

[135] Giorgio Torrieri, S. Steinke, Wojciech Broniowski, Wojciech Florkowski, Jean Letessier, and Johann Rafelski. SHARE: Statistical hadronization with resonances. *Comput. Phys. Commun.*, 167:229–251, 2005.

[136] Vytautas Vislavicius and Alexander Kalweit. Multiplicity dependence of light flavour hadron production at lhc energies in the strangeness canonical suppression picture, 2016.

[137] Betty Bezverkhny Abelev et al. Multiplicity Dependence of Pion, Kaon, Proton and Lambda Production in p-Pb Collisions at $\sqrt{s_{NN}} = 5.02$ TeV. *Phys. Lett. B*, 728:25–38, 2014.

[138] Jaroslav Adam et al. Production of $\mathrm{K}^{*}(892)^{0}$ and $\phi(1020)$ in p–Pb collisions at $\sqrt{s_{\mathrm{NN}}}$ = 5.02 TeV. *Eur. Phys. J. C*, 76(5):245, 2016.

[139] J. Aichelin and K. Werner. Centrality Dependence of Strangeness Enhancement in Ultrarelativistic Heavy Ion Collisions: A Core-Corona Effect. *Phys. Rev. C*, 79:064907, 2009. [Erratum: Phys.Rev.C 81, 029902 (2010)].

[140] Shreyasi Acharya et al. Evidence of rescattering effect in Pb-Pb collisions at the LHC through production of $K^*(892)^0$ and $\phi(1020)$ mesons. *Phys. Lett. B*, 802:135225, 2020.

[141] Chun Shen, Zhi Qiu, Huichao Song, Jonah Bernhard, Steffen Bass, and Ulrich Heinz. The iEBE-VISHNU code package for relativistic heavy-ion collisions. *Comput. Phys. Commun.*, 199:61–85, 2016.

[142] Huichao Song, Steffen Bass, and Ulrich W. Heinz. Spectra and elliptic flow for identified hadrons in 2.76A TeV Pb + Pb collisions. *Phys. Rev. C*, 89(3):034919, 2014.

[143] H. J. Drescher, M. Hladik, S. Ostapchenko, T. Pierog, and K. Werner. Parton based Gribov-Regge theory. *Phys. Rept.*, 350:93–289, 2001.

[144] Klaus Werner. Core-corona separation in ultra-relativistic heavy ion collisions. *Phys. Rev. Lett.*, 98:152301, 2007.

[145] Peter Skands, Stefano Carrazza, and Juan Rojo. Tuning PYTHIA 8.1: the Monash 2013 Tune. *Eur. Phys. J. C*, 74(8):3024, 2014.

[146] Shreyasi Acharya et al. Measurement of deuteron spectra and elliptic flow in Pb–Pb collisions at $\sqrt{s_{\rm NN}}$ = 2.76 TeV at the LHC. *Eur. Phys. J. C*, 77(10):658, 2017.

[147] Roger J. Barlow and Christine Beeston. Fitting using finite Monte Carlo samples. *Comput. Phys. Commun.*, 77:219–228, 1993.

[148] Shreyasi Acharya et al. Multiplicity dependence of (anti-)deuteron production in pp collisions at $\sqrt{s}$ = 7 TeV. *Phys. Lett. B*, 794:50–63, 2019.

[149] Wouter Verkerke and David P. Kirkby. The RooFit toolkit for data modeling. *eConf*, C0303241:MOLT007, 2003.

[150] V. Uzhinsky, J. Apostolakis, A. Galoyan, G. Folger, V. M. Grichine, V. N. Ivanchenko, and D. H. Wright. Antinucleus-nucleus cross sections implemented in Geant4. *Phys. Lett. B*, 705:235–239, 2011.

[151] P. Schwaller, M. Pepin, B. Favier, C. Richard-Serre, David F. Measday, and P. U. Renberg. PROTON TOTAL CROSS-SECTIONS ON H-1, H-2, HE-4, BE-9, C AND O IN THE ENERGY RANGE 180-MEV TO 560-MEV. *Nucl. Phys. A*, 316:317–344, 1979.

[152] W. Bauhoff. Tables of reaction and total cross sections for proton-nucleus scattering below 1 GeV. *Atom. Data Nucl. Data Tabl.*, 35:429–447, 1986.

[153] B. M. Bobchenko et al. MEASUREMENT OF TOTAL INELASTIC CROSS-SECTIONS FROM PROTON INTERACTIONS WITH NUCLEI IN THE MOMENTUM RANGE FROM 5-GeV/c TO 9-GeV/c AND pi- MESONS WITH NUCLEI IN THE MOMENTUM RANGE FROM 1.75-GeV/c TO 6.5-GeV/c. *Sov. J. Nucl. Phys.*, 30:805, 1979.

[154] J. Jaros, A. Wagner, L. Anderson, O. Chamberlain, R. Z. Fuzesy, J. Gallup, W. Gorn, L. Schroeder, S. Shannon, G. Shapiro, and H. Steiner. Nucleus-nucleus total cross sections for light nuclei at 1.55 and 2.89 gev/c per nucleon. *Phys. Rev. C*, 18:2273–2292, Nov 1978.

[155] A. Bianconi et al. Measurement of the antiproton–nucleus annihilation cross section at 5.3 MeV. *Phys. Lett. B*, 704:461–466, 2011.

[156] V. F. Kuzichev, Yu. B. Lepikhin, and V. A. Smirnitsky. The Anti-proton - nuclei annihilation cross-section at the momentum range from 0.70-GeV/c to 2.5-GeV/c. *Nucl. Phys. A*, 576:581–602, 1994.

[157] K. Nakamura, J. Chiba, T. Fujii, H. Iwasaki, T. Kageyama, S. Kuribayashi, T. Sumiyoshi, T. Takeda, H. Ikeda, and Y. Takada. Absorption and forward scattering of antiprotons by c, al, and cu nuclei in the region 470-880 mev/c. *Phys. Rev. Lett.*, 52:731–734, Feb 1984.

[158] A. Auce, R. F. Carlson, A. J. Cox, A. Ingemarsson, R. Johansson, P. U. Renberg, O. Sundberg, and G. Tibell. Reaction cross sections for 38, 65, and 97 mev deuterons on targets from ^{9}Be to ^{208}Pb. *Phys. Rev. C*, 53:2919–2925, Jun 1996.

[159] A. Ingemarsson et al. Reaction cross sections of intermediate energy 3 He-particles on targets from 9 Be to 208 Pb. *Nucl. Phys. A*, 696:3–30, 2001.

[160] A. Auce, R. F. Carlson, A. J. Cox, A. Ingemarsson, R. Johansson, P. U. Renberg, O. Sundberg, G. Tibell, and R. Zorro. Reaction cross sections for 75-190 MeV alpha particles on targets from C-12 to Pb-208. *Phys. Rev. C*, 50:871–879, 1994.

[161] Q. Yan, V. Choutko, A. Oliva, and M. Paniccia. Measurements of nuclear interaction cross sections with the Alpha Magnetic Spectrometer on the International Space Station. *Nucl. Phys. A*, 996:121712, 2020.

[162] S. P. Denisov, S. V. Donskov, Yu. P. Gorin, V. A. Kachanov, V. M. Kutjin, A. I. Petrukhin, Yu. D. Prokoshkin, E. A. Razuvaev, R. S. Shuvalov, and D. A. Stojanova. Measurements of anti-deuteron absorption and stripping cross sections at the momentum 13.3 gev/c. *Nucl. Phys. B*, 31:253–260, 1971.

[163] F. G. Binon et al. Absorption cross-sections of 25 gev/c antideuterons in li, c, al, cu and pb. *Phys. Lett. B*, 31:230–232, 1970.

[164] Shreyasi Acharya et al. Measurement of the low-energy antideuteron inelastic cross section. *Phys. Rev. Lett.*, 125(16):162001, 2020.

[165] Shreyasi Acharya et al. Production of light (anti)nuclei in pp collisions at $\sqrt{s}$ = 13 TeV. *JHEP*, 01:106, 2022.

[166] S. Acharya et al. (Anti-)deuteron production in pp collisions at $\sqrt{s} = 13$ TeV. *Eur. Phys. J. C*, 80(9):889, 2020.

[167] Shreyasi Acharya et al. Multiplicity dependence of π, K, and p production in pp collisions at $\sqrt{s} = 13$ TeV. *Eur. Phys. J. C*, 80(8):693, 2020.

[168] S. Acharya et al. (Anti-)deuteron production in pp collisions at $\sqrt{s} = 13$ TeV. *Eur. Phys. J. C*, 80(9):889, 2020.

[169] Shreyasi Acharya et al. Multiplicity dependence of (anti-)deuteron production in pp collisions at $\sqrt{s} = 7$ TeV. *Phys. Lett.*, B794:50–63, 2019.

[170] Shreyasi Acharya et al. Production of deuterons, tritons, ^{3}He nuclei and their antinuclei in pp collisions at $\sqrt{s} = 0.9$, 2.76 and 7 TeV. *Phys. Rev.*, C97(2):024615, 2018.

[171] Shreyasi Acharya et al. Multiplicity dependence of light (anti-)nuclei production in p-Pb collisions at $\sqrt{s_{\rm NN}} = 5.02$ TeV. *Phys. Lett.*, B800:135043, 2020.

[172] Shreyasi Acharya et al. Multiplicity dependence of (multi-)strange hadron production in proton-proton collisions at $\sqrt{s} = 13$ TeV. *Eur. Phys. J. C*, 80(2):167, 2020.

[173] J. Adam et al. Two-pion femtoscopy in p-Pb collisions at $\sqrt{s_{\rm NN}} = 5.02$ TeV. *Phys. Rev. C*, 91:034906, 2015.

[174] B. Abelev et al. Charged kaon femtoscopic correlations in pp collisions at $\sqrt{s} = 7$ TeV. *Phys. Rev. D*, 87(5):052016, 2013.

[175] Roger Barlow. Systematic errors: Facts and fictions. In *Conference on Advanced Statistical Techniques in Particle Physics*, pages 134–144, 7 2002.

[176] J. Scott Moreland, Jonah E. Bernhard, and Steffen A. Bass. Alternative ansatz to wounded nucleon and binary collision scaling in high-energy nuclear collisions. *Phys.Rev.*, C92(1):011901, 2015.

[177] Epos4: A monte carlo tool for simulating high-energy scatterings. https://klaus.pages.in2p3.fr/epos4/.

[178] Ekkard Schnedermann, Josef Sollfrank, and Ulrich W. Heinz. Thermal phenomenology of hadrons from 200-A/GeV S+S collisions. *Phys. Rev. C*, 48:2462–2475, 1993.